2021-09

Spectrally Multimode Photon Pair Source

Xiong, YanJuan

UNIVERSITY OF CALGARY

Spectrally Multimode Photon Pair Source

by

YanJuan Xiong

A THESIS
SUBMITTED TO THE FACULTY OF GRADUATE STUDIES
IN PARTIAL FULFILLMENT OF THE REQUIREMENTS FOR THE
DEGREE OF MASTER OF SCIENCE

GRADUATE PROGRAM IN PHYSICS AND ASTRONOMY

CALGARY, ALBERTA
SEPTEMBER, 2021

Abstract

The development of the quantum computer challenges the security of classical communication. This is due to the security of classical encryption being based on the computational complexity of an algorithm, for example, the difficulty of factoring a number into its prime product.

Quantum communication uses quantum mechanics to manipulate quantum states and exchange information between two locations. Quantum communication has proven to be unconditionally secure. However, the fact that the maximum transmission distance is largely limited by attenuation in the distribution link remains one of the biggest challenges for practical quantum communication. Quantum repeaters can greatly extend this communication transmission distance. To realize quantum repeaters, one requires quantum memories, entanglement swapping operations, and photon pair-sources. In addition, quantum repeaters greatly benefit - in terms of the achievable entanglement distribution rate - if they can incorporate some form of multiplexing. Multiplexing is possible in any of the available photonic modes, which for transmission in single-mode fibers amounts to polarization, spectral, and temporal modes. The polarization degree of freedom is undesirable because it only has two orthogonal modes. The choice of the spectral or temporal modes for multiplexing then depends on what is most compatible with other components in the setup, particularly the quantum memory, which is the most demanding component. Based on prior demonstrations in the lab of spectral multiplexing in rare-earth ion doped crystals, the purpose of my project has been to build a spectrally multi-mode photon pair-source. Our implementation of the spectrally multi-mode photon pair sources relies on a nonlinear optics process that involves the interaction of strong light and a non-linear crystal. To achieve the spectral selection of specific modes, the non-linear crystal is combined with a suitable cavity.

Acknowledgments

It has been a great and life-changing experience at the University of Calgary for the past two and a half years. I would very much like to extend my deepest gratitude to my supervisor, Dr. Daniel Oblak, for his distinguished guidance and patience. His support and overall insights into experimental optics have made this study an inspiring experience for me and and equipped me for future challenges in my professional career. I would like to extend my sincere thanks to Prof. Christoph Simon, Prof. Paul Barclay and Prof. Timothy Friesen for serving as members of my thesis committee. I very much appreciate Pascal for his openness and generosity in sharing his experience with me. I gratefully acknowledge the assistance of Rana with the detectors. Special thanks to our former member, Jake Davidson, who is so warm and greatly encouraged me when I first joined Cloud-lab. Lastly, it has always been delightful to interact with all other members of our group during work and fellowship.

The rest of my thanks go to my family, my parents, my fiance, James. They have been supportive both financially and emotionally. I also would like to appreciate the support and encouragement from my former boss, Mr. Lu. Sincere friendship with Qiaoqi and company from my little niece has meant a lot to me during my study and research at the University of Calgary.

Table of Contents

List of Tables

List of Figures and Illustrations

List of Symbols, Abbreviations and Nomenclature

Symbol	Definition
U of C	University of Calgary
BS	Bell State
BSM	Bell State Measurement
QR	Quantum Repeater
QKD	Quantum Key Distribution
QDs	Quantum dots
DOF	Degree Of Freedom
QM	Quantum Memory
SPDC	Spontaneous Parametric Down Coversion
PDC	Parametric Down Coversion
SFWM	Spontaneous Four Wave Mixing
PDC	Parametric Down Coversion
PPLN	Periodically Poled Lithium Niobate
OPO	Optical Parametric Oscillator
DR-OPO	Doubly Resonant OPO
JSI	Joint Spectral Intensity
JSA	Joint spectral Amplitude
AFC	Atomic Frequency Comb
REI	Rare-Earth Ion
EPR	Einstein-Podolsky-Rosen
FBG	Fiber Bragg Grating

Chapter 1

Introduction

1.1 Motivation for the thesis

Quantum mechanics developed very rapidly since the concept of quantum theory was first proposed in the early 1900s [1, 2] giving people a new understanding of the microscopic world. Quantum mechanics has already been successfully applied in different existing disciplines such as chemistry, biology, engineering, and many new disciplines based on quantum theory have been derived. Among those disciplines, quantum communication is a very impressive and promising technology. Today, important data is usually encrypted and sent via fiber optics or other channels using digital keys. These data and keys are sent using classical bits, i.e., a stream of electrical or optical pulses that encode bit values 1 or 0 [3]. These communication encryption and transmission security methods mainly rely on complex algorithms, but as long as the computing power of an adversary is strong enough, complex security algorithms can be cracked, and hackers may read and copy data without leaving any trace [4, 5]. Thus, security cannot be fully guaranteed. To solve this problem, secure quantum communication is needed [3].

In secure quantum communication, the sender and receiver use the state of a single optical quantum as an information carrier to establish a key [6]. Compared with traditional communication that is computationally secure, in the sense that the encryption could be defeated by an advanced quantum computer or other hacker technology [4, 5], quantum communication is proved unconditionally secure as a result of the no-cloning theorem[7]. In this information age, data transmission security is of huge importance. Many countries budget and make detailed strategic research plans in quantum technology. The research in quantum computing [9], quantum metrology [10], quantum sensing, and quantum communication [8] has achieved numerous breakthroughs in recent years.

As quantum computing manipulates and encodes data by using qubit[170], computing speed will be greatly enhanced, and vast numbers of calculations can be finished at once. In recent years, there has been vast progress leading to a meaningful quantum computer. In 2019, Google demonstrated that its 54-qubit quantum computer could solve a problem in minutes while a conventional computer would take $10,000$ years [172]. Furthermore, IBM also released their first commercial quantum computer, Quantum System One, in 2019. With quantum computers, vast numbers of calculations can be finished at once [170], which will bring tremendous progress to other scientific research fields, such as climate simulation, pharmaceutical research, and materials science [171]. Furthermore, by linking multiple quantum computer through quantum network can create a quantum computing cluster and realize more computing potential [193]. Similarly as connecting multiple classical computers to form a computer cluster in classical computing and adding more and more processors to the network [194, 195]. In recent work [196], the first prototype of quantum logic gates for distributed quantum computers was reported.

In addition, quantum sensors are also a promising technology, which advanced from proof of principle experiment from quantum physics into fully-fledged systems in the past two decades[173, 174, 175, 176, 177] into fully realized systems. These systems include atomic clocks [185, 186], superconducting quantum interference devices [181], and vapor-cell technologies such as spin-exchange relaxation-free (SERF) magnetometers [182, 183, 184]. Quantum sensors based on different platforms enables quantum-enhanced measurement of time, space, rotation, as well as gravitational, electrical and magnetic fields [187]. By Using quantum entanglement, distant quantum systems can be connected, the measurement of one system will affect the results of another system even if these systems are geographically separated. The two quantum systems are in slightly different environments and can provide information about the environment by interfering with each other. Theoretically, the precision provided by this atomic interferometer is several orders of magnitude higher than that of traditional technology [190, 191]. In the work [189], research has shown a quantum network of phased locked atomic clocks connected by quantum entanglement can result

in a significant boost of the overall precision and one of the advantages of a quantum clock network is the ability to maintain and synchronize the time standards across multiple parties in real-time [192].

The primary method of operating quantum networks is to use quantum communication, which has great advantages in terms of confidentiality and security as a result of the no-cloning theorem [7]. Global quantum communication attracts the constant efforts of scientists. One of the crucial links is to achieve a quantum network all over the world [11]. However, to date, the transmission distance of quantum communication remains limited due to the attenuation of photons by the distribution link [3]. For space link transmission, the loss is mainly caused by diffraction: the spatial mode of photons expands with the square of the travel distance [12, 13]. For optical links, the photons experience decay exponentially with the transmission distance $(0.2-0.3)$ dB/km using standard telecommunication fiber of 1550 nm transmission wavelength due to scattering and absorption [13].

In a classical communication network, signal amplifiers, called repeaters, are used at various points to amplify and regenerate the signal to solve this problem [66]. To achieve long-range quantum communication, a similar solution, which has been coined a quantum repeater, was proposed in [6]. One difference between classical and quantum repeaters is that the former aims to allow a bit to be faithfully transmitted from the sender to the receiver, while a quantum repeater aims to establish an entangled state of two qubits between the sender and the receiver. The main idea of the quantum repeater scheme is to change the problem of establishing long-range quantum entanglement to establishing a series of short-range quantum entanglement and using the entanglement swapping method [6] to extend the distance. According to the no-cloning theorem, the signal cannot be copied; hence, the repeater employed in classical communication that can generate and amplify signal does not apply to quantum communication. Instead, the quantum repeater uses entanglement swapping to link the elementary links of the repeaters until the entanglement is shared with the end node of the distribution link.

However, it is not easy to build a quantum repeater. First, it is necessary to establish a short-distance quantum entanglement, which requires a large number of entangled pairs to be generated quickly. Second, the successful establishment of short-distance quantum entanglement is probabilistic, and entanglement swapping requires two entangled pairs to exist simultaneously. Therefore, a perfect entanglement pair source is a key component of a quantum repeater. An ideal entanglement pair source for a quantum repeater should emit perfect entangled photon states (BS) at a high rate, and one such pair must be at telecommunication wavelengths for transmission via long-distance optical fibers. The entangled photon pair source should also be matched with quantum memory and entanglement swapping [12, 13]. Moreover, entanglement swapping requires the emitted photons to be indistinguishable, and all photon pair sources must have the same properties [12].

Developing an entanglement pair source of high quality is vital to realizing a quantum repeater in the future. However, if we only generate one photon pair at a time, the photon could survive to the end, but it could also be lost during transmission. Even if it is transmitted successfully, if we can only store one photon at a time, the entanglement distribution can only be repeated once the BSM result has been announced and discussed via classical communication to the elementary link node [12]. Suppose the elementary link length is L_0, the maximum attempt rate will be c/L_0 (c is light speed). However, if we can send n photons and can store n photons simultaneously, the likelihood of successfully transmitting photons is significantly enhanced, and the attempt rate is n times faster, greatly improving the classical communication efficiency. Specifically, in this thesis, we will describe the possibility of building frequency multiplexed photon pair-source using spontaneous parametric down-conversion. Different experiments towards this goal will be presented and discussed.

1.2 Thesis organization

The structure of the thesis is as follows: First, the basic elements of quantum communication and how to achieve quantum communication over long distances utilizing Quantum repeater(QR) are introduced. Second, different elements to build a frequency multiplexed quantum repeater will be introduced in Chapter 2. Next, the fundamental nonlinear optics will be introduced in Chapter 3. Chapter 4 will focus on the method to build a spectrally multimode photon pair source and the detailed experiments conducted during my MSc. Finally, in Chapter 5, conclusions will be presented.

Chapter 2

Background

2.1 Basic concepts

In this section, some basic components of quantum communication will be introduced.

2.1.1 Qubits

A Bit is a fundamental unit in classic information, represented by 0 and 1. Similar to a mechanical switch, it only has two absolute states either on or off. The superposition principle in quantum mechanics allows a physical system to be in a probabilistic combination of two states, that is, qubit, which is an elementary unit in quantum information. It can be represented by the linear superposition of two normalized orthogonal states. These two basic states can be wrote as $|0\rangle$ and $|1\rangle$. The general state of the qubit can represented as:

$$|\psi\rangle = \alpha|0\rangle + \beta|1\rangle, \tag{2.1}$$

where α and β are complex probability amplitudes and must fulfill the normalization constraint

$$|\alpha|^2 + |\beta|^2 = 1.$$

In quantum mechanics, the Bloch sphere is a geometrical representation of a quantum state shown in Fig. 2.1. Every 1-qubit state can be represented as a point on the sphere surface. It allows us to write the qubit state as follows:

$$|\psi\rangle = \cos\left(\frac{\theta}{2}\right)|0\rangle + e^{i\phi}\sin\left(\frac{\theta}{2}\right)|1\rangle, \tag{2.2}$$

where θ and ϕ are defined as angles from the Z and X axes.

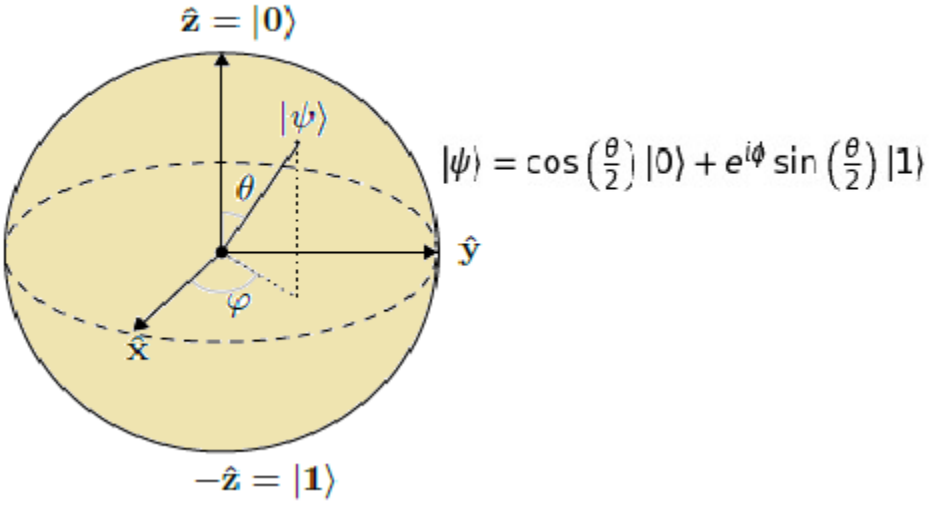

Figure 2.1: A qubit $|\psi\rangle$ represented as a point on the surface of the Bloch-sphere parametrized by the angular coordinates θ and ϕ.

Quantum information can be encoded and distributed using different physical systems [14]. As photons can be measured and transmitted easily, it is a good choice to encode qubits into some degrees of freedom of photons. For instance, polarization is commonly used to form a qubit as it is a naturally two-level system comprising $|H\rangle$ and $|V\rangle$, which is a complete basis [15], where $|H\rangle$ and $|V\rangle$ denote horizontal and vertical polarization, respectively. Another frequently used qubit is time-bin qubit [16] formed by two different emission times of a photon, referred to as early $|e\rangle$ or late $|l\rangle$. Which type of encoding one uses is mainly dependent on individual application.

2.1.2 No-cloning theorem

The no-cloning theorem is a result of quantum mechanics that forbids to perfectly copying an unknown quantum state [17]. The impossibility of cloning can be used as an advantage to create secure communication between two parties using QKD [18]. The no-cloning theorem suggests that an eavesdropper could not intercept and duplicate the information transmitted by the two parties without disturbing it and hence being spotted.

The reasoning can be found in [13]. Suppose that there exists a unitary operator U that copies

an arbitrary unknown q-state $|\phi\rangle = \alpha|0\rangle + \beta|1\rangle$. $|0\rangle$ is a blank state. Then the process can be represented by

$$\hat{U}|\phi\rangle|0\rangle = |\phi\rangle|\phi\rangle = (\alpha|0\rangle + \beta|1\rangle)(\alpha|0\rangle + \beta|1\rangle = \alpha^2|00\rangle + \beta\alpha|10\rangle + \alpha\beta|01\rangle + \beta^2|11\rangle \tag{2.3}$$

However, if we use U to copy the expansion of $|\phi\rangle$, we will end up with a different state

$$\alpha|0\rangle + \beta|1\rangle)|0\rangle \quad \xrightarrow{U} \alpha|00\rangle + \beta|11\rangle \tag{2.4}$$

No cross-terms existed here. It proves that there can not exist an ideal quantum cloning machine capable of copying arbitrary quantum states exactly.

2.1.3 Quantum entanglement

Quantum entangled states are special quantum superposition state of multiple particles. A particle 1 stays at a certain physical superposition state $|\psi\rangle_1$, while particle 2 stays at a superposition state $|\psi\rangle_2$. When these two particles are entangled, the superposition of two particles will be established. This compound state $|\psi\rangle_{12}$ can not be ascertained by simple analysis of the properties of the individual states $|\psi\rangle_1$ and $|\psi\rangle_2$ [13]. For example $\Phi_{12} = \alpha\,|0\rangle_1|1\rangle_2 + \beta\,|1\rangle_1|0\rangle_2$ is an entangled state. The basic characteristic of such a system is that it cannot be written in the form of the direct product of two subsystems as below:

$$|\psi\rangle_{12} \neq |\psi\rangle_1 \otimes |\psi\rangle_2 = |\psi\rangle_1|\psi\rangle_2 \tag{2.5}$$

Entangled particles have robust non-classical correlations, which can be used as an essential resource in quantum information processing. We can use it to share keys as well as implement quantum teleportation, which is also the basis of long-distance quantum communication relay [19]. Bell states known as the four maximally entangled two-qubit states and to form a complete basis of the four-dimensional Hilbert space for two quits, are the most widely used entangled states in

quantum communication [20]. They can be expressed as below:

$$\left|\psi^{\pm}\right\rangle_{12} = \frac{1}{\sqrt{2}}\left[|0\rangle_1|1\rangle_2 \pm |1\rangle_1|0\rangle_2\right] \tag{2.6}$$

$$\left|\phi^{\pm}\right\rangle_{12} = \frac{1}{\sqrt{2}}\left[|0\rangle_1|0\rangle_2 \pm |1\rangle_1|1\rangle_2\right] \tag{2.7}$$

Photon pairs can be entangled in different degrees of freedom such as in polarization [21], frequency [22], spatial mode [23], energy-time [24, 25] and time-bin [26, 27]. Currently, there are different types of schemes of generating entangled single photon pairs, such as by making use of nonlinear optical interaction like spontaneous parametric down-conversion (SPDC) [21, 28, 29] and spontaneous four-wave mixing [30], which are the two most widely used approaches. Alternatively, approaches include entangled photon pairs generated due to the transitions in atoms or ions [30] like atomic cascade sources and artificial atoms like quantum dots that are truly on-demand photon entangled photon pairs [31].

2.1.4 Bell-state measurement

Bell state measurements are crucial for quantum communication protocols such as QKD [31, 32], entanglement swapping [33], quantum teleportation [36], quantum repeaters [37], as well as in linear optics quantum computing [39]. A BSM results in is the projection of two qubits onto one of the four Bell states. The main device used for photonics Bell-state measurements is the 50:50 beam-splitter, followed by a measurement device that can identify two orthogonal modes for qubit encoding. When a photon enters a beam-splitter, it may pass through or be reflected. The odds of a photon going either path are 50%. The various situations of beam-splitter output are shown in Fig. 2.2 . There are four possibilities if two photons enter the beam-splitter from each input port: A reflection, B pass; A pass, B reflection; A reflection, B reflection; A pass, B pass. In the first case, the two output photons are bunched to the left side coincidentally, whereas two output photons are bunched to the right side in case 2, as shown in Fig. 2.2 (b, c). However, we cannot distinguish

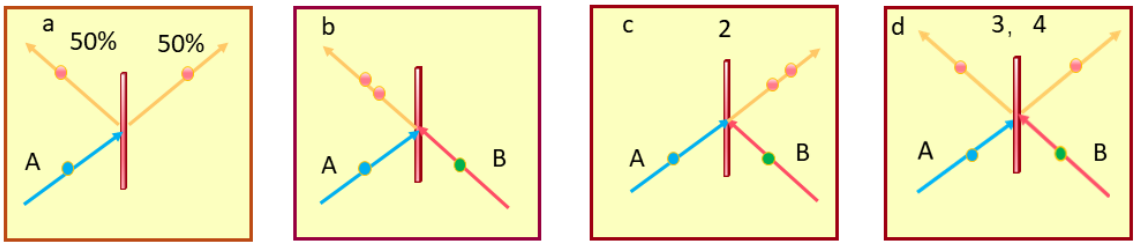

Figure 2.2: A photon bunch on a beam-splitter, either reflected or transmitted as shown in (a), If two photons enter the beam-splitter from each port, there are four cases 1: A reflection, B pass; 2: A pass, B reflection; 3: A reflection, B reflection; 4: A pass, B pass. In the first case, the two output photons are bunched to the left coincidentally see (b). In case 2, both two output photons are bunched to the right, as shown in (c). However, we cannot distinguish between the third and fourth cases as photons are indistinguishable. We are not able to identify which photons comes from A or B, as shown in (d).

between the third and fourth cases as the photons are indistinguishable. We are not able to identify which photons come from A or B, as shown in Fig. 2.2 (d).

A typical photonic BSM setup for polarisation and time-bin qubits is composed of a beam-splitter followed by detectors, see Fig. 2.3. The input and output spatial modes are labeled as $1,2,3,4$, respectively. After the beam-splitter transformation, the four Bell states mentioned in Eqs.(2.6)*and*(2.7) become

$$\begin{aligned}
|\phi^{\pm}\rangle_{12} &= \frac{1}{\sqrt{2}}(|00\rangle_{12} \pm |11\rangle_{12}) \quad \rightarrow \quad \frac{i}{2}(|00\rangle_{33} + |00\rangle_{44} \pm |11\rangle_{33} \pm |11\rangle_{44}) \\
|\psi^{+}\rangle_{12} &= \frac{1}{\sqrt{2}}(|01\rangle_{12} \pm |10\rangle_{12}) \quad \rightarrow \quad \frac{i}{2}(|10\rangle_{34} + |01\rangle_{34}) \\
|\psi^{-}\rangle_{12} &= \frac{1}{\sqrt{2}}(|01\rangle_{12} - |10\rangle_{12}) \quad \rightarrow \quad \frac{i}{2}(|10\rangle_{34} - |01\rangle_{34})
\end{aligned} \tag{2.8}$$

Note that $|\phi^{+}\rangle$ and $|\phi^{-}\rangle$ result in coincidences of photons in states 0 and 1 in the same output port of the beam splitter, hence $|\phi^{+}\rangle$ and $|\phi^{-}\rangle$ can not be distinguished. Eqs.2.8 indicates coincidences of photons in states 0 and 1 in the same output port of the beam-splitter, ,as shown in Fig. 2.2 (b, c), projection onto $|\psi^{+}\rangle$ and coincidence of photons in states 0 and 1 in different output ports gives projection onto $|\psi^{-}\rangle$. Therefore, it is evident that only 2 of the 4 bell states can be

unambiguously distinguished [37]. As discussed above, the four Bell states cannot be completely distinguished by using linear optics. The bell states measurement highly affects the fidelity in quantum communication, to achieve full Bell measurements; some other approaches could be used such as nonlinear optics [40] and adopted "continuous variable" entanglement sources [41, 42].

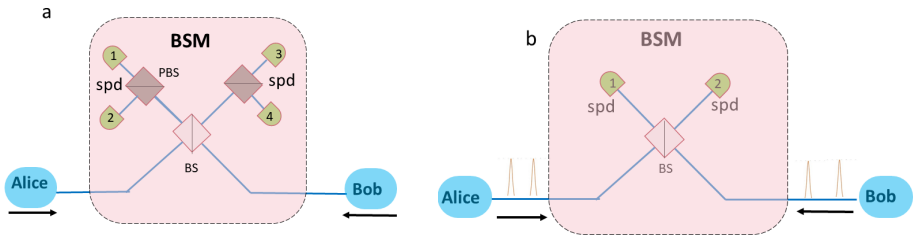

(a) BSM setup for polarization qubits. (b) BSM setup for time-bin qubits.

Figure 2.3: The BSM Setup. The BSM setup for polarization qubits is shown in (a). A polarization beam-splitter (PBS) is included at each beam-splitter output port. After passing through PBS, the photons are divided probabilistically into vertical and horizontal polarization paths. Two possibilities for the left and right photons are detected by detectors 1, 2 and 3, 4, respectively. Part (b) shows the BSM setup for time-bin qubits, whereas the outputs of the beam-splitter aredetected by single-photon detectors (SPDS), which should be able to identify early and late temporal modes.

2.1.5 Quantum teleportation

Quantum teleportation was proposed by Bennet [36] in 1993, after which, a considerable amount of theoretical and experimental research has shown that [34, 38, 59, 60, 61, 62] an unknown quantum state of a particle can be transmitted to a distant place without embodied transfer. It is a unique form of communication for quantum systems, and there is no classical counterpart. Quantum teleportation can be applied to construct quantum repeaters for quantum networks and remote state preparation [34, 35], which have a wide range of important applications.

Using EPR [46] entangled pairs correlation, an unknown quantum state $|\phi\rangle_{\mathrm{A}}$ can be transferred between sender Alice and receiver Bob. Alice prepares the EPR entangled pair composed of particle B and particle C [34]. Particle A is in an unknown single-particle state $|\phi\rangle_{\mathrm{A}} = \alpha|0\rangle_{\mathrm{A}} + \beta|1\rangle_{\mathrm{A}}$ Where α and β are complex constants, and particle C is in Alice's place and ready to teleport.

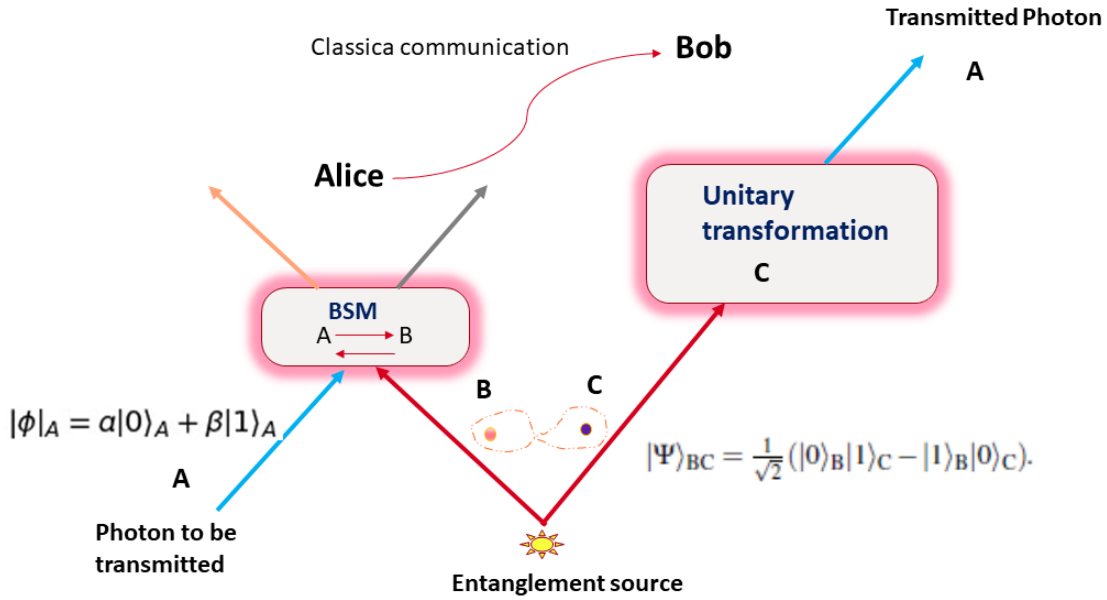

Figure 2.4: Quantum Teleportation. Alice wants to send quantum state A to Bob. B and C in the green color dot circle is an entangled pair. Here, the phone acts as a classic channel. Alice performs joint Bell-state measurements on A and B. After the measurement, the quantum state of A collapses, B changes, which immediately triggers the change on C. Alice communicates the measurement results to Bob by phone. Then Bob makes a unitary transformation on C accordingly that ends up with all information from A being transmitted to C. .

Suppose particles B and C are in the quantum state $|\Psi\rangle_{\mathrm{BC}} = \frac{1}{\sqrt{2}}(|0\rangle_{\mathrm{B}}|1\rangle_{\mathrm{C}} - |1\rangle_{\mathrm{B}}|0\rangle_{\mathrm{C}})$. Then the original three-particle state $|\Psi\rangle_{ABC}$ can be expressed by:

$$|\Psi\rangle_{ABC} = (\alpha|0\rangle_A + \beta|1\rangle_A) \otimes \frac{1}{\sqrt{2}}(|0\rangle_B|0\rangle_C - |1\rangle_B|1\rangle_C) \tag{2.9}$$

If we expand it using the Bell states of the two-particle system of B and C, then (2.9) becomes to

$$\begin{aligned} |\Psi\rangle_{ABC} = & \frac{1}{2}\left|\Phi^+\right\rangle_{AB} \otimes (\alpha|0\rangle_C + \beta|1\rangle_C) \\ & + \frac{1}{2}\left|\Phi^-\right\rangle_{AB} \otimes (\alpha|0\rangle_C - \beta|1\rangle_C) \\ & + \frac{1}{2}\left|\Psi^+\right\rangle_{AB} \otimes (\beta|0\rangle_C + \alpha|1\rangle_C) \\ & + \frac{1}{2}\left|\Psi^-\right\rangle_{AB} \otimes (\beta|0\rangle_C - \alpha|1\rangle_C) \end{aligned} \tag{2.10}$$

Suppose Alice conducts a joint bell measurement on Particles A and B. In that case, the quan-

tum states of the two-particle system of A and B will collapse into any one of the four Bell states while Bob's quantum state collapses to the corresponding quantum state. Alice will inform Bob of the joint Bell measurement results, and Bob can make particle C in the initial unknown state $|\phi\rangle_{\mathrm{A}}$ through different unitary transformations on the particle C corresponding to different measurement results and realize the teleportation, see Fig. 2.4. Note that if particle A is one member of entangled photon pairs, then the entanglement would be swapped onto particles that have never been entangled before. This is known as entanglement swapping, which is the basic operating unit of a quantum repeater that can be used to overcome photon attenuation problems in long-distance quantum communication [33].

2.2 Quantum repeater

In the previous chapter, we discussed that encoding a quantum state into a DOF of a photon is a convenient way to distribute it either by optical fiber or through free space. The transmission distance is greatly limited in long-distance quantum communication due to photon absorption and scatter in the optical fiber. The photons experience attenuation that grows exponentially with the distance. The typical fiber loss in the current 1.5 um communication band is about 0.2 dB/km. For free-space links (outside the earths atmosphere), the loss is mainly due to the propagation loss that is proportional the square of the traveled distance as well as the atmospheric absorption and the loss caused by bad weather like fog or rain. To date, the largest single-photon level transmission distance is 1200 km [48] by satellite and 509 km through optical fiber link [49]. In a classical network, repeaters are used at various points to amplify and regenerate the signal to solve this problem. But this schema can not apply to quantum communication due to the no-cloning theorem. To achieve long-distance quantum communication, alternative technology must be adopted to overcome the exponential attenuation of distributing links.

A plausible solution for that problem is the quantum repeater (QR)[51], proposed by Briegel and Zoller in 1998. The basic idea is to split the total communication length L into N short distance

links (elementary link L0) and establish entanglement overall elementary links. Shared entanglement between the adjacent elementary can be created through entanglement swapping operations. The entanglement can be distributed between the end nodes of the communication link if this operation is repeated [42]. (see Fig. 2.5)

In more detail, first, by dividing the quantum channel between Alice and Bob into 2^n link, the attenuation of quantum information in this elementary link is tiny under the present technical condition so that the entanglement distribution can successfully complete, while the fidelity can be assured to meet the communication threshold requirements. Second, parallel entanglement pairs for two nodes should be distributed at the ends of each link and stored in their respective device named quantum memory (QM). Note, optical quantum memory is refer to one whose state can be prepared and/or manipulated using light. The quantum state is also purified using an entanglement purification technique [63], so that the degree of entanglement between them reaches the threshold requirement for secure quantum communication. After establishing entanglement between two neighboring nodes, the entanglement swapping performed operating a joint projective measurement at the quantum relay station extends the communication distance and makes the non-neighboring nodes also in the entangled state. Finally, repeat this process until the entanglement is shared by the end nodes of the communication link.

Now we know the basic framework of a quantum repeater. There are many different schemes for physical quantum repeater implementation. Generally, a quantum repeater can be of two types, one of which is the scheme of to-the-memory [65], which means that the entanglement is established from an external entanglement source to an internal QM entanglement (see Fig. 2.6). The crucial parts in this architecture is the high-quality quantum memory and entanglement source. Another proposal is the scheme of from-the-memory, which establishes entanglement from the internal QM and shares the entanglement with different QMs through post-selection (see Fig. 2.6) [65]. Specifically, the process is first to establish the entanglement between the QM energy level transition and accompanying emitted photon. Then, Bell-state measurements need to be conducted

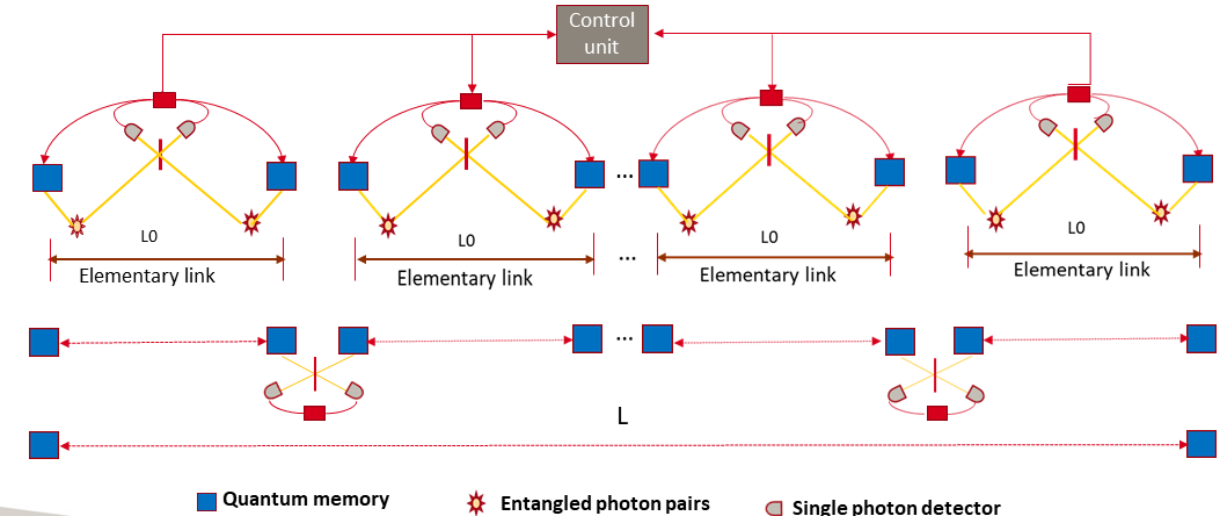

Figure 2.5: Schematic quantum repeater diagram with its main components. The transmission distance is broken up into segments with lenth of L, each elementary link includes two entangled photon pair sources and two QMs and a central BSM unit

.

on the accompanying photon so that the two QMs establish entanglement. This scheme was first proposed by L-M. Duan et al., namely the DLCZ protocol[52]. Note, although quantum memory is pivotal for these two schemes, an all-photonic repeaters protocol, not quantum memory based was also developed [53, 54]. In this thesis, we focus on the first QR architecture based on photon-pair sources and absorptive quantum memories [55, 56]. In this architecture, each elementary link is composed of two entangled photon pair sources, two QMs, and an entanglement swapping operation based on a BSM that is conducted by merging two photons on a beam-splitter [66]. For more details, see Fig. 2.7.

Note that if the QMs can only store a single photon, then entanglement distribution over elementary links can be repeated only once the BSM result has been released and communicated through classical communication to the elementary link nodes. This results in a maximum attempt rate of $\sim c/L_0$ if elementary links are symmetric, i.e., the BSM station is exactly in-between the QMs. L_0 refers to the elementary link length and c to the speed of light. But if the memories can store n photons simultaneously, entanglement distribution can be attempted at a rate (R) n times faster, $R = nc/L_0$, improving the chance of entanglement distribution per time over an elemen-

(a)

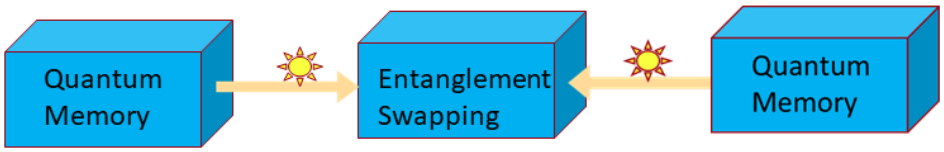

(b)

Figure 2.6: Two types of quantum repeater: (a) to-the-memory: an extra entanglement source send the entangled photon to the quantum memory and established the entanglement between two quantum memory. (b) from-the-memory: the entanglement between the QM energy level transition and accompanying emitted photon was established. The two QMs entanglement established by conducting Bell-state measurements on the accompanying photon

tary link and hence reducing the time required to distribute entanglement over the entire length. Thus, many quantum repeater architectures rely on the capability to store multiple copies of entangled qubits simultaneously. We will explain a quantum repeater architecture based on frequency multiplexing in the following section [64].

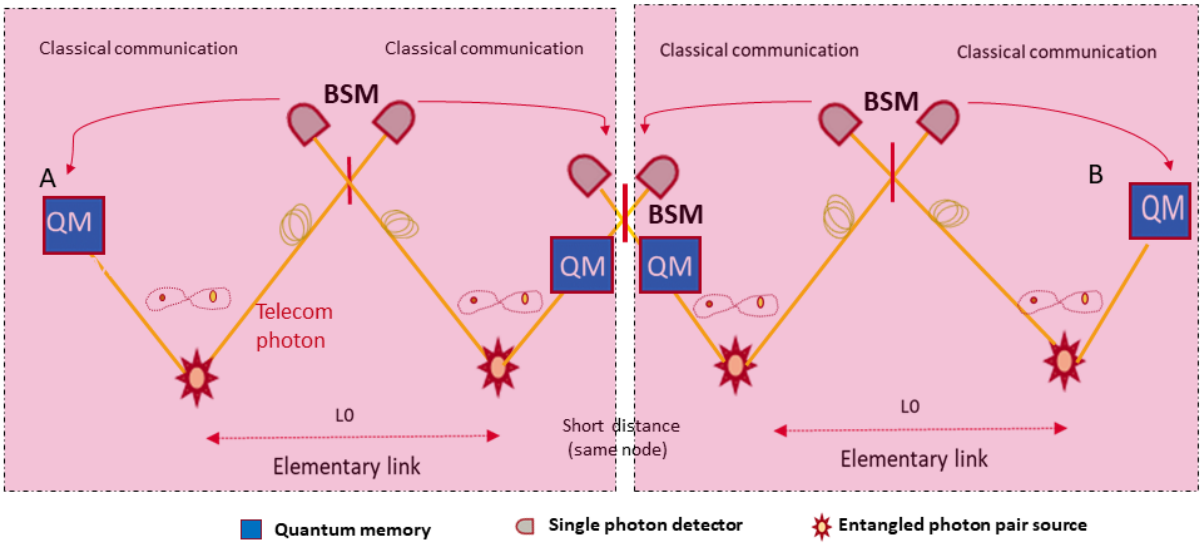

Figure 2.7: Quantum repeater architecture based on entangled photon pair sources and absorptive quantum memories. Each photon pair source generates an entangled photon pair. One photon of each pair is stored in a quantum memory while the other photon is sent via a long fiber link and meets with another photon that travelled from the neighboring entangled photon pair source in a beam-splitter where a BSM will be performed. The successful of the BSM heralds the presence of entanglement between the two QMs. Then, when neighboring elementary links successfully heralded the presence of entanglement, the photons are retrieved, and a BSM is attempted to swap entanglement between elementary links. The process is repeated until entanglement is distributed across the total communication distance[64].

2.3 Frequency multiplexed quantum repeater

In this section, we will shortly introduce the QR architecture based on frequency multiplexing proposed in [64]. As explained in the previous sections, compared with using a single photon, the use of multiple photons simultaneously would significantly increase the entanglement distribution rate (see Fig. 2.7). The primary idea is to simultaneously generate numerous entangled photons pairs with different frequencies and operate a BSM independently with all the frequency modes

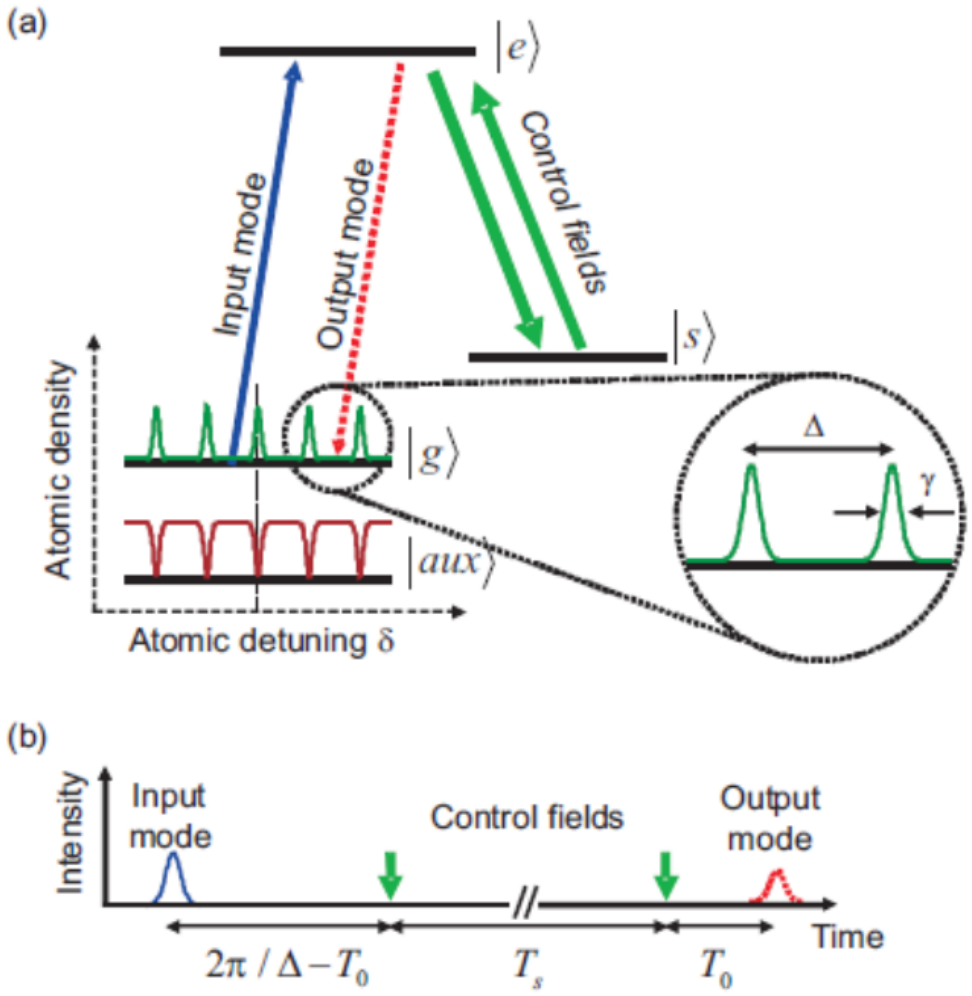

Figure 2.8: Atomic frequency comb storage protocol. a) All atoms are initially in the ground state $|g\rangle$. The inhomogeneously broadened optical transition $|g\rangle - |e\rangle$ is then shaped into an comb structure by optical pumping to $|aux\rangle$ level, which is composed of numbers of peaks with width (FWHM) γ and are separated by Δ. (b) The input mode is completely absorbed and coherently excites the AFC modes, a photon echo being re-emitted after a time $2\pi/\Delta$. A pair of control fields on $|e\rangle - |s\rangle$ allow for longtime storage as a collective spin wave in $|s\rangle$, and on-demand read-out obtained after a storage time T_s by applying a controlled light.[168]

at once. The goal is to distribute entanglement over an elementary link ideally deterministically, which can be achieved if enough frequency modes are simultaneously employed. Furthermore, as a result of entanglement over each elementary link being distributed in every attempt, the quantum memories do not need to allow recall on demand (the stored photons are released and send to operate BSM), which relaxes the requirements for the quantum memories. For swapping entanglement between elementary links, the successfully stored modes must be recalled from the QMs and shifted to a common reference frequency as the photons impinge in a BSM need to be indistinguishable in all DOF [64]. Our group is building the different elements required to build a frequency multiplexed QR consisting of three functional parts, as below.

1) **Frequency multiplexed entangled photon pair sources**. Sources that can generate multiple entangled photon pairs in different frequency modes simultaneously. In our group, we focus on developing a spectrally multimode photon pair source based on SPDC, and it is also the main work of my master project.

2) **Spectrally multi-mode quantum memories**. Memories that can store multiple frequency modes simultaneously. Our group focuses on developing a frequency multimode quantum memory based on rare-earth ion (REI) doped solids and the so-called atomic frequency comb (AFC) protocol shown as in Fig.2.8. [168]

3) **Entanglement swapping operations**. By performing a spectrally resolved BSM between two members of different entangled photon states, swapping entanglement was operated, and the entanglement transferred to the remaining photons. Our group has realized entanglement swapping based on linear optics, this work is introduced in [66].

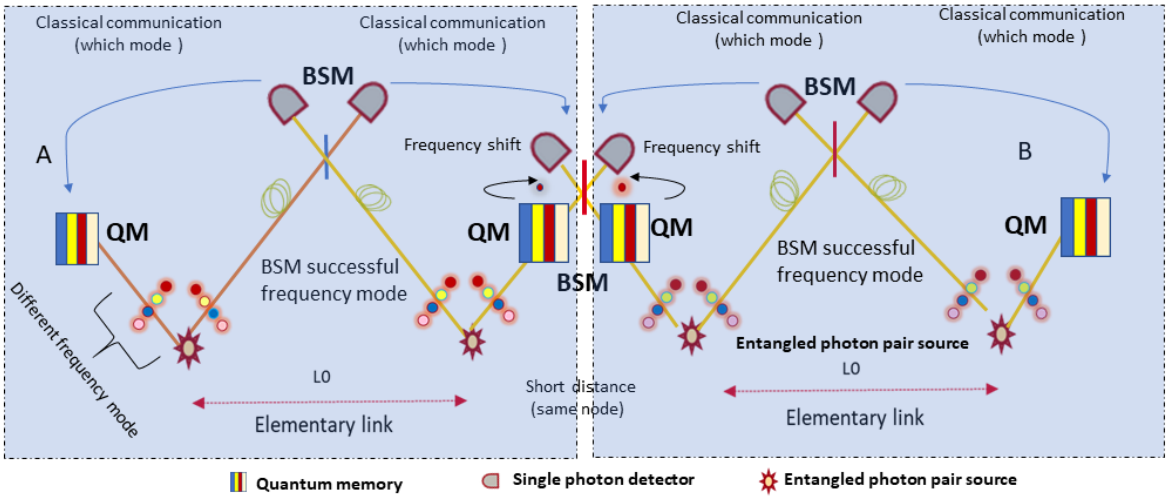

Figure 2.9: Frequency multiplexed quantum repeater scheme. In each elementary link two frequency multiplexed sources generate many pairs of entangled photon pairs in different spectral regions. One photon from each entangled pair is sent to the center of the elementary link, where a spectrally resolved Bell-state measurement (BSM) is operated for swapping entanglement. With enough frequency modes simultaneously, the probability nearly to unity to succeed in at least one BSM is ensured. The other photon from each pair is sent to quantum memories (QMs) where all frequency modes are stored. The information about which frequency modes succeeded in the BSM is sent by classical communication. Next, all frequency modes are recalled from the QMs. After frequency shifting, only the mode corresponding to the successful BSM is allowed to pass through altogether with previously agreed-on reference resonance frequency, while the other photons are rejected. The last step ensures indistinguishably between the two photons coming from different elementary links, which is required in order to conduct a BSM at the interface of two elementary links. This BSM results in entanglement swapping across neighboring elementary links[51].

2.4 Quantum repeater based on parametric downconversion sources

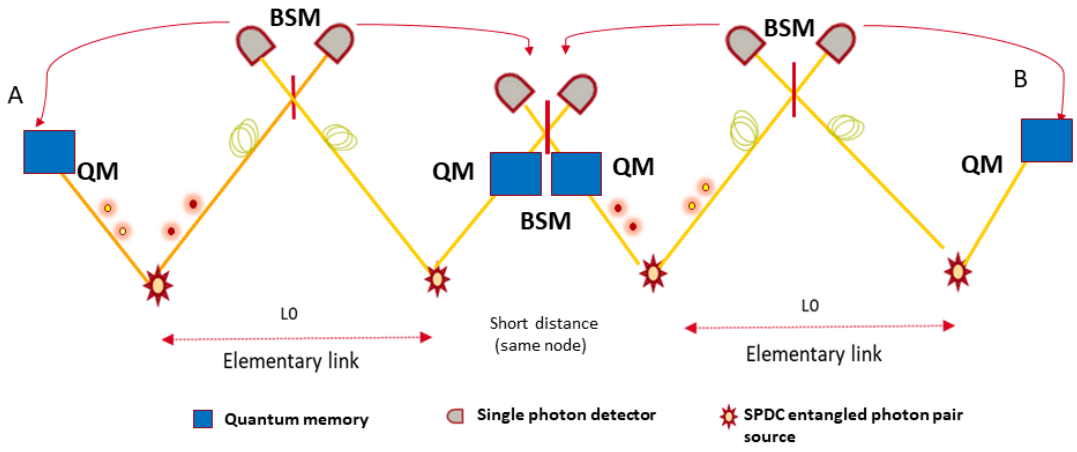

Figure 2.10: Limitation of quantum repeater diagram based-SPDC source. The first PDC source yields two photon pairs, while the second gives nothing. The single photon detector (which are non-photon number resolving) cannot distinguish between one or multiple photons coming in [119]. The twofold coincidence in the detectors is still possible, but the second PDC source sending "0" photon and entanglement swapping operation has not been achieved

In the previous two sections, a basic principle of quantum repeater and a quantum repeater scheme based on frequency multiplexed was introduced, in which the entangled photons can be generated by parametric down-conversion (PDC) in a nonlinear crystal. As is known, this down converted process always creates multiple photon pairs in some probability [112, 113, 114, 115]. The quantum state generated into the signal and idler modes from an SPDC source can be described by a two-mode squeezed vacuum (TMSV)[116]:

$$|\psi\rangle_{SI} = \sqrt{1-\lambda^2}\sum_{n=0}^{\infty}\lambda^n|n\rangle_S|n\rangle_I \tag{2.11}$$

$|n\rangle$ refers to an n -photon state, and λ is the squeezing parameter [116, 117]. From Eq.2.11, one can find it includes higher-order photons that contribute to the multi-photon emissions [116].

The presence of higher-number components could degrade the quality of the two-photon inter-

ference's in the Bell state measurement (BSM) and causes errors [118]. In long-distance quantum communication implementations with quantum repeater architecture, it is not possible to eliminate the errors by working with a low pump power. This is because intrinsically the probability of a Bell-state measurement caused by multi-pair emissions from one side of the BSM input remains equal to the probability of a BSM due to actual single-pair photons arriving from separate inputs. As shown in Fig.2.10, when the first PDC source yields two photon pairs, while the second gives nothing, the single photon detector (which are non-photon number resolving) cannot distinguish between one or multiple photons coming in [119, 120]. So the twofold coincidence in the detectors is still possible, but the second PDC source sends "0" photon and the entanglement swapping operation has not been achieved. This problem can be avoided if the detector can distinguish between one or several photons [121].

A practical quantum repeater approach based on SPDC was proposed in [118] by adding a photon number plus spectrally resolving detectors and multimode quantum memories. Multimode memories can compensate for the requirement of working with low-pair emission probability and photon-number-resolving detectors that can distinguish the number of photons and significantly remove the remaining errors due to multipair emissions [118]. Thus, in order to realize a practical frequency multiplexed quantum repeater, one can rely on performing photon-number spectrally resolved measurements in the heralding arm, which are able to enhance the heralding of single-photon states by suppressing the higher photon number components [121]. As is shown in Fig.2.11.

Substantial efforts have been made in the development of photon-number-resolving detectors (PNRDs) [122], either multiplex non-PNR detectors or fabricate SPAD arrays on a single chip [123, 124, 125, 126, 127, 128, 129]. In addition, individual devices as sensors superconduction transition edge [130, 131] and semiconductor system [132, 133] based were shown to resolve a few photons without multiplexing. Recently, a superconducting nanowire photon-number-resolving detectors integrated with current reservoirs that can resolve up to 11 photons was realized in [134]. We can expect the real practical frequency multiplexed quantum repeater is within reach.

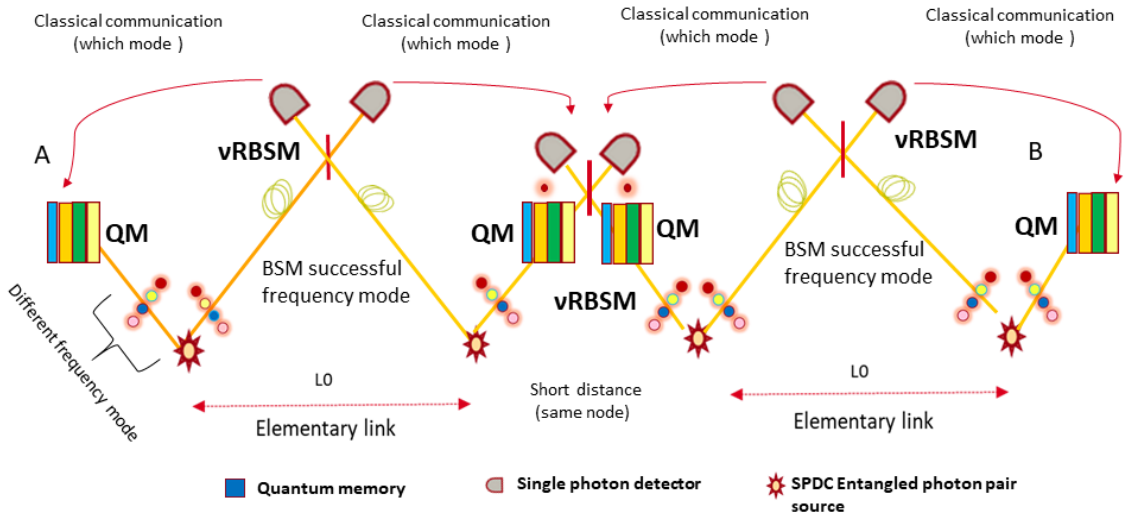

Figure 2.11: Practical frequency multiplexed quantum repeater. Instead of using a non-photon-number-resolved detector, by relying on performing photon-number spectrally resolved measurements in the heralding arm, the enhancement of the heralding of single-photon states could be realized by suppressing the higher photon number component.

Except to use SPDC entangled source, alternative promising entangled photon sources that could be used in quantum repeater is the quantum dot (QDs) [135, 136], which has been tremendously investigated in the past decades and could generate entangled photons on demand. QDs can be created using various methods such as molecular beam epitaxy [137], where the process of self-assembled (Stranski-Krastanov) growth [138] forms tiny islands of smaller-band-gap semiconductors embedded in a larger-band-gap semiconductor [137]. Besides, chemical synthesis can be used to produce colloidal quantum dots [139]. Quantum dots can be excited optically [146] or electrically [147]. Quantum dots base on CdSe in ZnS, [139] InP in GaInP, and InAs in GaAs,[140] are examples of optically active dot while an example of an electrically driven quantum dot is InAs.[148, 149] Quantum dots as single-photon emitters need to operate at cryogenic temperatures, which is technically cumbrous. In addition, each QD is a unique structure and suffers from lower indistinguishability and fidelity because of charge fluctuations in their local environment even though dedicated effort was made in addressing these problems such as pump resonate

pumping [141, 142, 143, 144] and progress in tuning them controllably [150, 151].

In addition, color center defects in diamond is another approach to generate single photons and could be a potential quantum emitter [152], the nitrogen-vacancy (NV) defect [153, 154] being the most widely investigated albeit of the indistinguishability in problem due to the spectral drift [154]. A nitrogen-vacancy (NV) color center [156, 157] is formed by a substitutional nitrogen atom and a vacancy at a neighbouring lattice position in diamond. [158] The emission line of the nitrogen-vacancy center is at 637 nm with a spectrum bandwidth broader than 100 nm spectrum bandwidth [156, 157] while the zero-phonon emission line of the nicel-nitrogenvacancy center is around 800 nm with a few nanometer's bandwidth. [159, 160, 161] It is noticed there are hundreds of color centers in diamond, so it is possible other suitable defects could also be used as a single emitter [158]. Recently, work has demonstrated coupling of individual NV centers to a microring resonator and fiber microcavity [162]. These approaches could be used in quantum information applications.

Single atoms and molecules could be another promising source [163, 164]; however it is not easy to integrate and engineering.

In the last sections, the source requirement of frequency multiplexed quantum repeater scheme was introduced, one can use a multimode entangled photon source, which can emit many frequency modes simultaneously, or by integrating many single-mode entangled photon sources. But compared with quantum dots and NV center emitters, the SPDC sources are easily have a different frequency output, broad bandwidth and can be easily tailored to fulfil the requirements to be implemented in frequency multiplexing [66].

In the following chapters, the required elements to build a spectrally multimode photon-pairs source will be explained in more detail, and the experiments conducted during my master's degree will be described.

Chapter 3

Nonlinear optical frequency conversion

In this chapter, the fundamental theory of the generation of photon pairs in non-linear optical media via a process of SPDC will be introduced, which is the basis of all experiments presented in this thesis.

3.1 Spontaneous parametric down-conversion

The most important and common way to prepare photon pairs is to use the SPDC process based on nonlinear optical interaction between intense light with nonlinear crystals. The experimental simplicity and flexibility of these sources have earned them a role in numerous quantum information applications [69]. The process of SPDC was first described by D. C. Burnham and D. L. Weinberg in 1970 [67], and the experiments were conducted for the first time by Carroll Alley and Yanhua Shih Rupamanjari Ghosh and Leonard Mandel in the late 1980s [68].

In the SPDC process, a pump light passes through the nonlinear crystal to generate two low-energy photon pairs called signal light and idler light, respectively. For a better understanding of this process, the theoretical analysis of SPDC will be given in the following.

The induced polarization $P(t)$ by an external field $E(t)$ can be expressed as [71].

$$P(t) = \varepsilon_0 \left[\chi^{(1)} E(t) + \chi^{(2)} E(t)^2 + \chi^{(3)} E(t)^3 + \ldots \right] \tag{3.1}$$

Where ε_0 is the vacuum electrical permeability and $\chi^{(n)}$ is the susceptibility tensor and is a characteristic of the material. From this expression, we can identify the linear interaction described by $\chi^{(1)}$. Generally, the process to generate photon pairs makes use of relatively large second $\chi^{(2)}$ and third-order $\chi^{(3)}$ electrical susceptibilities present in some materials, and they are referred to as SPDC and SFWM, respectively [70]. In this thesis, we will focus on the SPDC process, which is

the basis of the experiment presented in the following sections.

The SPDC process can be described by the following Hamiltonian [72].

$$\mathscr{H}_i = i\hbar\zeta \left[\hat{a}_i^\dagger \hat{a}_s^\dagger - \hat{a}_i \hat{a}_s\right] \tag{3.2}$$

Where $\hbar$ is the reduced Planck constant, while $\hat{a}_i\,(\hat{a}_s)$ is the annihilation operator of a photon in the idler (signal) modes and ζ is a constant proportional to $\chi^{(2)}$ and the pump intensity. For finding the state after the interaction with the crystal $|\psi\rangle_{is}$. Here, apply the time evolution operator on the vacuum state and use the previous Hamiltonian in Eq 3.2 gives

$$|\psi_{is}\rangle = e^{i\mathscr{H}_i/\hbar}|0\rangle = \cosh(\zeta t)^{-1} \sum_{n=1}^{\infty} \tanh(\zeta t)^n \, |n_i n_s\rangle \tag{3.3}$$

Where t corresponds to the interaction time, and $|n\rangle$ refers to photon number states. As discussed in section 2.4, in a time duration that light passes through the nonlinear crystal, the state of the field has probabilities of being in a zero biphoton state, a one-biphoton state, a two-biphoton state, and so on [72]. Light whose number statistics obey this exponentially decaying photon number distribution is known as thermal or super-Poissonian light [72]. The thermal bi-photon state with an average photon pair number is known as $\langle\mu\rangle = \sinh(\zeta t)^2$ [72]. Since the photons are created in pairs $|n_i n_s\rangle$, there is a perfect correlation between the photon number in each mode, leading to the fact that each mode, if analyzed independently, features a thermal photon number distribution [70]. In many applications, the number of higher-order biphoton states needs to be small since muti-photon introduces white noise in practical operations [70].

The SPDC process also must fulfill two main conservation criteria: energy and momentum conservation. Energy conservation can be expressed by noting that the total energy of the created photon pairs equals the energy of the pump photon (see Fig. 3.1). It can be written as below:

$$\begin{aligned} \omega_p &= \omega_i + \omega_s \\ \vec{k}_p &= \vec{k}_i + \vec{k}_s \end{aligned} \tag{3.4}$$

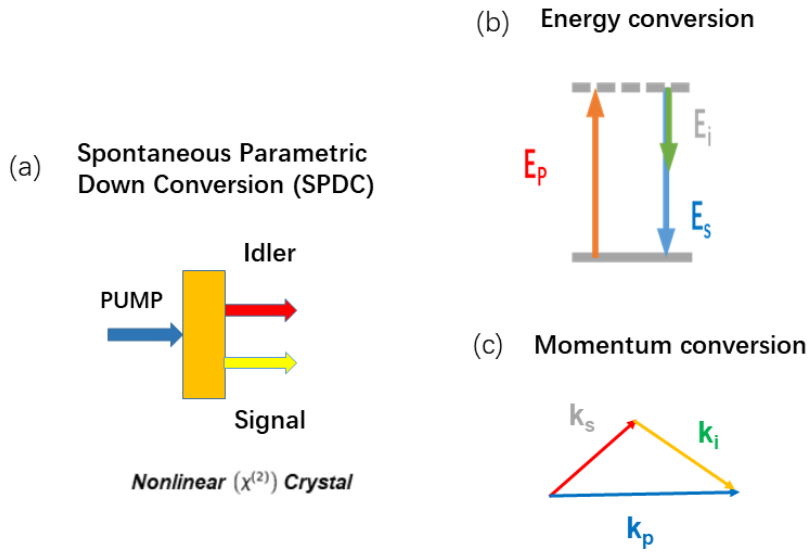

Figure 3.1: Conservation law of the SPDC process. (a) SPDC process: a pump light with higher frequency generate a pair of photons lower frequency by interacting with a second order nonlinear material. (b), (c), This SPDC process need to fuifil energy conversion and momentum conversion.

Where ω and $\vec{k}$ represent the frequency and wave vector of the pump light (p), signal light (s), and idle light (i).

The energy conservation determines the possible wavelength of the down-converted photon pairs, while the momentum conservation condition, or also known a phase-matching condition, determines the direction of the down-converted photons [70]. Different techniques to achieve phase-matching will be discussed in the following sections.

In the experiments described in this thesis, we also used another common $\chi^{(2)}$ second-order nonlinear optical processes Second Harmonic Generation (S H G), which is the simplest of the second-order nonlinear processes.

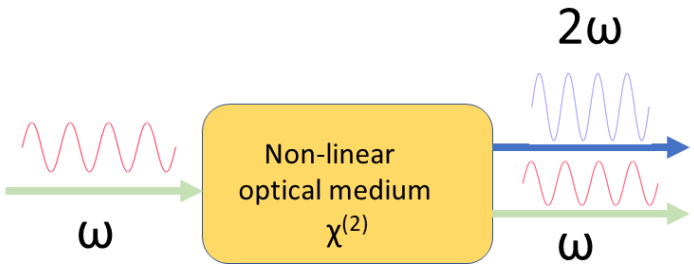

Figure 3.2: Second Harmonic Generation. Second harmonic generation (SHG) is a nonlinear optical process in which the input frequency interaction with a $\chi^{(2)}$ nonlinear material is doubled $(\omega \rightarrow 2\omega)$.

.

From Eq.3.1, we have

$$\begin{aligned} P^{(2)}(2\omega) &= \varepsilon_0 \chi^{(2)} E^2(\omega) \\ &= \varepsilon_0 \chi^{(2)} * E_0 e^{-i\omega t} * E_0 e^{-i\omega t} \\ &= \varepsilon_0 \chi^{(2)} * E_0^2 e^{-i2\omega t} \end{aligned} \tag{3.5}$$

Eq.3.5 shows that an incident electric field at frequency ω generates, depending on its strength, a second-order nonlinear polarization at frequency 2ω [87]. It was shown in Fig. 3.2.

3.2 Phase matching

In the previous section, we discussed that the conservation of momentum must be satisfied in the process of SPDC, which also means the conditions for phase matching should be fulfilled. So, in this section, we will specifically introduce some basic concepts and commonly used methods to achieve phase matching.

In the PDC process, in terms of the electromagnetic theory of light, the optical field of the

pump, signal, and idle light can be expressed by [74]:

$$\begin{aligned}\vec{E}_1(z,t) &= A_1 e^{i(k_1 z-\omega_1 t)} + c.c \\ \vec{E}_2(z,t) &= A_2 e^{i(k_2 z-\omega_2 t)} + c.c \\ \vec{E}_3(z,t) &= A_3 e^{i(k_3 z-\omega_3 t)} + c.c\end{aligned} \tag{3.6}$$

Where E_1, E_2 and E_3 are the amplitudes of the EM fields of pump light, signal light, and idle light, respectively, A is the amplitude of the light wave. In this process, it is assumed that the light propagation direction is along the z-axis direction. This process can be represented by Fig. 3.1 (a).

In the process of SPDC, the interaction between the light fields of the three beams can be obtained by a series of calculations, and we can find coupled wave equation [74].

$$\begin{aligned}\frac{d^2A_1}{dz^2} + 2ik_3\frac{dA_1}{dz} &= -\frac{4d_{eff}\omega_3^2}{c^2}A_2A_3e^{i(k_1+k_2-k_3)z} \\ \frac{d^2A_2}{dz^2} + 2ik_3\frac{dA_2}{dz} &= -\frac{4d_{eff}\omega_3^2}{c^2}A_1A_3e^{i(k_1+k_2-k_3)z} \\ \frac{d^2A_3}{dz^2} + 2ik_3\frac{dA_3}{dz} &= -\frac{4d_{eff}\omega_3^2}{c^2}A_1A_2e^{i(k_1+k_2-k_3)z}\end{aligned} \tag{3.7}$$

Where d_{eff} is the effective polarization coefficient which depends on the strength of the non-linearity of the material and geometrical factors [74]. The third equation can be reduced by considering the slowly varying amplitude approximation and hence ignoring the first term on the left-hand side of this equation, which leads to:

$$\frac{dA_3}{dz} = \frac{2id_{eff}\omega_3^2}{k_3c^2}A_1A_2e^{i\Delta kz} \tag{3.8}$$

Where Δkz is phase-mismatch. We can easily find the solutions of Eq 3.8 by integration from 0 to L (length of the crystal):

$$A_3(L) = \frac{2id_{eff}\omega_3^2}{k_3c^2}A_1A_2\int_0^L e^{i\Delta kz}dz = \frac{2id_{eff}\omega_3^2}{k_3c^2}A_1A_2\left(\frac{e^{i\Delta kL}-1}{i\Delta k}\right) \tag{3.9}$$

Here considering that $I_i = 2n_i\varepsilon_0 c\,|A_i|^2$ is the optical intensity of idler beam I [8]:

$$I_3 = \frac{8d_{eff}^2\omega_3^2 I_1 I_2}{n_1 n_2 n_3 \varepsilon_0 c^3} L^2 \left(\frac{\sin\Delta k\cdot L/2}{\Delta k\cdot L/2}\right)^2 = I_3^{\max}\cdot \sin c^2(\Delta k\cdot L/2) \tag{3.10}$$

Where $\Delta k = k_1 + k_2 - k_3$ is called the phase-matching parameter. From Eq 3.10, we know that to increase the intensity, the only way is to allow $\Delta k = 0$ to maximum the Sinc function. This phase-matching condition is essential for an efficient non-linear effect. To fulfill the phase-matching condition, one must have:

$$k_1 + k_2 = k_3 = \frac{n_3\omega_3}{c} = \frac{n_1\omega_1}{c} + \frac{n_2\omega_2}{c} \tag{3.11}$$

It is very difficult to achieve a perfect phase-matching condition for most materials as $n_1(\omega_1) < n_2(\omega_2) < n_3(\omega_3)$ for $\omega_1 < \omega_2 < \omega_3$, i.e. for "normal" dispersion. Fortunately, there are some different techniques to achieve phase matching, in which the use of the birefringence of the crystal itself to reach phase matching is a common way in experiments, mainly using the difference of the refractive index of o (ordinary) light and e (extraordinary) light in the birefringent crystal to select the crystal type and incident light angle. In the specific case of second-harmonic generation, we have $n_e(\omega_1) = n_o(\omega_3 = 2\omega_1)$. Alternatively, for some crystals, the amount of birefringence is strongly temperature-dependent, and so it may be possible to achieve phase-matching by tuning the temperature of the crystal [70, 72].

In this thesis, we use periodically poled lithium niobate(PPLN) waveguide, which will be introduced in the next section. To better calculate the brightness, Eq.3.10 needs to be adapted to the 1 dimensional problem, modify the idler down-converted intensity to power, and rewritten as [85]:

$$\mathrm{d}P_i = \frac{16\pi^3\hbar d_{\mathrm{eff}}^2 L^2 c P_p}{\varepsilon_0 n_i n_s n_p \lambda_i^4 \lambda_s}\frac{1}{A_{WG}}\,\mathrm{sinc}^2\left(\frac{\Delta kL}{2}\right)\mathrm{d}\lambda_i \tag{3.12}$$

Where we rewrote waveguide mode index as n_k at wavelength λ_K for subscript K of signal s, idler i, or pump p, and A_{WG} is the cross-section of the waveguide.

The main difference between the bulk crystal and waveguide crystal is that the pump interacts with a continuum of plan wave modes in a bulk crystal, whereas in the waveguide only several spatial modes of the propagating pump, signal and idler photons interact, corresponding to their respective wavelengths. [84] The waveguide emission is restricted to a limit band as a result of the sinc-squared function. In contrast, the bulk SPDC emission theory predicts that far from collinear emission, the spectral density is nearly flat, as experimentally proved in [85][84]. Based on the density of states model, this spectral difference results from the fact that waveguide SPDC is fundamentally a 1- dimensional problem. In contrast, the bulk needs to be handled as a 3-dimensional case. A brighter waveguide SPDC emission compared with the bulk indicates that a waveguide can increase mode overlap between the pump, signal, and idler. Hence, the interaction between the three fields can be enhanced [84].

Based on this theory, the SPDC flux of the waveguide source can be estimated. The pump laser we are using is a $\lambda_p = 766.2885$ nm, continuous-wave laser, which generated the degenerate output at $\lambda_{s,i} = 1532.577$ nm. The length of our PPLN waveguide is 5.3 mm. The cross-section of the waveguide was approximately $A_{WG} \simeq 75.0\ \mu\text{m}^2$. The refractive indices for the pump, idler and signal photon are estimated at $n_p = 2.18269, n_s = 2.14081, n_i = 2.14081$, respectively.

Here we use the nonlinear coefficient listed in Tab 3.1, which gives the type-0 PPLN waveguide crystal $d_{33} = 30$ pm/V. d_{33} is the highest nonlinear coefficient, which corresponds to interactions that are parallel to the z-axis, such as type-0 phase match [187]. Using Eq.(3.12), we calculate the pair generation rate of our waveguide source to be $\sim 2.70 \times 10^9$ pairs/s/mW of pump power over the entire band without a cavity. The calculated spectrum of the signal photon is shown in Fig. 3.3.

Here, we introduce an important concept: the Joint spectral amplitude (JSA) which can characterizes the structure and joint spectrum of the generated photons. From JSA we can obtain information about the different degrees of freedom of the photon pairs and their quantum correlations.

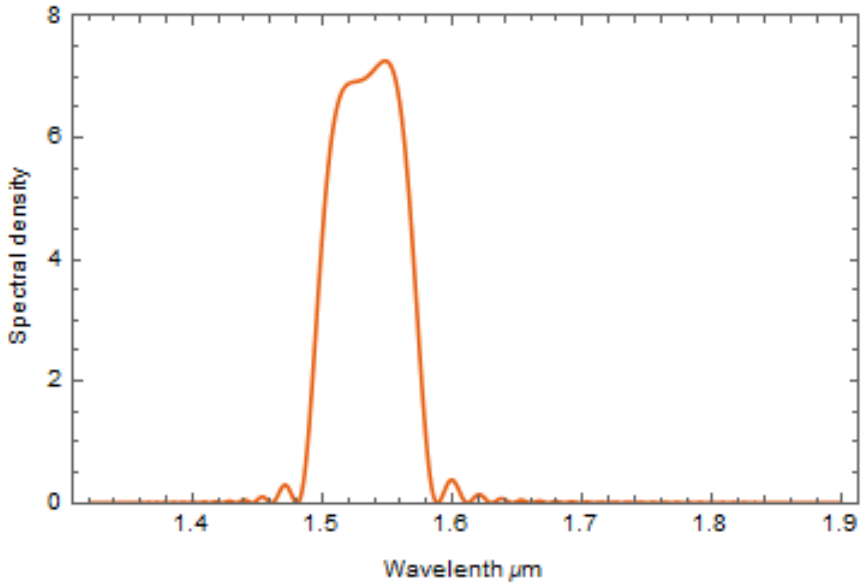

Figure 3.3: Theoretical signal spectral power density of the PPLN waveguide per nm with 1 mW pump power calculated from Eq.(3.12).

Table 3.1: Types of SPDC for generating photon pairs in PPLNW.

Interaction type	type-0	type-I	type-II
Polarization	$\|V\rangle_p \rightarrow \|V\rangle_s \|V\rangle_i$	$\|V\rangle_p \rightarrow \|H\rangle_s \|H\rangle_i$	$\|H\rangle_p \rightarrow \|H\rangle_s \|V\rangle_i$
$\chi^{(2)}$ coeff. of LiNbO3	$d_{33} \approx 30\text{pm/V}$	$d_{31} \approx -5\text{pm/V}$	$d_{24} \approx 10\text{pm/V}$
η_{SPDC} in	$10^{-6} - 10^{-5}$	10^{-7}	10^{-9}
$\Delta\lambda$ at 1550nm	$20 - 100\text{nm}$	$20 - 100\text{nm}$	$0.8 - 3\text{nm}$
$\Delta\nu$ at 1550nm	$2.5 - 12.5\text{THz}$	$2.5 - 12.5\text{THz}$	$0.1 - 0.375\text{THz}$
Natural entanglement	Energy-time	Energy-time	Polarization

[169] The JSA of signal and idler photons defined as:

$$f(\omega_s, \omega_l) = \alpha(\omega_s + \omega_l)\, \phi(\omega_s, \omega_l) \tag{3.13}$$

Where $\alpha(\omega_s + \omega_l) = e^{-\left(\frac{\omega_s + \omega_l - \omega_p}{\sigma_p}\right)^2}$ is the pump envelope function, which we consider to be a Gaussian function and $\phi(\omega_s, \omega_l)$ is the phase-matching function, which function which is expressed as:

$$\phi(\omega_s, \omega_l) = \text{sinc}\left[\Delta\beta(\omega_{s,}, \omega_l)\frac{l}{2}\right] \exp\left(i\Delta\beta(\omega_s, \omega_l)\frac{l}{2}\right) \tag{3.14}$$

Where $\Delta\beta(\omega_s,\omega_l)=\beta(\omega_s+\omega_l)-\beta_s(\omega_s)-\beta_i(\omega_i)-\beta_{QPM}$ is the phase-matching condition in the waveguide, and $\beta_{p,s,i}=\frac{2\pi}{\lambda_{p.s,i}}n_{p,s,i}$ is the wave vector of the pump, signal and idler, respectively corresponding to the effective indices $n_{p,s,i}$ of the same inside the waveguide. Here, $n_{p,s,i}$ also is known as effective refractive index denotes as n_{eff}, which is wavelength-dependent parameter. The joint spectral amplitude (JSA) is a very important concept that encodes the complete spectra-temporal structure of the two-photon state[84].

3.2.1 Quasi phase-match

We discussed in the previous section that a perfect phase-matching condition is difficult to achieve; however, there is a better way to achieve phase-matching called quasi-phase-matching, which was proposed by J.A.Armstrong, N.Bloembergen in 1962 [75]. This technique mainly takes advantage of nonlinear crystal periodic structure, using the spatial reciprocal vector provided by this structure to compensate for the phase mismatch and thus to achieve phase-matching by adjusting the polarization period [76].

This technique reverses the polarization direction at both ends of the domain wall, that is, a phase factor of π is introduced to achieve the purpose of spatial modulation, as shown in Fig 3.3. This process also changes the spatial distribution of d_{eff}. For a medium with a periodic modulation of the nonlinear susceptibility with period Λ and thus fundamental spatial frequency $K_g=2\pi/\Lambda$, we can expand the nonlinear susceptibility as a Fourier series [78].

$$d(z)=d_{eff}\sum_{m=-\infty}^{\infty}g_m e^{ik_m z} \tag{3.15}$$

Where the mth spatial harmonic $K_m=mK_g$, for a square-wave modulation from $+d_{\text{eff}}$ to $-d_{\text{eff}}$, a standard Fourier series result gives $g_m=\frac{2}{m\pi}\sin\frac{mn}{2}$ [78]. Thus, we have

$$\begin{cases} k_m=\frac{2\pi m}{\Lambda} \\ g_m=\frac{2}{m\pi}\sin\frac{m\pi}{2} \end{cases} \tag{3.16}$$

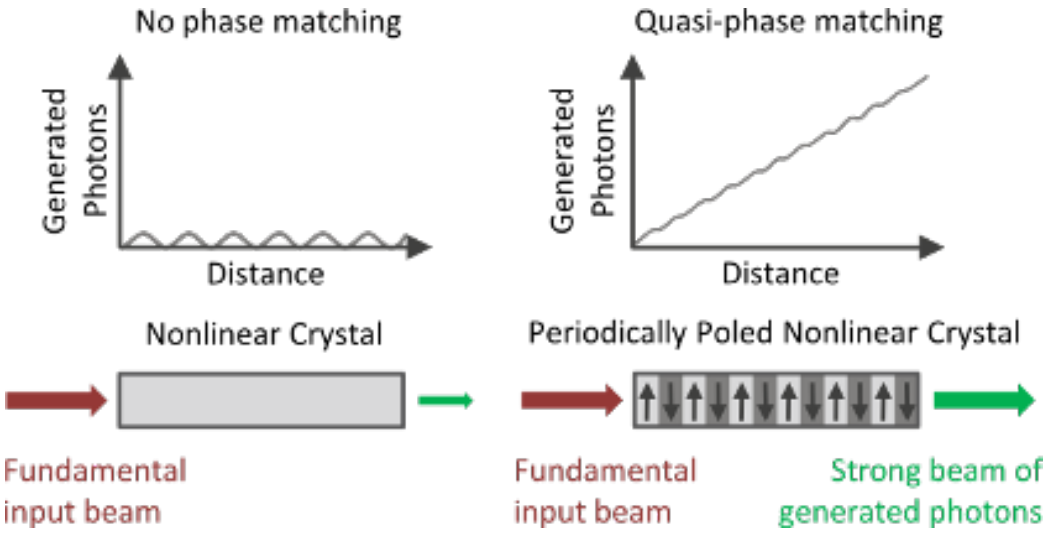

Figure 3.4: The principle of Quasi-phase-matching. Periodic poling allows for quasi phase matching. The polarization direction at both ends of the domain wall was reversed by introduced a phase factor of π to achieve the purpose of spatial modulation, which maintains phase relation of the photons throughout the crystal where they would otherwise fall out of phase.[77]

Substituting this equation into the coupled wave equation represented by Eq.3.8 can yield: :

$$\frac{dA_3}{dz} = \frac{2id_{eff}\omega_3^2 G_m}{k_3 c^2} A_1 A_2 e^{i\left(\Delta k + \frac{2\pi m}{\Lambda}\right)z} \tag{3.17}$$

It can be seen from Eq.3.13 that the phase term becomes $\Delta k + \frac{2\pi m}{\Lambda}$, so in order to achieve phase matching, the polarization period needs to satisfy:

$$\Lambda = \frac{2\pi m}{k_3 - k_2 - k_1}, \quad m = 1,3,5\ldots \tag{3.18}$$

As a result of the Sellmeier equations, thermal expansion and the periodicity constant carry a temperature dependence, and the entire phase-matching process is highly temperature-dependent. So, by adjusting the temperature accordingly, slight deviations from the optimal crystal periodicity can be compensated. This method is known as temperature-tuning. Examples for the temperature dependence of the phase mismatch as shown in Fig. 3.5.

The above discussion shows that the difficulty in achieving phase matching can overcome by periodically reversing (periodically poling) the polarity over the entire length of the nonlinear crystal, thus assuring the number of generated photons will grow as the light propagates through

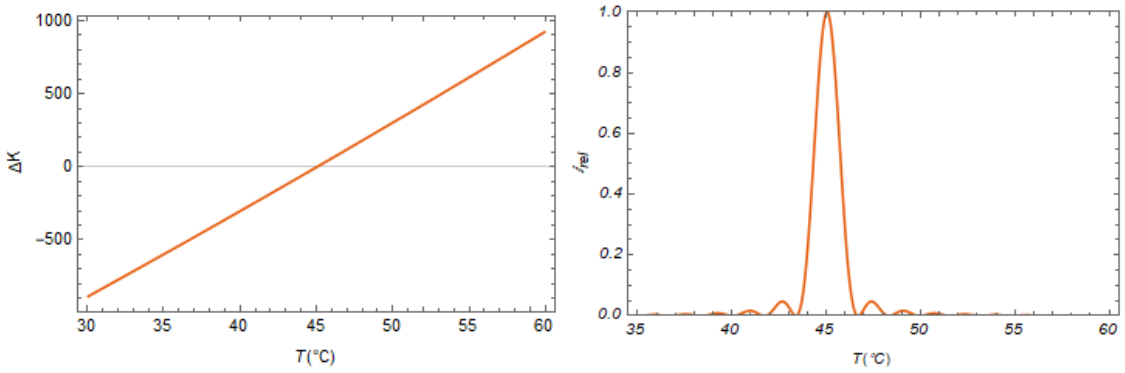

(a) a (b) b

Figure 3.5: Illustration of temperature-tuning. Type 0 down-conversion $(e \rightarrow e+e)$ from 766.3 nm to 1532.3 nm and 1532.9 nm. The periodicity was set to 18.4μm. Figure (a) shows the wavevector mismatch as a function of T; Figure (b) shows the output intensity with respect to T. Both figures indicate that for this specific setup, phase-matching is achieved at $T \approx 45°$C

the crystal.

3.2.2 Periodically Poled Lithium Niobate

With the development of quantum communication, a substantial effort was made to prepare and improve entanglement sources. Significant advances have been made in phase-matching technology and looking for various nonlinear crystal materials. The nonlinear crystal is crucial to generate photon-pair sources via the SPDC process. Different kinds of crystals have been exploited to generate photon pairs, such as KDP [79], BBO [80]. In the previous section, we introduced the quasi-phase match and periodical poling technique which is widely used in lithium-niobate (LiNbO3) crystals that allow access to one of the largest nonlinear coefficients existent amongst all known materials [70]. In the work presented in this thesis, we use periodically poled lithium-niobate (PPLN) crystals to generate photon pairs.

PPLN is an engineered, quasi-phase-matched material. An essential step in the production of PPLN is the inversion (polarization) of the lithium niobate crystal structure. Lithium niobate is a ferroelectric crystal, which means each unit cell has a small electric dipole moment. The dipole orientation in a unit cell depends on the position of the niobium and lithium ions in that unit cell.

The electric field required to flip the crystal structure is very large, about 22 KV/mm. It was only applied for a few milliseconds, after which the inverted parts of the crystal have permanently remained in the crystal structure. The production of PPLN requires the deposition of a periodic electrode structure on a lithium niobate wafer, and a voltage is applied to invert the crystal underneath the electrodes [81]. The specific preparation process can be divided into three main steps [82], as shown in Fig. 3.6.

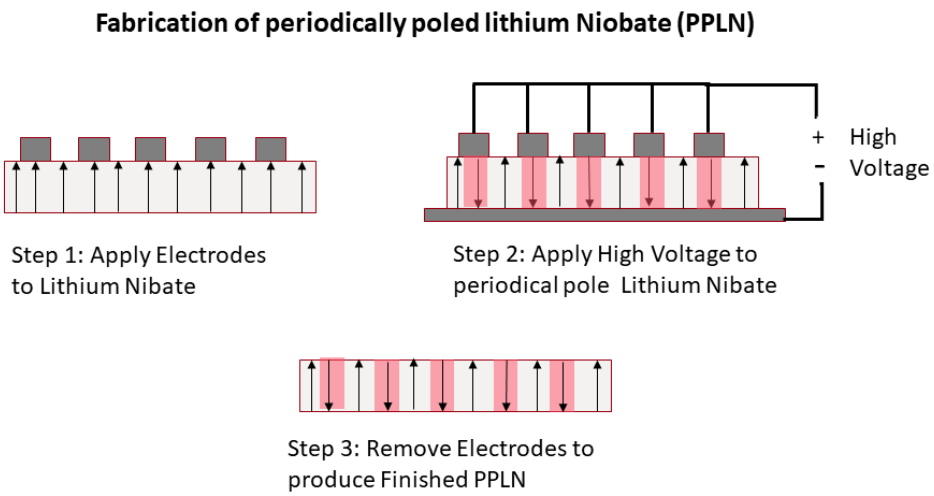

Figure 3.6: The process of preparing the PPLN crystal.[82]

To date, the generation of photon pairs in periodically poled crystal mainly exploits the three main interaction types that relate to the polarization states of the pump, signal, and idler photons (see Tab.3.1) [83]. For this thesis, we use type-0 PPLN to generate photon pairs at telecom wavelength.

Chapter 4

Spectrally Multi-mode Photon Pair Source

In previous chapters, we discussed that multiplexing is a promising scheme to improve transmission rate in quantum communications experiments, and three essential components of frequency multiplexed quantum repeater were introduced. In this chapter, details on the cavity engineering of the spectrally multi-mode photon pair source, which is the key component of FMQR, will be given.

4.1 Cavity design of the parametric module

The optical cavity consists of a set of cavity mirrors, whose optical axis usually coincides with the long axis of the working medium in the cavity. Thus, the light in the resonant cavity will be reflected back and forth between the mirrors of the cavity, passing through the working medium multiple times so that the intensity of the light is continuously enhanced. At the same time, as a result of the cavity boundary condition of the electromagnetic field mode, it has many discrete eigenmodes, which offer possibilities to allow it to work as a spectrum filter as well as the laser frequency calibrator. In this study, a PPLN waveguide with end-face dielectric multi-layer reflective mirrors at telecom wavelengths was used to prepare the cavity-enhanced photon pair source and realized the spectrally multi-mode output. The fundamental theory will be given in detail in the following subsections.

4.1.1 Theory of optical cavity

Consider a simple optical cavity with a cavity length of L. The frequency of the input beam is $\omega = 2\pi \cdot \nu$ and its wave function given

$$E(\mathbf{r},t) = A(\mathbf{r})e^{i\omega t} \tag{4.1}$$

Where the the complex amplitude $A(\mathbf{r})$ fulfilled the Helmholtz equation[108]

$$\nabla^2 A(\mathbf{r}) + k^2 A(\mathbf{r}) = 0 \tag{4.2}$$

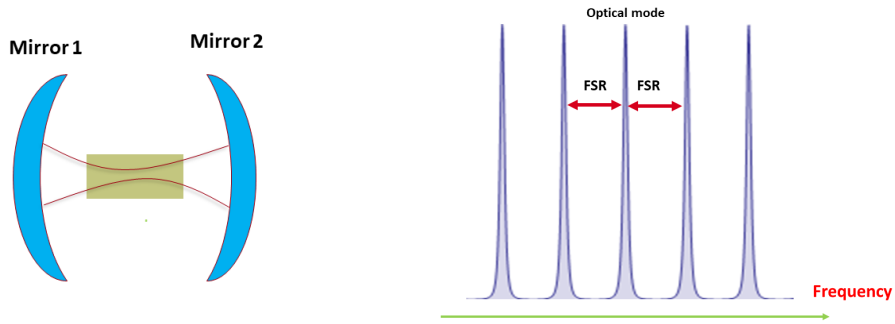

(a) Cavity (b) Free spectral range

Figure 4.1: Optical Cavity.

Whereas wave number $k = \omega/c$, c is the speed of light in a vacuum. By solving the Helmholtz equation above, we can see that the optical wave is a series of standing waves in the longitudinal direction of the optical cavity and can be expressed as $A(\mathbf{r}) = A\sin(kz)$ which satisfied $kL = q\pi$ and q is an integer. Thus the general solution of the mode in the optical cavity is

$$A(\mathbf{r}) = \sum_q A_q \sin\left(k_q z\right) \tag{4.3}$$

whereas A_q is a constant. $k_q = q\frac{\pi}{L}, (q = 1,2,\dots)$. The modes of the cavity are separated in frequency by a free spectral range (FSR) (see Fig.4.1 (b)).

$$FSR = \frac{c}{2L} \tag{4.4}$$

Where c is the speed of light, L is the cavity length. If the refractive index of the nonlinear medium in the cavity is n, Eq.4.4 can be rewritten as

$$FSR = \frac{c}{2nL} \tag{4.5}$$

The phase (φ) of each mode should be shifted $2q\pi$ (q is an integer number) with each round trip in the cavity. Consider the reflectivity of the cavity mirror is not ideal ($(R \neq 1)$, the amplitude of the optical wave of each trip in the cavity is a complex factor $h = \sqrt{R}e^{-i\varphi}$. Then after n trips, when $n \to \infty$, the amplitude of optical wave becomes

$$A = \sum_n h^n A_0 = \frac{A_0}{1-h} \tag{4.6}$$

Where A_0 is the initial amplitude. Then the relationship between the light intensity in the optical cavity and the frequency of the light wave f can be expressed as

$$I = |A|^2 = \frac{I_0}{(1-\sqrt{R})^2\left(1+(2F/\pi)^2\sin^2(\pi f/FSR)\right)} \tag{4.7}$$

where $I_0^2 = |A_0|^2$, F is the fineness of the cavity, which reflects the quality of the cavity.

$$F = \frac{\pi\sqrt{\sqrt{R}}}{1-\sqrt{R}} \tag{4.8}$$

In practical situations, the reflectivity of the cavity mirror is not always the same. Especially in our experiments, the cavity mirror's reflectivity needs to be designed according to the required multi-photon output. For the more general case, the fineness is [88]

$$F = \frac{\pi}{2\arcsin\left(\frac{1-\sqrt{\rho}}{2\sqrt[4]{\rho}}\right)} \tag{4.9}$$

where ρ is denoted to the power in the cavity after a round trip and can be written as $\rho = R_1 R_2 10^{-2\alpha L/10}$, R_1 and R_2 are the reflectivity of the mirrors, α is the absorption coefficient expressed in dBcm^{-1} .

Another quantity, F_0, can be defined as $F_0 \approx \frac{2\pi}{t_{op}}$ ($t_{op} = 1 - R_2$). The quantity F_0 is the bounding limit of the finesse for the output power since any other loss will reduce the output power and the cavity finesse.

4.1.2 Theory of cavity-enhanced spontaneous parametric down-conversion

Spontaneous parametric down-conversion (SPDC) is a spontaneous nonlinear process induced by the vacuum field effect. When the parametric down-conversion crystal is inserted into an optical cavity since the optical cavity changes the mode of the vacuum field in the cavity, only the nonlinear process matching the cavity mode can enhance. In contrast, the other modes will be suppressed [95, 96, 97, 98]. By doing so, one can be benefited from enhanced emission into some desired modes without extra filter loss, which is crucial for building a spectrally multimode photon pair source that is the main objective in this thesis. This type of SPDC setup is also called an optical parametric oscillator (OPO). Aside from engineering desired modes output, another benefit of using OPOs is that the effective length of the crystal increases since the pump passes the crystal multiple times; thus, the spectral brightness will enhance [90].

Generally, there are three types of resonance for an OPO, including singly resonant OPO, whereby only the signal is resonant,, doubly resonant if both signal or idler and pump are resonant simultaneously, and triple resonant if signal, idler, and pump are achieved at the same time [91]. The latter two often requiring active stabilization techniques [91].

In practical quantum information and communication experiments, an integrated device [92, 93, 94] provides many advantages. As described above, doubly resonant usually requiring challenging stabilization techniques. In a monolithic design, such as the one provided by a PPLN waveguide integrated cavity, only the temperature needs to be stabilized. By changing the temperature, the device can be phase-matched for different wavelengths [90].

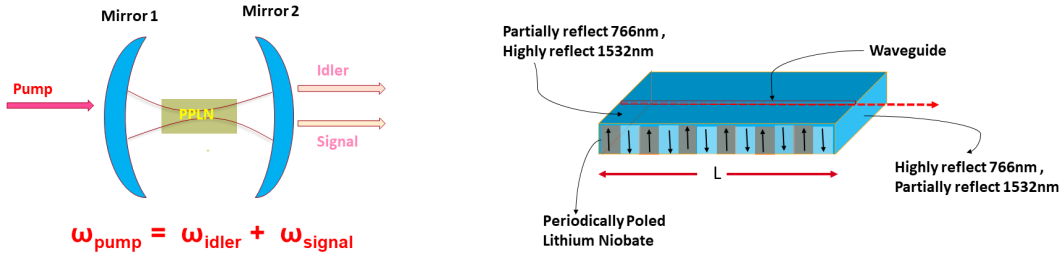

(a) (b)

(c)

Figure 4.2: Spontaneous down conversion in cavity. (a) Optical cavity with non-linear crystal included. (b) An integrated cavity-waveguide by reflection coating mirrors at the end face of a periodically poled nonlinear material. (c) Picture of cavity-waveguide chip used in this work with red light coupled to the waveguide through input and output optical fibers.

In this thesis, a doubly resonant OPO (DR-OPO) structure is employed, including a based periodically poled lithium niobate (PPLN) crystal as shown in Fig. 4.2 (b). The input facet is coated with a high reflection mirror at the signal, idler wavelengths, and high transmission at the pump. And the exit facet is coated with the mirror that has reflectivity enough for obtaining the desired finesse but low enough to be the dominant loss mechanism [90]. In this work, we used a waveguide chip that includes 10 waveguide channels with different phase match features, one channel as shown in Fig. 4.2 (c).

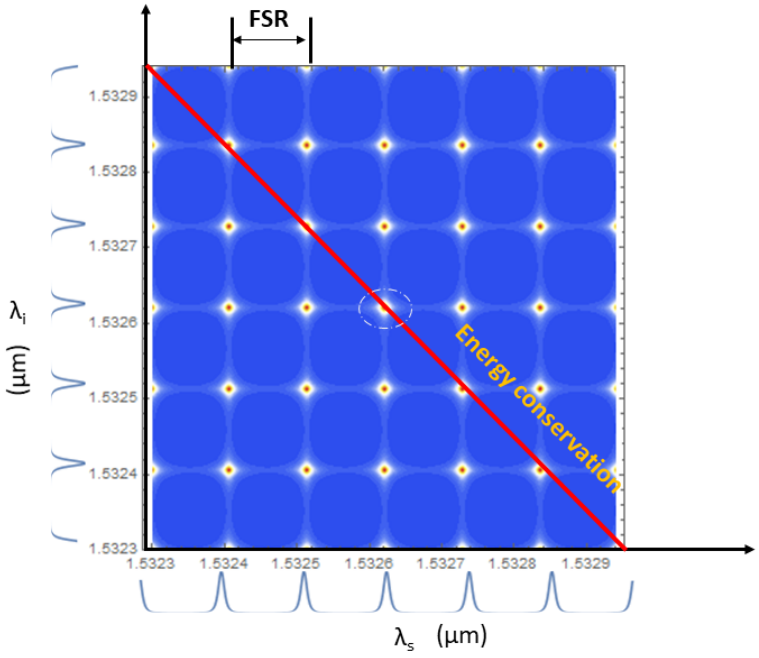

Figure 4.3: Cavity-waveguide. Correlations in a doubly resonant SPDC source where energy conservation (diagonal line) and resonance can be satisfied for a large number of adjacent cavity modes.

Now consider the state of the photon pairs emitted by a DR-OPO is represented by [99]

$$|\Psi\rangle_{\mathrm{OPO}} = \int \mathrm{d}\omega_{\mathrm{s}} \int \mathrm{d}\omega_{\mathrm{i}} S(\omega_{\mathrm{s}}, \omega_{\mathrm{i}})\, a_{\mathrm{s}}^{\dagger}(\omega_{\mathrm{s}})\, a_{\mathrm{i}}^{\dagger}(\omega_{\mathrm{i}})\, |vac\rangle \tag{4.10}$$

where $S(\omega_{\mathrm{s}}, \omega_{\mathrm{i}})$ is the Joint Spectral Intensity (JSI) [90],

$$S(\omega_{\mathrm{s}}, \omega_{\mathrm{i}}) = |f(\omega_{\mathrm{s}}, \omega_{\mathrm{i}})|^2 \mathscr{A}_{\mathrm{s}}(\omega_{\mathrm{s}})\, \mathscr{A}_{\mathrm{i}}\left(\omega_{\mathrm{i}} = \omega_{\mathrm{p}} - \omega_{\mathrm{s}}\right) \tag{4.11}$$

Here $f(\omega_s, \omega_i)$ denotes the joint spectral amplitude without cavity, which was introduced in the previous chapter. $\mathscr{A}_j(\omega_j)$ are the airy functions for the signal and the idler photons, which, as functions of the wavelength, are written as [90].

$$\mathscr{A}_j(\lambda_j) = \left[1 + \frac{4\sqrt{R_1 R_2}}{(1-\sqrt{R_1 R_2})^2} \sin^2(\phi_j)\right]^{-1} \tag{4.12}$$

where $\phi_j = 2\pi L n_{\text{eff}}(\lambda_j)/\lambda_j$.

For the degenerate SPDC, as a result of the refractive index being equal for both signal and idler photons, the airy functions will be the same for both photons. The distance between the peaks will be defined by the FSR of the cavity [90].

While for non-degenerate, the FSR at the signal and idler will be different given that they have different dispersion characteristics. In this situation, simultaneous resonance for both the signal and the idler happens only in regions of the spectrum where the peaks of the FabryPerot for the signal and the idler align [90]. These regions are called clusters [111, 112] since they consist of many peaks.

As mentioned earlier, when the down-conversion crystal is placed inside a cavity, photons can only be emitted in modes that resonate by the resonator. For a FabryPerot cavity, the resonant modes are given by the airy function [90]. This restraint on the joint frequency spectrum is shown in Fig. 4.3. In the next subsection, more detail about the cavity design in this thesis will be given. In order to design an integrated waveguide resonant multi-mode photon pair source with specific finesse, we have to know the absorption coefficient and optimize the length of the crystal L and the second mirror reflection R_2 to take account of the loss inside the crystal [90]. We can calculate the probability p_{out} by assuming that photons are generated in the middle of the resonator after a number n of round-trips is given by $10^{-(\alpha/2)L/10}(1-R_2)\left(R_1 R_2 10^{-2\alpha L/10}\right)^n$. So, the probability

that each photon exits the cavity can be given as [90]

$$\begin{aligned} p_{\text{out}} &= 10^{-(\alpha/2)L/10}(1-R_2)\sum_{n=0}^{\infty}\left(R_1R_2 10^{-2\alpha L/10}\right)^n \\ &= \frac{10^{-(\alpha/2)L/10}(1-R_2)}{1-R_1R_2 10^{-2\alpha L/10}} \end{aligned} \tag{4.13}$$

α is the absorption coefficient, and αL is the absorption losses for a single pass inside the cavity. The probability p_{out} largely depends on the length L of the waveguide resonator. For a bigger value of L, the probability p_{out} decreases. Thus, shorter crystals give less loss and a large FSR, which is easier for selecting a single spectral mode [90].

Note that the two-photon state produced by cavity-enhanced parametric down-conversion is quite similar to the two-photon state of conventional spontaneous parametric down-conversion, placing a cavity after the nonlinear crystal. Still, the pump beam only interacts with the crystal in a single pass. In addition, the brightness of a photon pair source spectral filtering with a cavity after the crystal is lower than the brightness of a cavity-enhanced photon-pair source with the same cavity linewidth [89]. The average enhancement factor per mode in a DR-OPO is given by [102].

$$B = F^3/2F_0 \tag{4.14}$$

Where F is the cavity fineness, and F_0 is the cavity finesse without any loss. For waveguide SPDC, the spectral brightness is inversely proportional to the mode overlap area A_I (see section 3.2 in chapter 3), and the field confinement could lead to an enhanced pair generation rate [110]. The enhancement factor is given by [110]

$$\Gamma_{\text{enhance}} \simeq \frac{\lambda_{si}L}{\pi n_{si}A_{\text{I}}} \tag{4.15}$$

Whereas λ_{si} is signal and idler wavelength, respectively, n_{si} is the refractive index of signal and wavelength, respectively.

4.2 Numerical simulation and cavity design

The main objective of this thesis is to generate a spectrally multi-mode photon pair via the clustering effect. To realize this goal, the clusters must contain at least five spectral modes distributed in specific wavelengths from 1532 to 1533 nm or 1533to 1534 nm, which matches with our later erbium memory experiment, and the FSR should be large enough to be able to select individual desired modes using low-loss filters.

In the previous section, we introduced JSI, whose shape is known as the intersection of pump envelope and phase match, as shown in Fig. 4.4. By multiplying the airy function for the idler and signal photons whose frequencies are decided by the energy conservation, the emission spectrum can be modeled. The wavelength dependency of the effective refractive index for PPLN is given by the Sellmeier equations in [100] already consider the waveguide dispersion. The pump wavelength operates at around 766.3 nm, which gives the generation of photon pairs degenerate around 1532.6 nm. The bandwidth of the down-conversion set by the phase mismatching function $|\phi(\omega_s, \omega_i)|^2$ is shown in Fig. 4.5. By slightly tuning the pump wavelength, varied output frequency can be achieved.

In our experiment, we use a type 0 PPLN waveguide with length $L = 5.3$ mm. By choosing the appropriate reflective coefficient for the two-cavity mirrors, one can obtain the desired multi-photon output. Fig. 4.6 shows the joint SPDC spectra intensity by different mirror reflection coefficients. To guarantee relatively high intensity and GHz linewidth level that can match with later AFC quantum memory, we ultimately set the end facet mirror coating reflectivity with $R_1 = 99.5$ %, $R_2 = 45$ %. The pump wavelength operates at around 766.3 nm,, which gives the generation of photon pairs degenerate around 1532.6 nm. The bandwidth of the down-conversion set by the phase mismatching function $|\phi(\omega_s, \omega_i)|^2$ is shown in Fig. 4.5. By slightly tuning the pump wavelength, varied output frequency can be achieved. The JSI Contour shown in Fig. 4.7 illustrates the JSI shape at $T = 61.7$ °C, this cavity allows 11 modes output in the wavelength ranging from 1532 nm to 1533 nm. Tuning the temperature gives different phase matching due to the

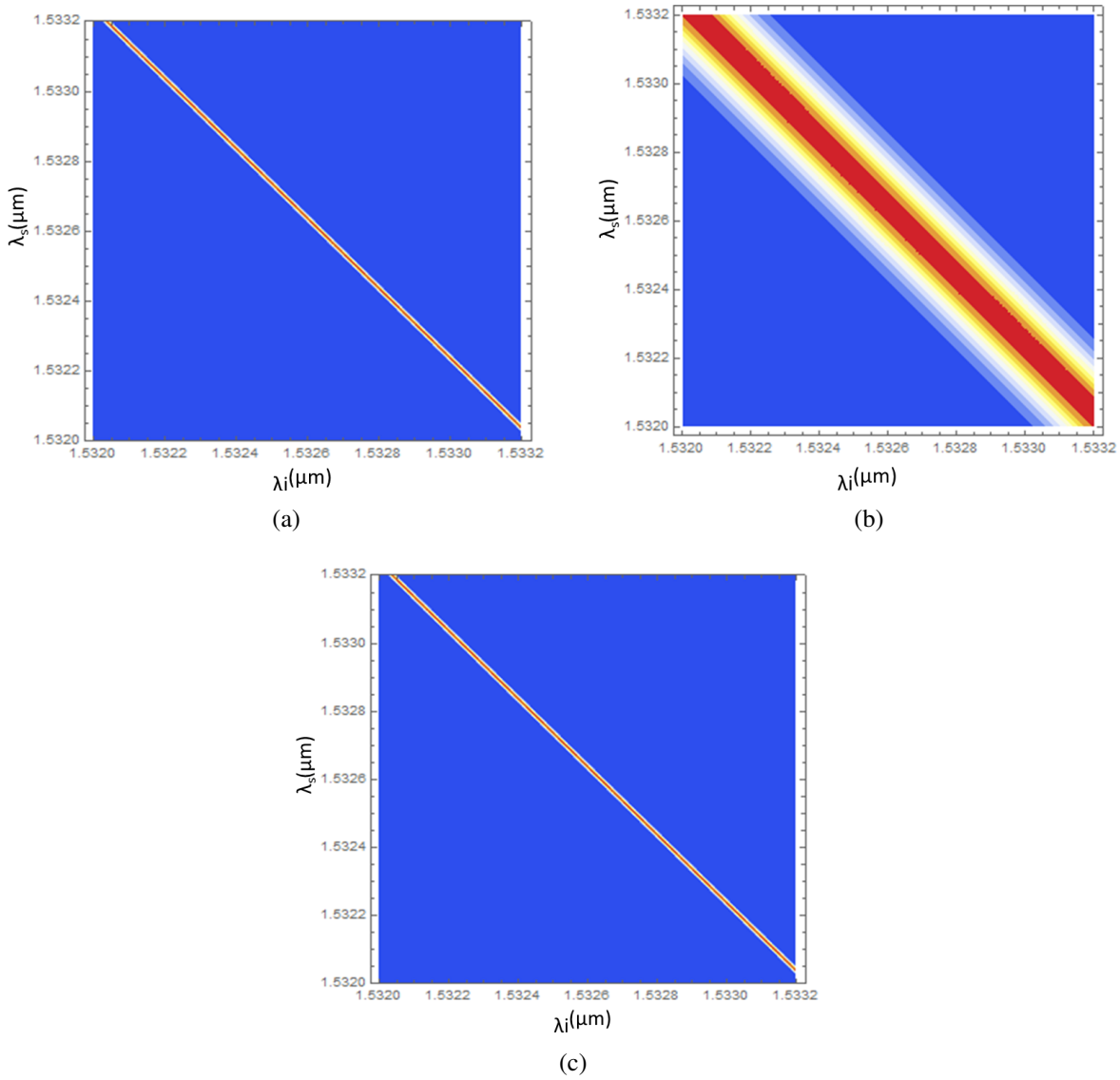

Figure 4.4: JSI without cavity. Example of phase-matching intensity $|\phi(\omega_s,\omega_i)|^2$ (a), pump envelope intensity $|\alpha(\omega_s+\omega_i)|^2$ (b) and JSI $|f(\omega_s,\omega_i)|^2$ (c). The three figures illustrate a type 0 down-conversion from 766.31 *nm* to 1532.62 *nm* in LN. We see that if the pump envelop has wider bandwidth and overlap with the phase-matching, then the output fields are mainly dependent on the phase-matching.

.

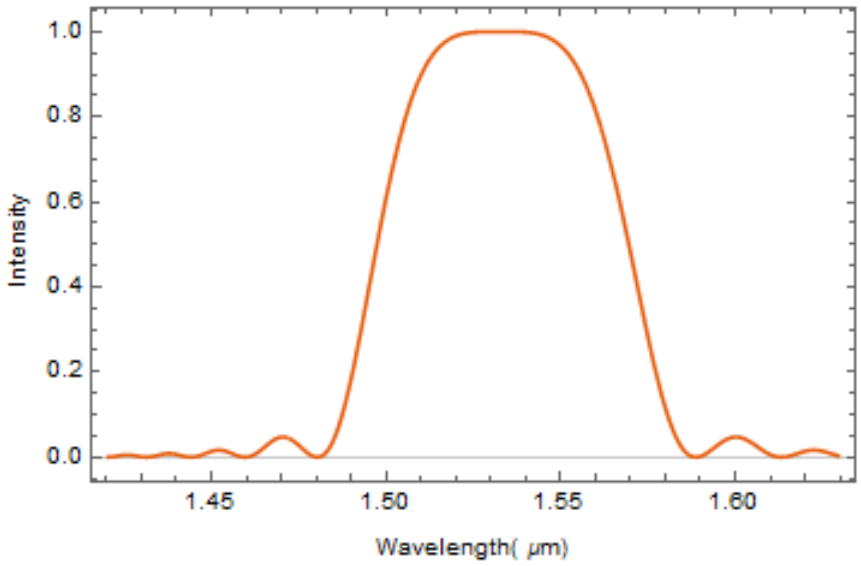

Figure 4.5: SPDC bandwidth .The bandwidth of the down-conversion set by the phase mismatching function $|\phi(\omega_s, \omega_i)|^2$

dispersion and crystal length change. The JSI will also change accordingly, as shown in Fig. 4.8.

The cavity parameters are shown in tab. 4.1.

Table 4.1: Cavity Parameter.

FSR	13.1GHz
FINESSE	7.524
LINEWIDTH	1.754GHz

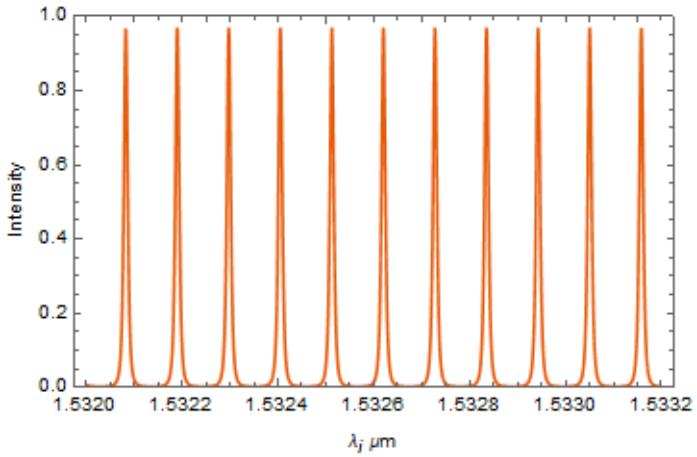

(a)

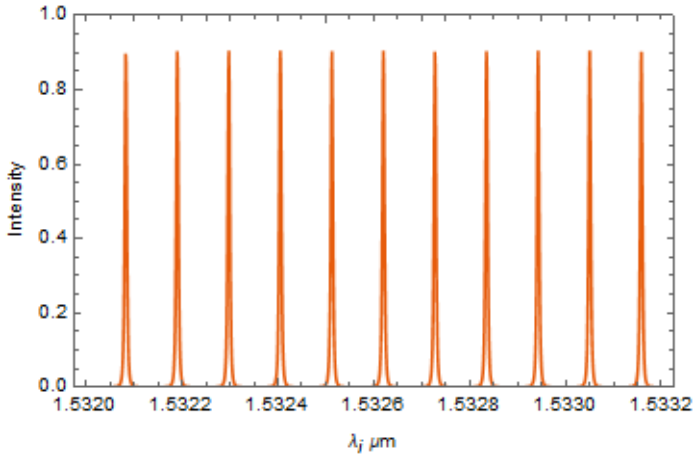

(b)

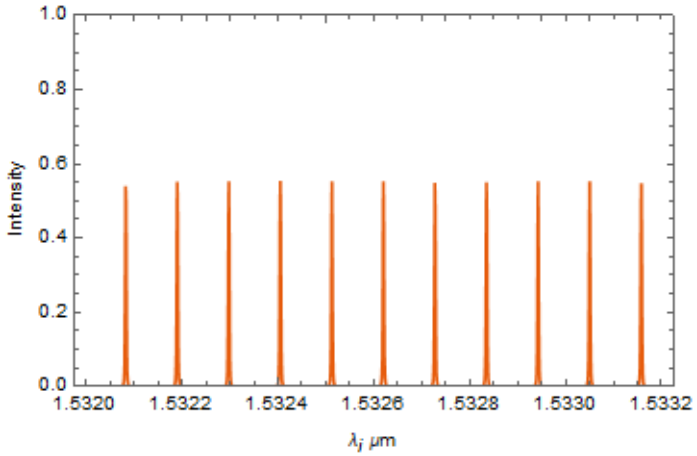

(c)

Figure 4.6: JSI with cavity. This plot illustrates the JSI with different cavity mirror reflectivity value in a set temperature ($T = 61.7°$C). (a) The two end facet mirror reflectivity R1=99.5%, R2=45%. (b) R1=99.5%, R2=65%. (c) R1=99.5%, R2=85%

.

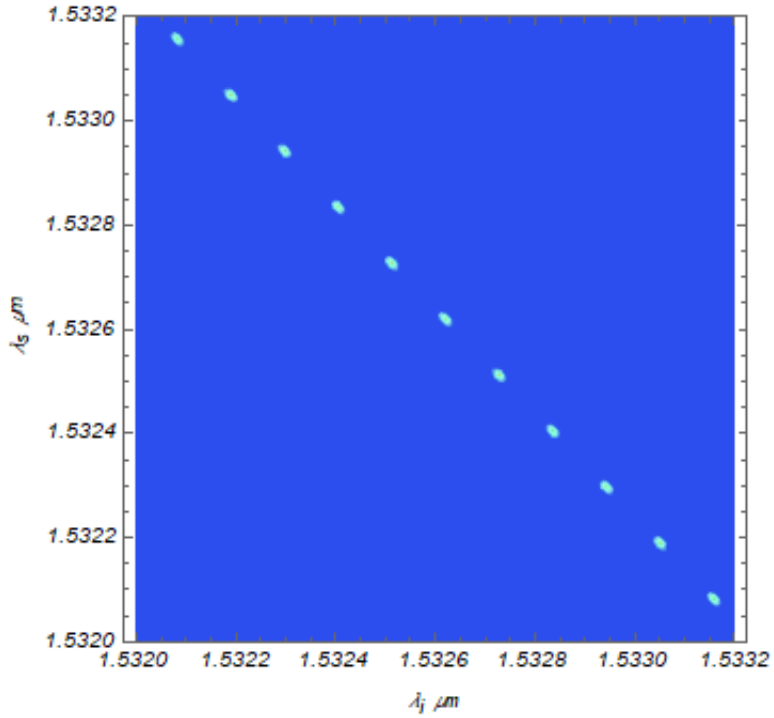

(a)

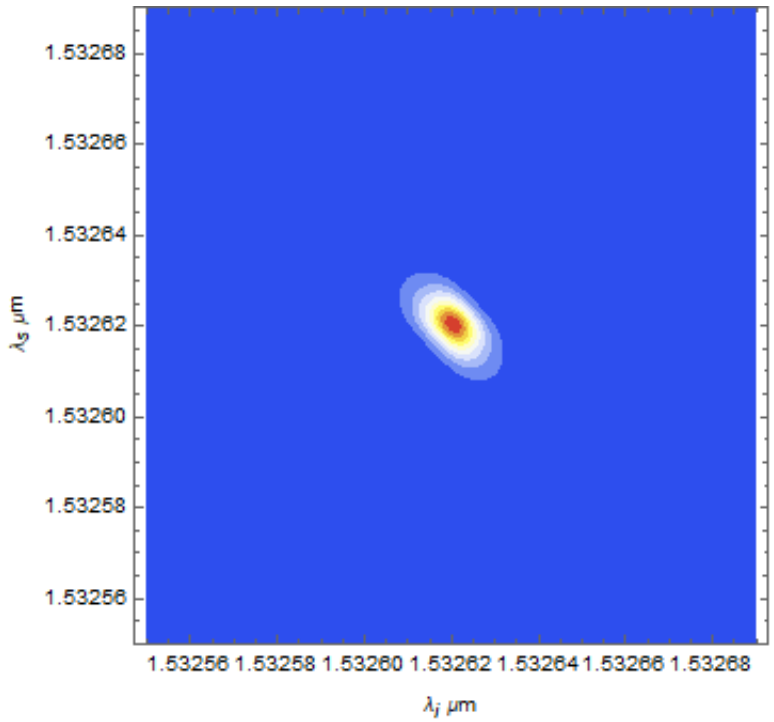

(b)

Figure 4.7: JSI Contour. JSI Contour in a set temperature ($T = 61.7°$C with two end facet mirror reflectivity values R1=99.5%, R2=45% .(a) 11 modes Contour from 1532 nm to 1533.2 nm (b) Contour of single mode shape

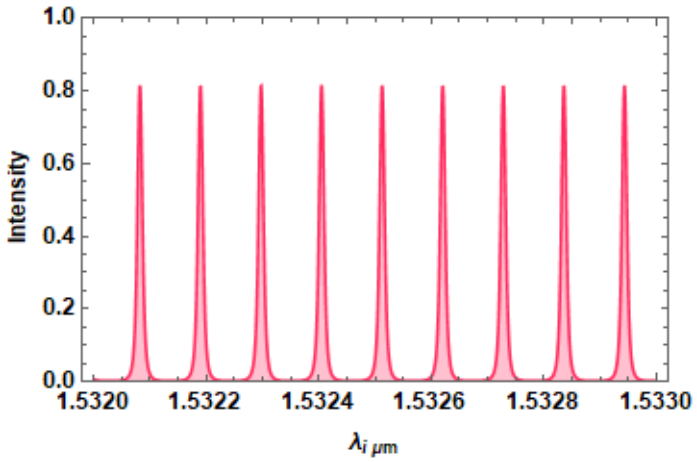

(a)

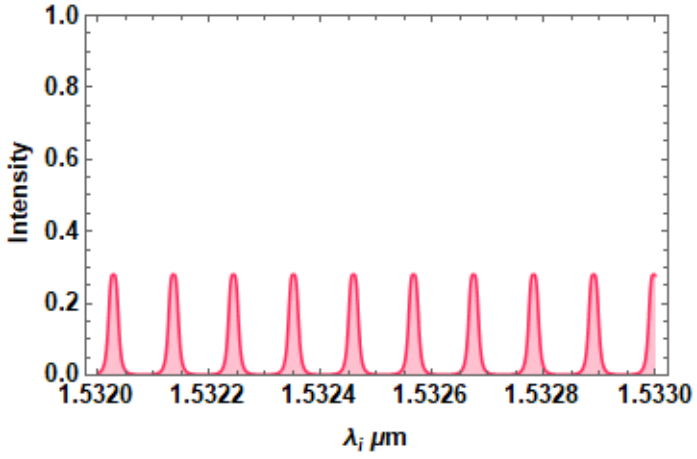

(b)

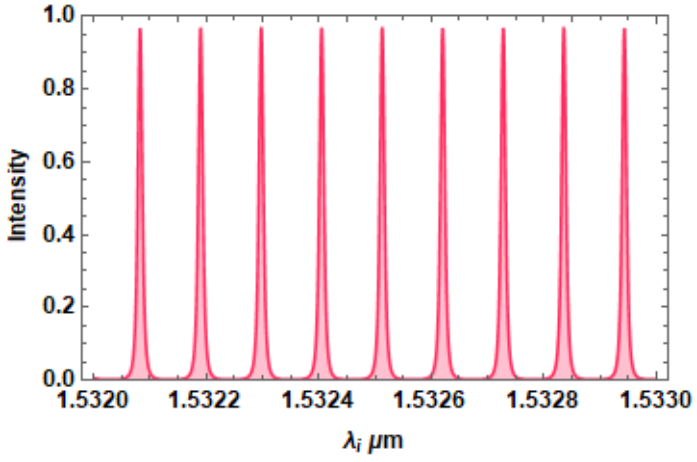

(c)

Figure 4.8: JSI in varied temperature. In a set coating mirror (R1=99.5%, R2=45%) , temperature tuning gives different JSI. (a) $T = 31.3°C$. (b) $T = 56.4°C$. (c) $T = 61.7°C$

.

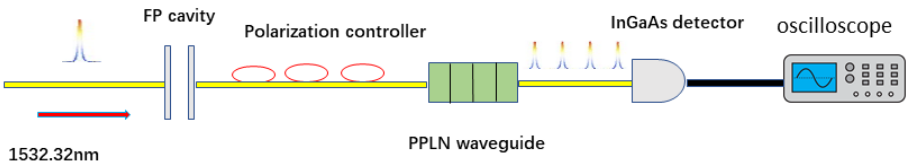

Figure 4.9: Cavity Characterization setup. A 1532 nm single frequency laser controlled by a manually polarization controller passes through the waveguide chip. The cavity transmission is recorded by an InGaAs detector and oscilloscope.

Combined with Eq.3.12 in the last chapter and Eq.4.13, 4.14, one can recalculate the pair generation rate of this wave-guide to be $\sim 8.89 \times 10^6$ pairs/s/mW per mode which equates to $\sim 6.35 \times 10^8$ pairs/s/nm/mw.

To characterize this cavity, we employed a CW tunable single-frequency laser operating at around 1532.32 nm laser and a reference Fabry-Perot cavity whose FSR is given as 1.5 GHz. The cavity was investigated by measuring the transmission out by scanning the 1532 nm laser with the FP cavity, and the setup is shown in Fig. 4.9. The transmission output is shown in Fig. 4.10. However, due to the limitation of the laser scan function, it couldn't give enough scan offset to show the FSR of the cavity. By comparing the transmission output with the referenced cavity with 1.5 GHz FSR and reference FP cavity calibration, using MATLAB to find the halfwidth value, we can roughly find the linewidth of the cavity to be nearly 3 GHz. This value is not precise due to the limit of the scanning system. More accurate line-width could be measured with a high-resolution spectral analyzer. The crystal length and coating could also cause the linewidth discrepancy between the actual and theoretical values. The actual specification might not be the same as the specification provided by the supplier, and the waveguide propagation losses are larger than the specification value we use in the theoretical calculation. As a result of the maximal scan range of the laser is only 8 GHz, which is much smaller than a full FSR, we could not obtain the FSR value from this measurement.

The frequency spectrum of the cavity can be tuned by changing its temperature. The length of

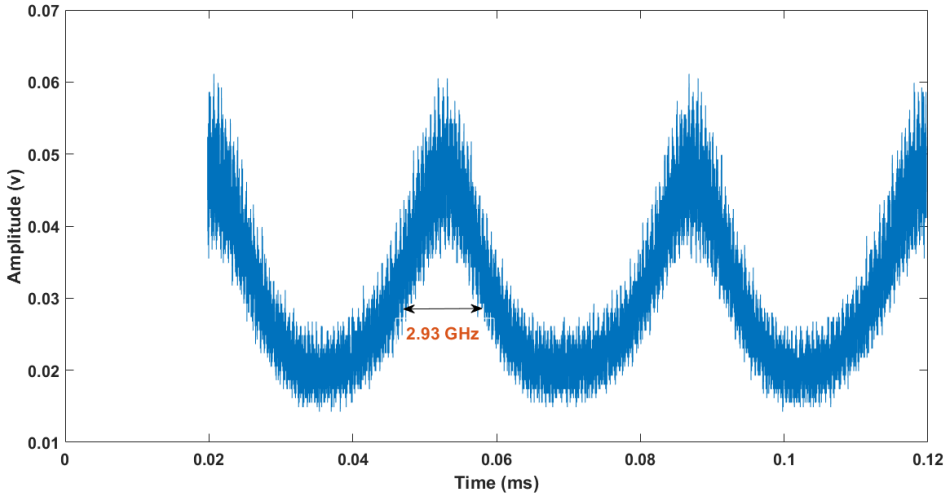

(a)

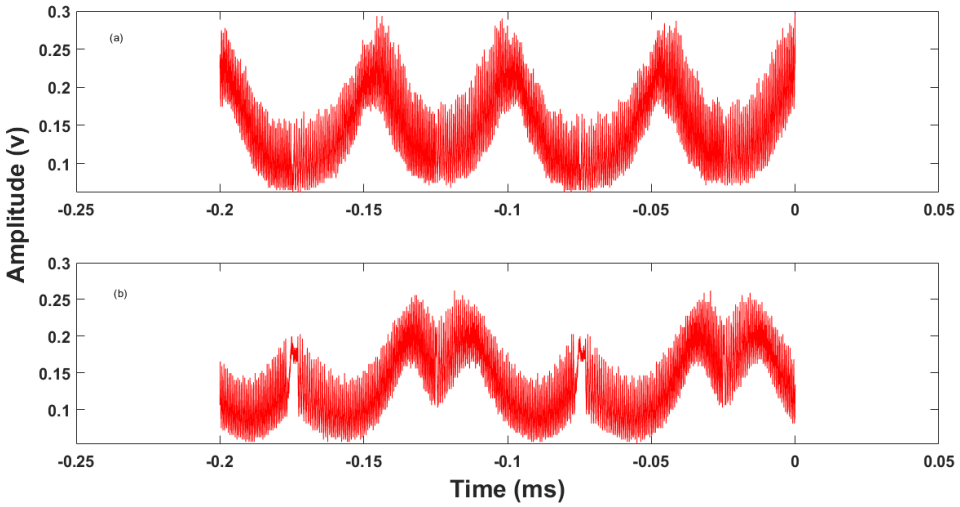

(b)

Figure 4.10: Cavity feature. This PDC source cavity transmission measured with an oscilloscope. (a) 1532 nm cavity transmission. (b) Cavity transmission at 85°C (a) and 103°C (b)

.

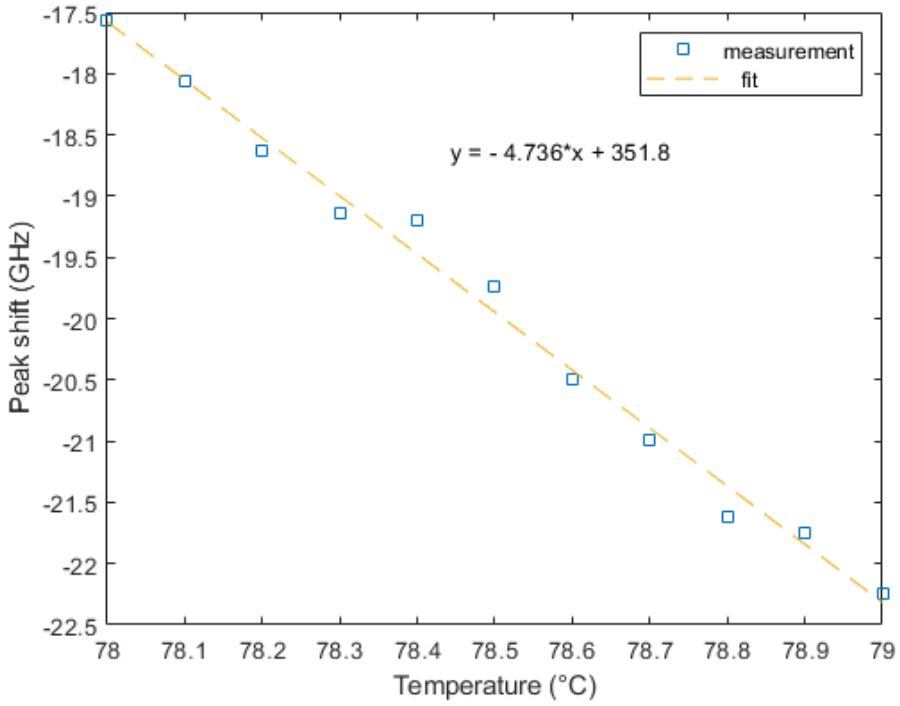

Figure 4.11: Cavity peak shift 4.736 GHz per degree

the cavity and the effective index of refraction change as a result of thermal expansion leading the spectrum shift, as shown in Fig. 4.10 (b). To better manipulate this cavity in a later experiment, the cavity peak mode shift against the temperature was measured, and we found the peak shift 4.736 GHz each degree, as shown in Fig. 4.11. By tuning the temperature of the wave-guide the sequence of the cavity modes shifts, and the resonance condition is lost for specific clusters of frequencies, but it is obtained for others [90]. In this measurement, we find about $2^{\circ}C$ degrees have to be changed to shift one cavity mode to another.

Thermal stability better than 0.1°C is guaranteed by a temperature controller consisting of a proportional-integral-derivative (PID) regulation. Different PID settings were compared by measuring the SHG photon counts stability, and one PID settings that gave the most stable counts was chosen, as shown in Fig. 4.12.

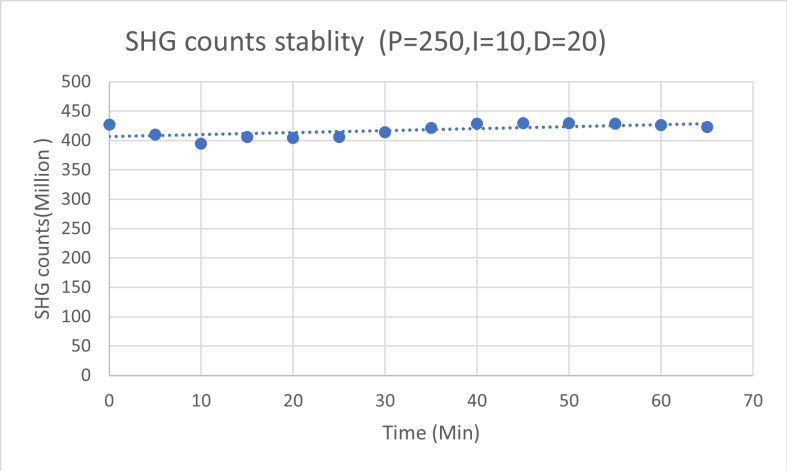

(a)

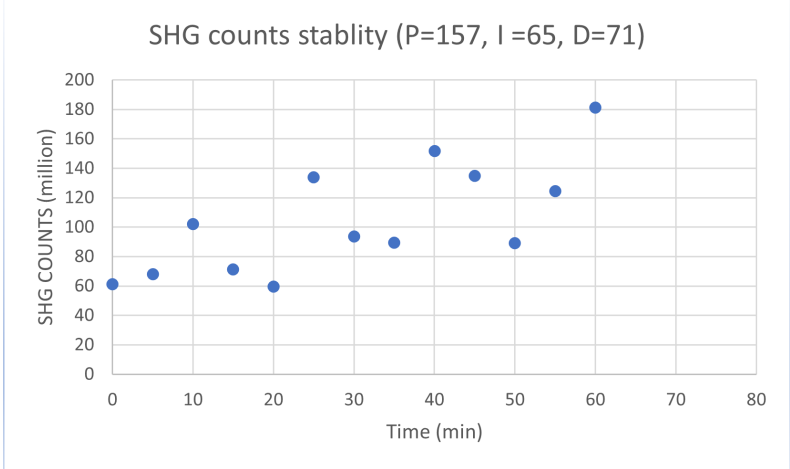

(b)

Figure 4.12: The SHG stability in different PID settings. (a) P=25, I=10, D=20 . (b) P=157, I=65, D=71

.

4.3 SHG Characterization

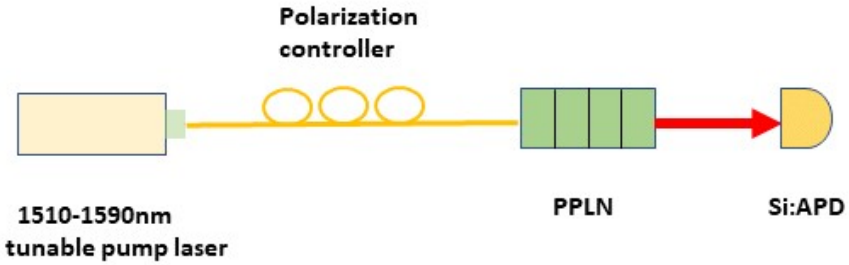

Figure 4.13: SHG characterization setup A tunable fiber laser with a scan range from 1510 nm to 1590 nm passed through the wave guide chip and was detected by a Si:APD

.

In the SHG process, introduced in Sec.3.1, shown in Fig 3.2. Two pump photons are combined into a single-photon of exactly half the wavelength of the pump photons. This single-wavelength energy conservation is in contrast to SPDC, for which the energies conservation determines the possible wavelength of down-converted photon pairs and thus wavelengths of the generated pair photons can be distributed in different ratios between them. On the other hand, the phase-matching condition governing SHG and SPDC processes are exactly the same. Hence, the SHG process is a practical way to probe the phase-matching condition without relying on any precise spectral filtering as the SHG light is at a well-defined wavelength.

For preliminary characterization, the type-0 SHG process in our 5.3 mm PPLN waveguide was measured. The experimental setup for the SHG measurement is shown in Fig. 4.13. A fiber-coupled CW tunable laser at 1510 nm to 1590 nm was sent through a polarization controller at maximum laser power and then coupled into our waveguide PPLN, including 10 waveguide channels. Then, the SHG output was sent to a Si:APD single-photon detector.

With the waveguide temperature fixed at 23.5 °C, we scanned the wavelength of the pump laser and recorded the photon counts against the pump wavelength. The 10 waveguides (SR080315.1 C60-69.2) spectrum peak can be easily identified in Fig. 4.14 (a). The whole spectrum bandwidth

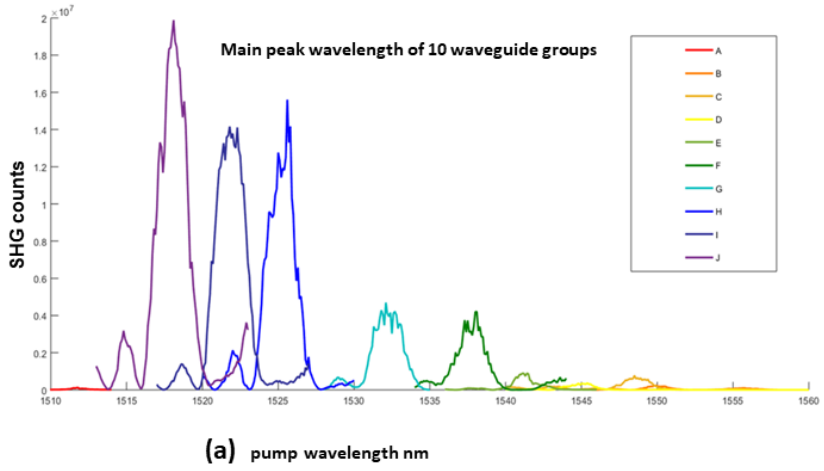

(a) Peak wavelength of 10 waveguid channels

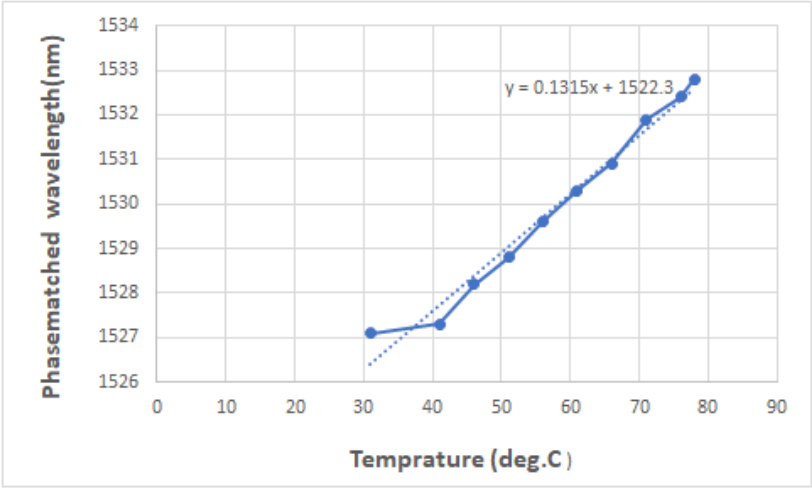

(b) Peak wavelength against temperature in the waveguide H3 and linear fit function

Figure 4.14: Waveguide Phasemacthing: (a) Peak wavelength of 10 waveguide channels. (b) Peak wavelength against temperature in the waveguide H3 and linear fit function. Phase-matched tuning curve for SHG in the PPLN waveguide.

of around 50 nm is comparable with our simulation result, as shown in Fig. 4.5. According to the spectrum peak, a few waveguide channels whose peak wavelength is around 1532 nm match our later Atomic Frequency Comb (AFC) experiment based on Erbium determined. Next, we repeated the SHG spectrum measurement at different temperatures. For each temperature, we found the corresponding fundamental input wavelength at which peak SHG counts occurred. The experimental results are shown in Fig. 4.14 (b), which plots the phase-matched fundamental wavelengths against the temperature. The SHG temperature tuning coefficient is estimated.

$$\frac{\mathrm{d}\lambda_{phm}}{\mathrm{d}T_{pl}} \simeq 0.13 nm/^{\circ}\mathrm{C} \tag{4.16}$$

This phase-matched tuning curve estimates that the degenerate idler and signal at 1532 nm occurred around 80 °C.

In a practical experiment, coupling to a specific waveguide that gives desired peak wavelength is quite challenging. And the temperature tuning provides more flexibility as we can quickly shift the frequency when we switch to a different waveguide channel by tuning the temperature. By using a temperature controller that gives a temperature resolution of 0.1 °C, we could easily obtain the frequency spectrum we want.

The nonlinear coefficient of this PPLN waveguide can be obtained from SHG output power measurement. To measure the power, we adopted a 1532 nm cw single frequency diode laser (TOPTICA) as a pump, and a manual polarization fiber loop controller adjusted its polarization to allow the maximum output power.

We measured the SHG power by tuning waveguide temperature and fundamental pump wavelength, respectively. The setup is shown in Fig. 4.15. The phase-matching measurement by adjusting the temperature gives us a general idea of the maximum power temperature. The result is shown in Fig. 4.16(a). The best phase-matching temperature was found to be 84 °. We then fixed the waveguide temperature at 84 °, tuned the pump wavelength, and recorded the output power from the power meter. Fig. 4.16 (b) shows the SHG power against the pump power. Considering

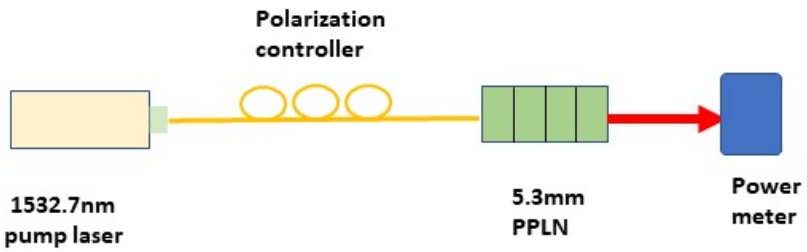

Figure 4.15: **SHG characterization setup**. A 1532.7 nm single frequency laser pass through the PPLN waveguide, and the SHG power was measured by a powermeter

.

the 30% coupling efficiency between the waveguide and fiber and the 45% transmission coating, the input power is around 0.756 mw. With this input, the SHG peak power is 23.6 nw. The waveguide SHG efficiency is given[102].

$$\eta_{SHG} = \frac{P_{\text{in}}}{P_{\text{out}}} = \kappa^2 L^2 P_{\text{in}} \ \text{sinc}^2 \left(\Delta k_{SHG} L/2\right) \tag{4.17}$$

where P_{in} and P_{out} represent the input power and output power. L is the length of the waveguide, and κ is the coupling coefficient for the waveguide SHG, defined as:

$$\kappa = \sqrt{\frac{\left(2\omega_f\right)^2}{2n_s\left(\omega_f\right) n_i\left(\omega_f\right) n_p\left(2\omega_f\right)} \left(\frac{\mu}{\varepsilon_0}\right)^{\frac{3}{2}} \frac{d_{eff}^2}{A_I}} \tag{4.18}$$

Note, d_{eff} is the effective nonlinear coefficient, ω_f is the angular frequency of the pump field, and A_I is the effective mode overlap area. The effective overlap area at our operating wavelength is estimated as $A_I = 78.5\ \mu\text{m}^2$. Assuming phase-matching is satisfied, we have $\Delta k_{SHG} = 0$, so the sinc-squared phase matching function is 1 as the SHG output was measured at the center of the phase matching function. Then, together with Eq.(4.17), we can calculate the relevant nonlinear coefficient $d_{eff} = 2d_{33}/\pi = 14.14$ pm/V where $d_{33} = 22.2$ pm/V. The value we obtained here is comparable with the reported nonlinear coefficient of the ppln waveguide which is 30 pm/V, as

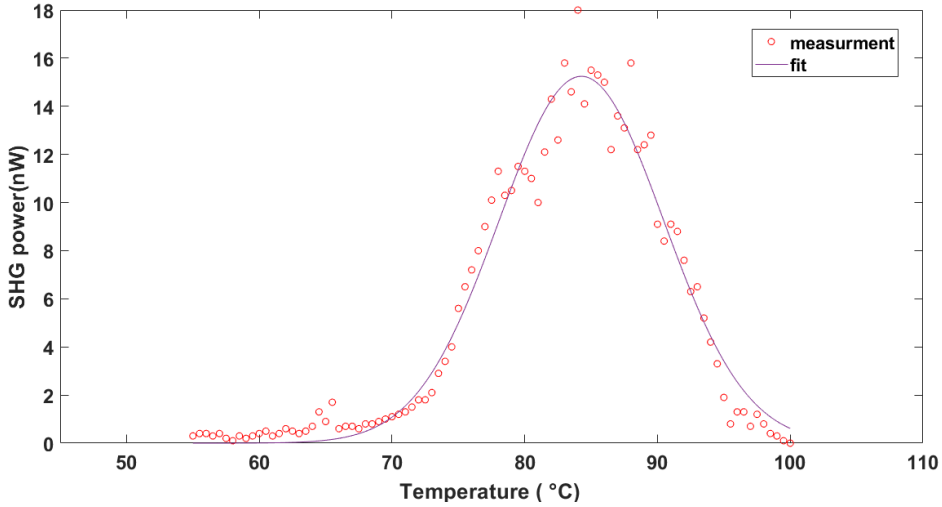

(a) Phasematch against temperature

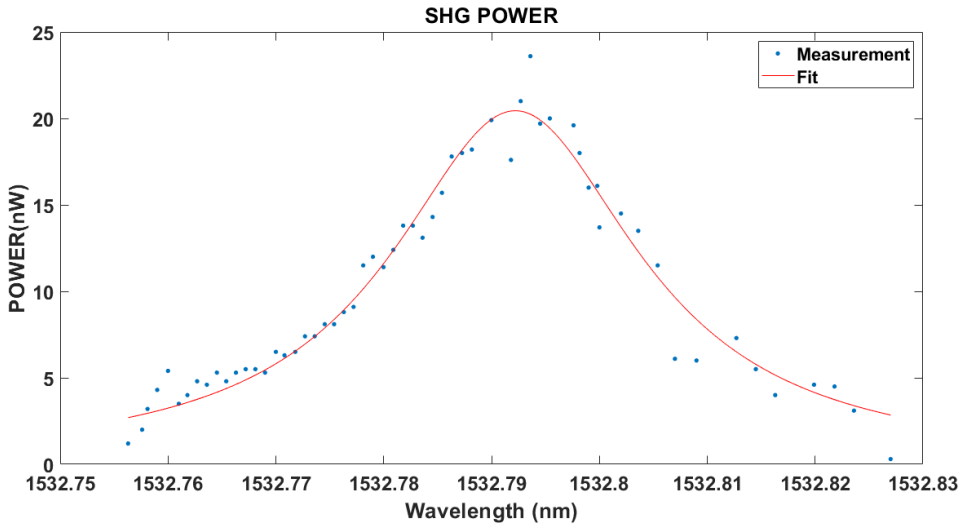

(b) SHG power against pump wavelength

Figure 4.16: Waveguide Phasemacthing. Phase-matching. The best phase-matching temperature was found to be 84 °C. (a) Phasematch against temperature; (b) SHG power against pump wavelength

.

shown in Tab 3.1 in last chapter.

4.4 Photon flux characterization

The experimental setup for characterizing the waveguide SPDC output photon flux is shown in Fig. 4.20. The pump light is a continuous wave single-frequency laser that operates at 766.289 nm polarized, controlled by a manual polarization controller. The fiber to waveguide coupling was optimized by using a pair of V-groove plates preventing vibration-induced instability of the fiber taper. At the end, we achieved reasonable coupling efficiencies of 30%. The fiber waveguide coupling part is shown in Fig. 4.18. The fiber-coupled SPDC output was sent to a fiber isolator to block the residual pump-light (taking advantage of the side-effect of telecom isolators that they are opaque to wavelengths below about 1000 nm). The output light was delivered to two ultra-narrow filters (AOS GmbH) by a beamsplitter. The bandwidth specification of both filters is 40 pm $\pm$ 5 pm (5 GHz) with 2.9 dB insertion loss provided by AOS GmbH. Fig. 4.18 shows the measured transmission, which shows the actual bandwidth of the filter is around 6-8 GHz by comparing the envelop width with a reference F-P caviy with 1.5 GHz FSR.

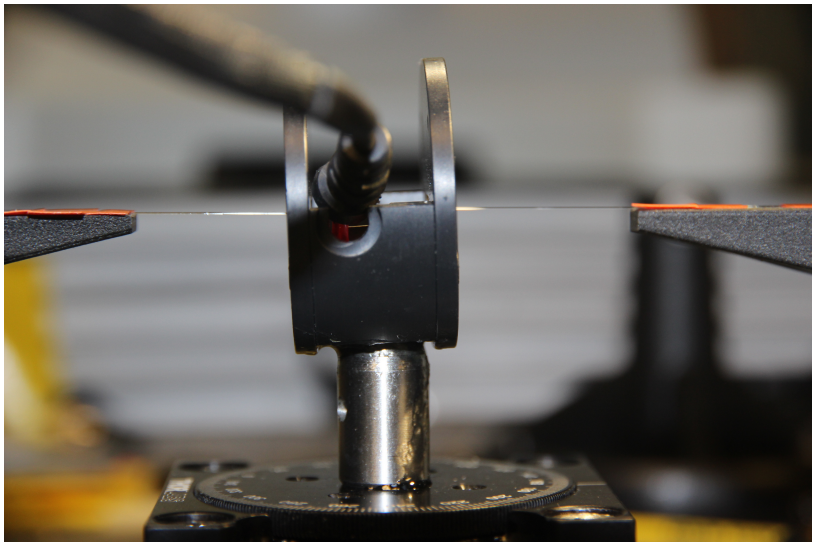

Figure 4.17: Fiber waveguide coupling The ppln waveguide placed in an oven, the input and output coupling fiber are fixed in two V groove mounts

.

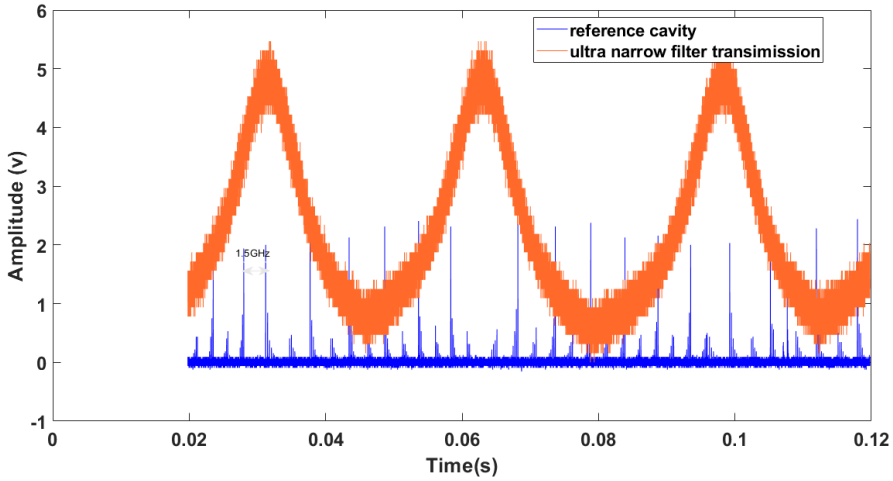

Figure 4.18: Filter transmission. The filter transmission full bandwidth was estimated around $6-8$ GHz by comparing the width with a reference cavity whose FSR gives as 1.5 GHz.

In this way, the signal and the idler photon were distinguished by adjusting the filters to select two wavelengths symmetrically around the SPDC degeneracy wavelength (for example, $\lambda_s = 1532.68$ nm and $\lambda_s = 1532.48$ nm) with a bandwidth of around 6-8 GHz. This ultra-narrow filter could allow us to select one SPDC cavity mode, as the FSR is about 0.1 nm (13.1 GHz). The setup is shown as Fig. 4.19 (b). The measured insertion losses of these two filters are 3 and 3.8 dB, respectively. The signal and idler count were measured by two Superconducting Nanowire Single-Photon Detectors (SNSPD). We also perform some preliminary characterization of the SPDC without filtering, in which case the SPDC outputs are divided by a beam splitter and sent to the SNSPD directly, as shown in Fig. 4.19 (a). The PPLN was set at 83.7 $^{\circ}C$ by the temperature controller.

Before beginning any measurements, we first characterize the overall detection efficiency and noise. For the latter, the dark counts of the two SNSPDs are 50 Hz and 100 Hz. Using 1532 nm light, we assess the losses in various components from the SPDC to the SNSPSDs. The transmission coefficients of all optical components in both signal and idler channels are listed in Table 4.2. Considering the waveguide-to-fiber coupling and transmission of optical components, we estimated the overall signal and idler detection efficiencies at $\eta_s \simeq 4.78\%$ and $\eta_i \simeq 5.58\%$.

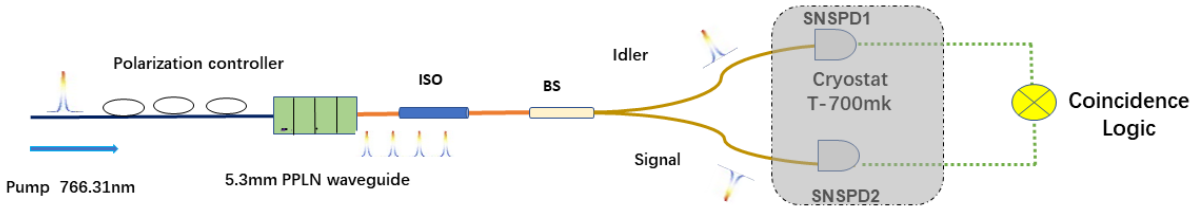

(a)

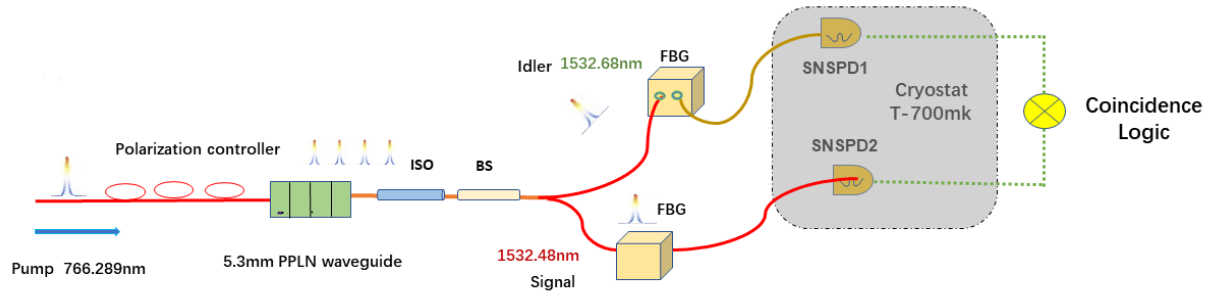

(b)

Figure 4.19: Experiment setup for characterizing the SPDC output flux. (a) The coincidence measurement setup without filter; (b) The coincidence measurment setup with filter

.

System component transmissions		
	Signal channel	Idler channel
Waveguide to fiber coupling	30%	30%
Isolator	86%	86%
Beam splitter	46.5%	46.5%
Fiber to fiber coupling	60%	70%
Fiber connectors	95%	95%
Detector efficiency	70%	70%
Overall detection efficiency	4.78%	5.58%

Table 4.2: Optical component transmissions and the overall detection efficiencies.

In order to evaluate the photon pair source, we performed time-correlated measurements on the signals from the two SNSPDs. The specific method is to measure second-order cross-correlation function $G^{(2)}_{s,i}(\tau)$ [103, 104] between the photon pairs.

The coincidence between signal and idler photons was measured with a Qutools time-to-digital converter with a maximal resolution, given in terms of bin size, of 81 ps. The coincidence analysis software running the time-to-digital converter can set different coincidence windows and electrical delay times. A successful coincidence count was recorded by a PC-installed electronic counter (NI) when two detection events from the two SNSPDs were separated by less than the coincidence window. The coincidence window was set to 10 bins in our experiment. The result of $G^{(2)}_{s,i}(\tau)$ with 0.45 mw and 0.21 μW pump without filter (setup in Fig. 4.19) is shown in Fig. 4.20 a and b, respectively.

In terms of quantum information processing requirement, the normalized cross-correlation function of the photon source needs to be a larger value at zero delay $g^{(2)}_{s,i}(0)$. The normalized cross-correlation function can be written as

$$g^{(2)}_{s,i}(\tau) = \frac{\left\langle E^{\dagger}_{s}(t)E^{\dagger}_{i}(t+\tau)E_{i}(t+\tau)E_{s}(t)\right\rangle}{\left\langle E^{\dagger}_{i}(t+\tau)E_{i}(t+\tau)\right\rangle\left\langle E^{\dagger}_{s}(t)E_{s}(t)\right\rangle} \tag{4.19}$$

$E_{s,i}(\tau)$ above is the operator of signal light field and idle light field. In the practical experiment, the cross-correlation function value can be obtained by dividing the peak value of the correlation function by the average accidental count of the random coincidence area.

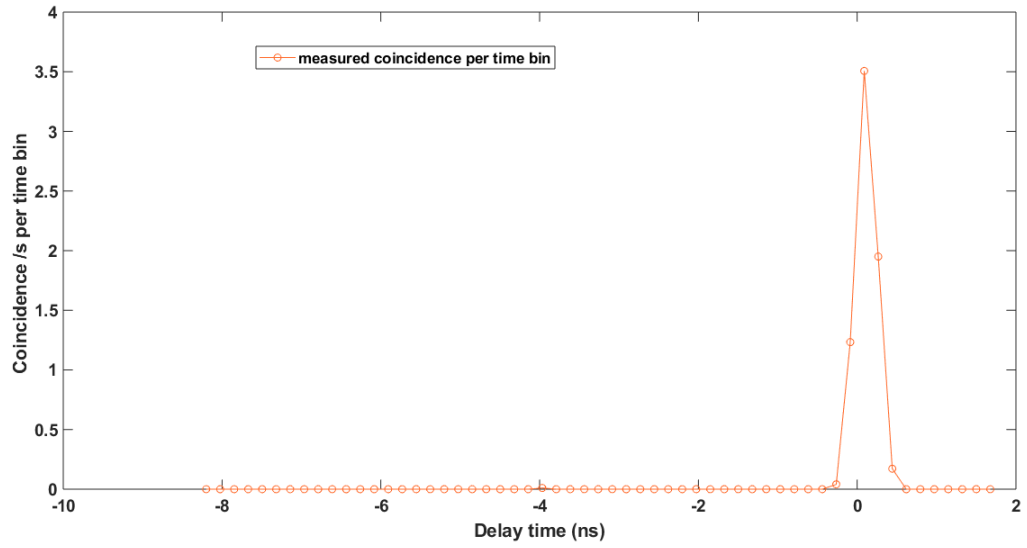

(a)

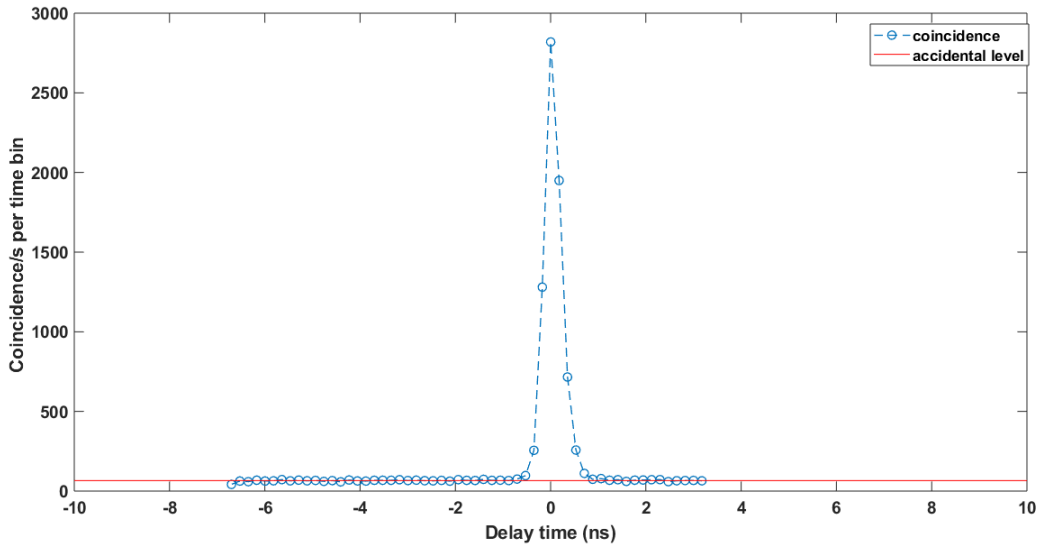

(b)

Figure 4.20: $G^{(2)}_{s,i}(\tau)$ measurement (a) (b): the incident pump power is 0.21 μW and 0.45 mW respectively, the time Bin is 81 ps, the coincidence window is 10 bin

.

The insert graph in Fig. 4.21 (b) shows the varied value of $g^{(2)}_{s,i}(0)$ with different pump power, which is an inversely proportional relationship with the power change [105]. The value of $g^{(2)}_{s,i}(0)$ is 1900 with 1.3 μW, which is far exceeding the classical threshold of 2 for the two-mode squeezed state. The $g^{(2)}_{s,i}(0)$ drops to 54 when pump power increase to 100 μW. The background noise in the data was subtracted. A very high $g^{(2)}_{s,i}(0)$ value indicates a high-quality quantum light source that can use in quantum networks.

The relationship between the coincidence, single rate, and the incident pump light power P_p is shown in Fig. 4.22 (a). According to the assumption of the correlation between the signal and idler and the theory of waveguide, a linear increase of R_s (signal single rate), R_i (idler single rate) and R_c (coincidence rate) with the input pump power P_p was expected. As shown in Fig. 4.21 (a), the measured singles rate has a linear dependence on the pump power. In this measurement, the detectors saturated when the pump power was higher than 0.12 mW. The generation efficiency can be calculated according to [101].

$$R_{gen} = R_c/\eta_s\eta_i P_p \tag{4.20}$$

And we obtain a pair generation rate of $\sim 3.289 \times 10^7$ pairs/s/mW of pump based on the data as shown in Fig. 4.21 and Tab. 4.3. The result is much smaller compared with our theoretical estimate.

The singles rates can be obtained from the net coincidence rate according to [101]

$$\tilde{R}_{s,i} = R_c/\eta_{i,s} \tag{4.21}$$

We find $\tilde{R}_{s,i}$ is smaller than the measured rates because the measured singles included background photons that were primarily fluorescence photons. For 0.21 μW effective pump, 610 single counts was registered with 17.5 coincidence in the 10 bins coincidence window. From Eq. 4.21, we can calculate the down-converted singles rates to be 379, which is smaller than our measured results. We suggested the cause to be the residual pump and other fluorescence noise.

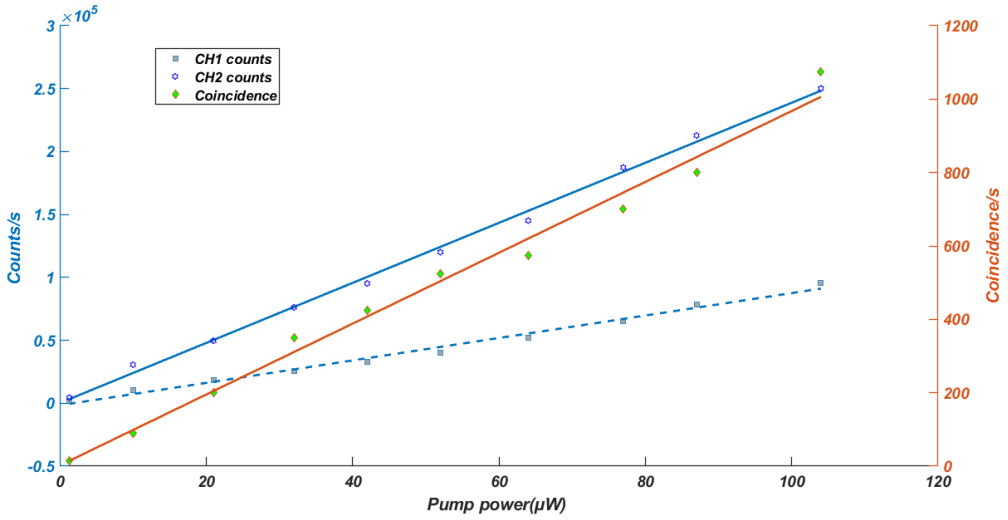

(a)

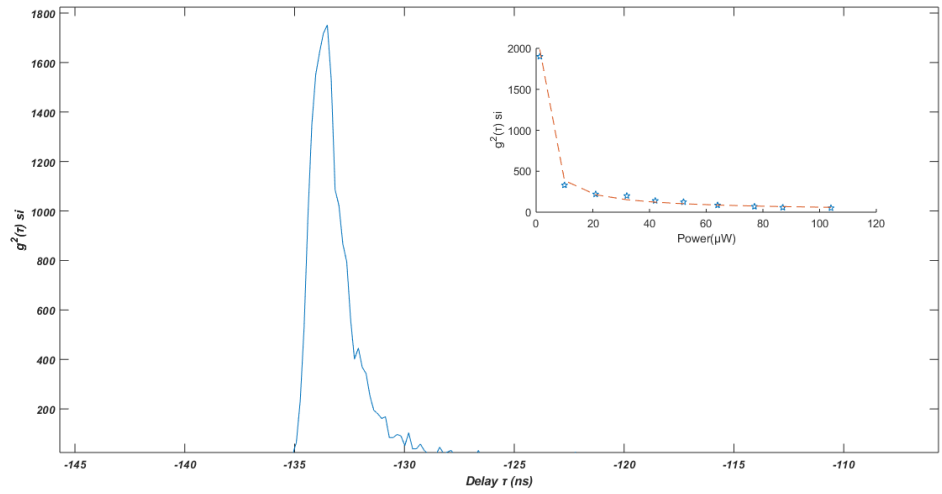

(b)

Figure 4.21: Counts and $g^{(2)}_{s,i}(\tau)$ depend on input pump power. (a): Measured singles counts (dark counts subtracted) for signal, idler, and coincidence counts (accidentals subtracted) versus pump powers. (b) $g^{(2)}_{s,i}(\tau)$ at 1.3 μW pump, the insert graph is the $g^{(2)}_{s,i}(0)$ versus pump power.

Table 4.3: Coincidence measurement result

Coincidence Measurement result		
	without filter	with filter
Effective input power	0.21 uW	0.7 mW
Coincidence/s/10 bin	17.5	20.5

In this thesis, the spectral brightness of a photon source is defined as the number of photon pairs measured each second per optical bandwidth (in GHz) of one particular frequency mode and per mW of pump power [101].

$$[B] = \frac{\text{photon pairs /s}}{\text{mW} * \text{GHz}} \tag{4.22}$$

Due to the interference between different frequency modes, the time-resolved $g^{(2)}_{s,i}(\tau)$ measurement result of the cavity-enhanced spontaneous parameter down-conversion photon should be a comb structure in the time domain [106]. The interference fringe period is $t = 1/FSR$, which is the same as the cycle time of the optical cavity. Yet, the resolution time of the single-photon detector is around 200 ps, but the cycle time of the optical cavity is 76 ps. That could explain the disappearance of the comb structure in our measurement result.

In order to guarantee a single-mode measurement with the detectors having a timing resolution of hundreds of picoseconds,the following needs to happen: $\Delta v \ll 1$GHz [109]. However, the linewidth of this source is larger than 1 GHz, which makes a single-mode measurement impossible with our current 200 *ps* resolution detectors.

4.5 Spectrum characterization with filter

To better characterize the spectrum of the down-converted photon, we used two ultra narrow-band filters (AOS) with a spectral FWHM bandwidth of around 8 GHz. 3 dB and 3.8 dB insertion loss were measured, and the center wavelength can manually be tuned with a spectral resolution of 0.004 nm. The experimental setup keeps the same as that is shown in Fig. 4.19 b.

We first calibrated the filter uses a wavemeter; the relationship between the spectral and position

are shown in Fig. 4.22 (a), (b). After being filtered, the photons are detected by two superconducting nanowire single-photon detectors with 70% quantum efficiency, at which it has 165 dark counts per second in the signal photon detector channel. Note, it was suggested that our detector upgrades cause the increase of dark counts in this measurement.

The single-photon count is detected in both signal and idler channels by scanning the filter center wavelength from 1532.57 nm to 1532.8 nm. The spectral result for signal photons is shown in Fig. 4.23 (a), in which the dark count of the detector was not subtracted. In this measurement, the pump laser operated at 766.2885 nm. Note that the figure shown is not the true signal photon spectrum as a result of the limit of bandwidth of the narrowband filter. The measured data needs deconvolution to remove the effect of the filter transmission bandwidth. However, a deconvolution technique is not suitable in this case since the bandwidth of the filter is much wider compared with that of this SPDC cavity. In order to estimate the bandwidth of this waveguide resonator, we could use the exponential decay to fit the cross -correlation function if the detector resolution is as high as a few picoseconds, which is also not suited in our device with our current detectors. So we can only roughly estimate the linewidth of this integrated resonator from the oscilloscope measurement described in the previous subsections.

From the result of this measurement, three peak resonant modes 1532.57 nm, 1532.67 *nm* and 1532.77 *nm* were witnessed and separated with about 13.1 GHz (0.1 nm), which is exactly one FSR of the cavity. See in Fig. 4.23 (a). This result agrees well with our simulation result shown in Fig. 4.23 (b). Nevertheless, almost half of the count was detected in the un-resonant modes. The contrast ratio is around 2 : 1; in principle, using this filter should allow the single-mode output of the source, but due to relatively low finesse for the filter, it could still catch the edges of the adjacent modes that might mix in the final output. A narrower filter could be used to address this problem.

We then used the two FBG filters to select three resonant pairs and two unresonant pairs. The effective pump power in this measurement is 0.52 mw. The coincidence measurement result of

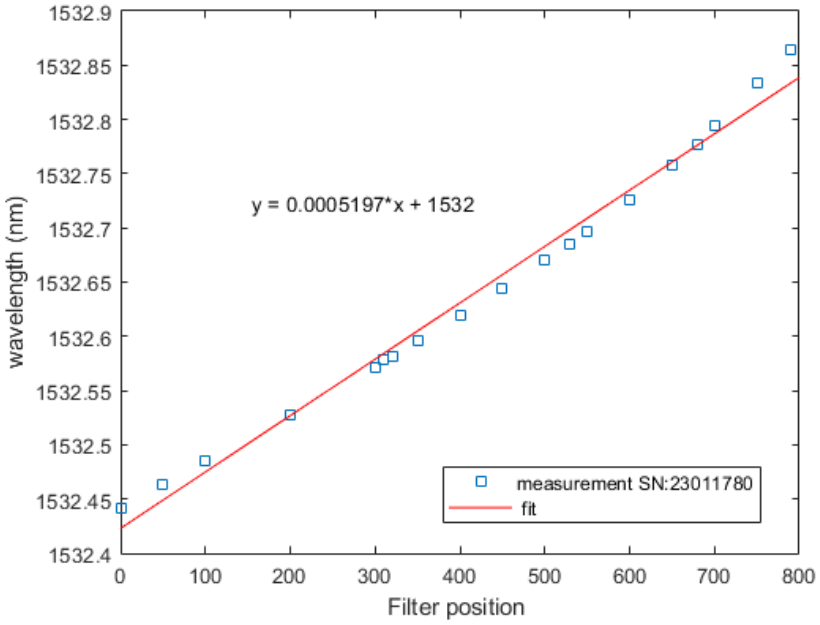

(a)

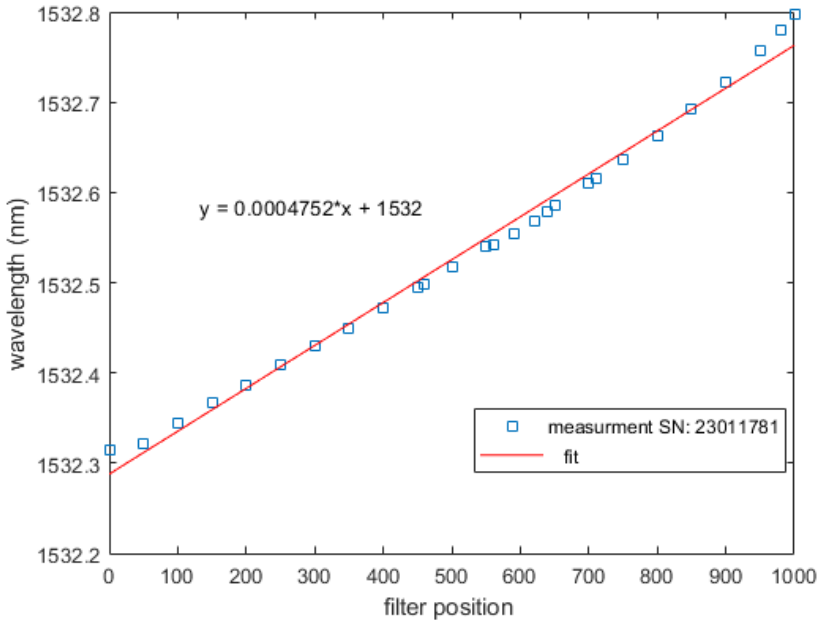

(b)

Figure 4.22: filter calibration. The two filter calibrated with a wave-meter. (a) Calibration of the filter with series number of SN:23011780. (b) Calibration of the filter with series number of SN:23011781.

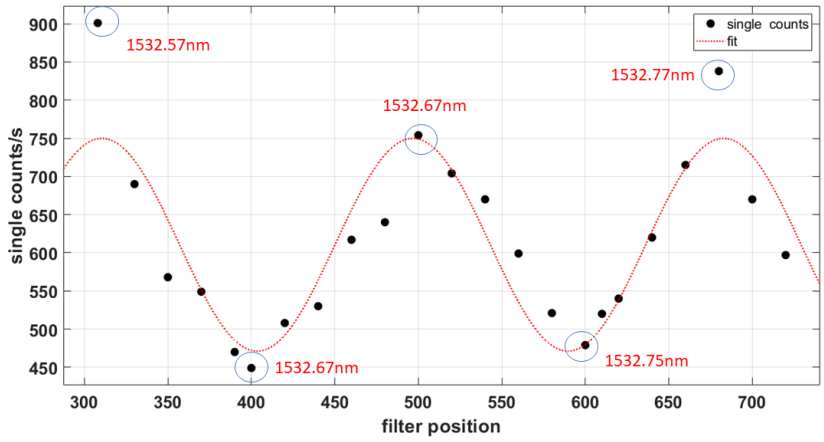

(a) Signal single counts variation by scanning the filter

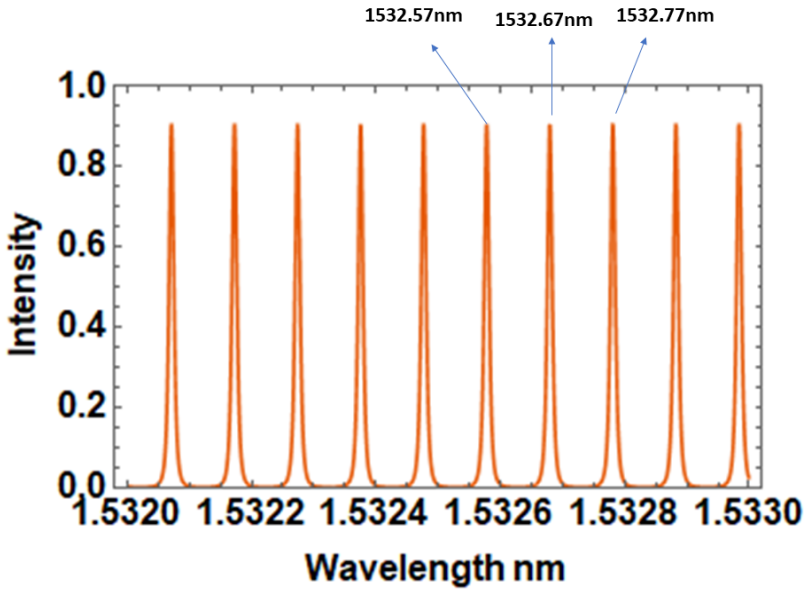

(b) Simulation result

Figure 4.23: Spectral intensity change by scanning the filter (SN:23011780) . (a) Signal single counts variation by scanning the filter. (b) Simulation result. The resonant spectral intensity is almost twice of the non-resonant spectral intensity.

each pair is shown in Fig. 4.24. The coincidence rate of the unresonant pairs is $1/3$ of the resonant pair. But as a result of the limit of the filter range, we could not select more than three modes. In the future, we consider using a microring resonator filter that has multiple output ports. Thus, it could work as the source of high-dimensional quantum information processing.

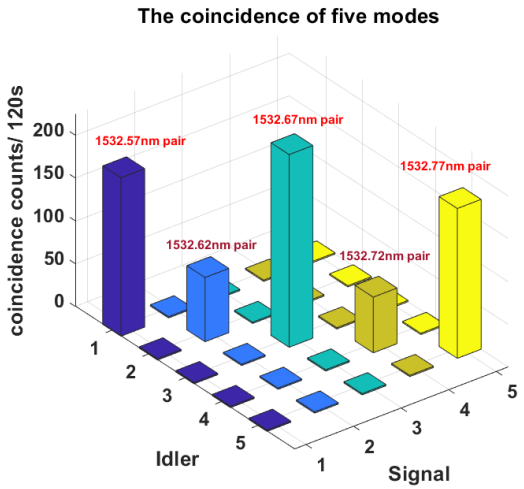

(a) The coincidence for 5 modes

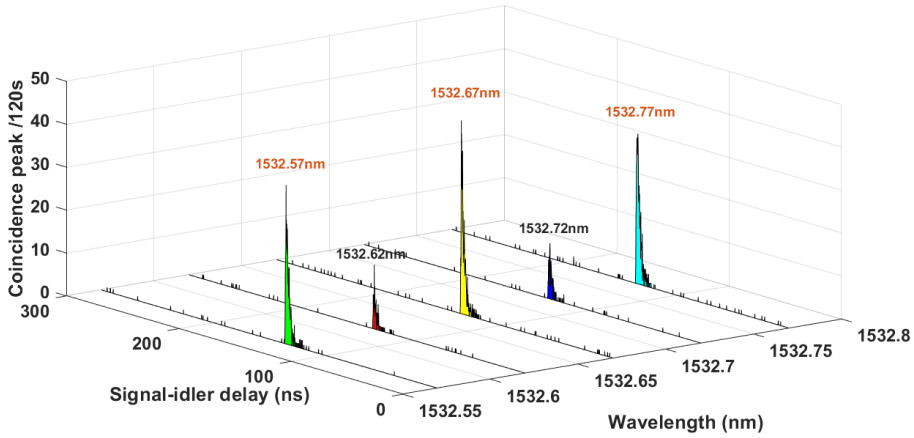

(b) The coincidence peak within 120s

Figure 4.24: The coincidence measurement result. The non-resonant pair coincidence is around $1/3$ of the resonant pair. The coincidence window is 10 bins. The effective pump power is 0.78 mw. (a) The total coincidence with 120s integral time. (b) The coincidence peak with 120s integral time.

We then injected 0.7 mw effective pump power into the waveguide resonator with 766.288 nm light. We observed 2246 single counts s^{-1} for the central mode (1532.57 nm) on the signal channel

detector and 4.1 coincidences per second per bin, and the coincidences window is 10 bin. The total coincidence was obtained by summing up all the coincidences in the coincidence window. The measured cross-correlation between signal and idler with a TDC is shown in Fig. 4.25 (a). The temperature of the waveguide was fixed at $T = 83.6\ ^\circ$ C. The high $g^{(2)}_{s,i}(\tau)$ shown in Fig. 4.25 (b) exhibited great signal-to-noise ratio of this source after filtering.

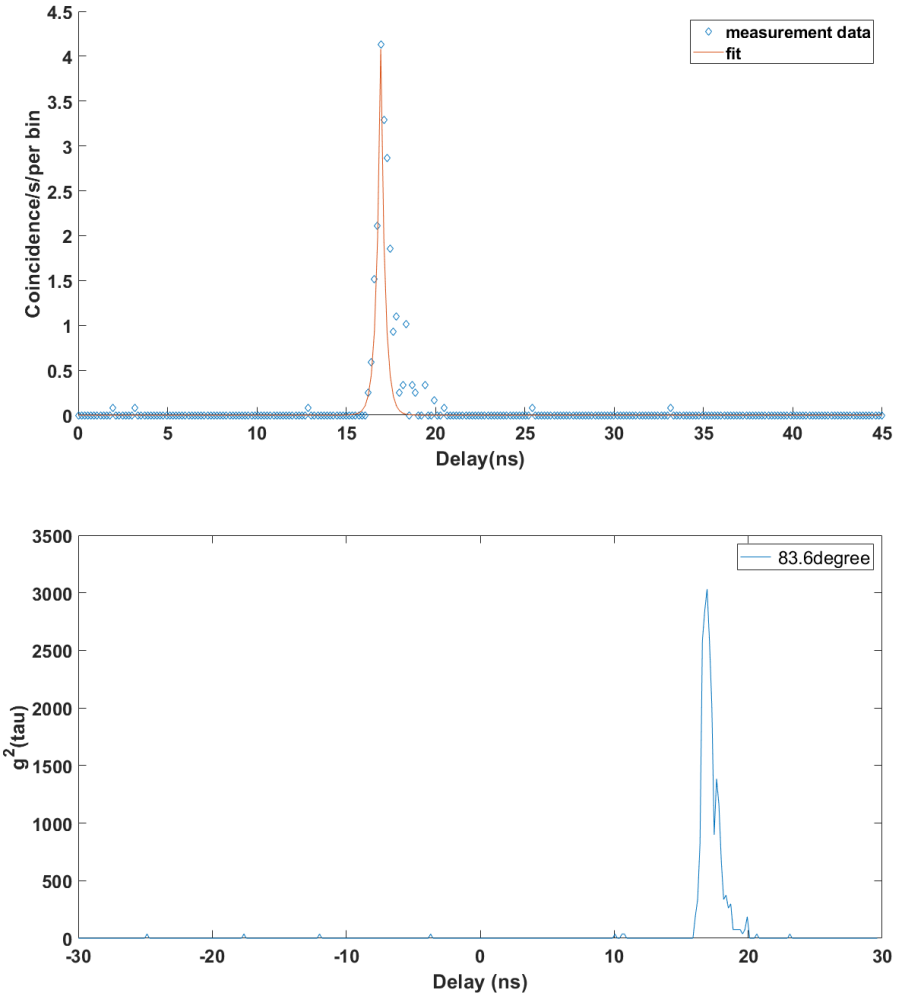

Figure 4.25: Coincidences as a function of the temporal delay between the signal and idler detection. (a) Coincidence per second per bin with 0.7 mw effective pump power. (b) The $g^{(2)}_{s,i}(\tau)$ with 1.11 mw effective pump power

.

We then calculated the spectral brightness of the source, taking into account the overall loss of the system mentioned in the last section, which corresponds to $\sim 1.47 \times 10^4/\mathrm{s/GHz/mW}$ pairs of

photons emitted per second, per GHz of bandwidth and per mW of effective pump power.

In order to evaluate the brightness of our pair source, we compared it with the measured brightness reported in [107] for a 3 cm type 0 PPLN waveguide pumped by a CW laser at 777 nm and generating photons in a degenerate configuration at 1554 nm. The brightness of such a source is 2×10^5 photon pairs generated per second, per GHz of bandwidth and per mW of pump power. Considering the length of our waveguide is much shorter than [107], we estimated the brightness of this waveguide source without cavity to be 6.4×10^3 photon pairs were generated per second. According to [102] double-resonant OPOs undergo an average enhancement factor per resonant mode equal to the square of the finesse F over π that gives 17. Therefore, the optimized, integrated cavity-waveguide reported in this subsection would have a brightness of $1.08 \times 10^5 (\text{ s mW})^{-1}$ in a single resonant mode. However, the experimental enhancement factor is 2.3 showing there is still much space to improve. The result can be further improved by enhancing the fiber to waveguide coupling efficiency and detector upgrade in the future. Note, because of our experiment condition is not exactly the same with [107], such as crystal loss and pump condition could be different, so we can only obtain a roughly value of the experimental enhancement factor.

Chapter 5

Conclusion

In this work, we have experimentally demonstrated the production of spectrally multimode photon pairs at 1532 nm base on a type-0 phase-matched PPLN waveguide, yielding a source brightness of 3.28952×10^7 pairs/s/mW of pump over the entire phase-matching bandwidth and 2.58×10^4 pairs/s/mW per cavity mode. The brightness can be further enhanced by improving the fiber waveguide coupling and detector optimization. The current implementation can be stabilized better by using a higher-resolution temperature controller.

In this thesis, 3 spectral modes were witnessed with the ultra- narrow filter. In order to maximize the probability of delivering a single photon, addressing many frequency modes is necessary. A high Q factor microring resonator filter with multiple output ports can be considered in future work. One limitation in our current set-up is that the filter bandwidth is not narrow enough to perfectly select one spectral mode, and the detector resolution is too big to distinguish different modes.

This integrated spectrally multimode photon source is very simple and compact, and it is a promising candidate for a frequency multiplexed quantum repeater that can be efficiently combined with an AFC quantum memory. Furthermore, the availability of the frequency and time-bin entanglement of this source could also be utilized in high- dimensional quantum information processing.

Bibliography

[1] L. Rosenfeld, La premiere phase de le‘volution de la The‘orie de Quanta, Osiris 2, 149196 (1936). 2

[2] L. Rosenfeld, Max Planck et la de‘finition statistique de lentropie in Max Planck Festschrift, edited by B. Kockel, W. Macke, and A. Papapetrou (Veb Deutscher Verlag Der Wissenschaften, Berlin, 1958), pp.203211

[3] Nicolas Gisin and Rob Thew, Quantum Communication Technology. Electronics Letters 46(14):965 - 967/ (2010)

[4] P. W. Shor, Algorithms for quantum computation: discrete logarithms and factoring, Proceedings 35th Annual Symposium on Foundations of Computer Science, 1994, pp. 124-134, doi: 10.1109/SFCS.1994.365700.

[5] Lov K. Grover .Quantum Mechanics Helps in Searching for a Needle in a Haystack. Phys. Rev. Lett. 79, 325 14 July 1997

[6] Gisin, N., Thew, R. Quantum communication. Nature Photon 1, 165171 (2007).

[7] Wootters, W., Zurek, W. A single quantum cannot be cloned. Nature 299, 802803 (1982). https://doi.org/10.1038/299802a0

[8] Peter W. Shor and John Preskill. Simple Proof of Security of the BB84 Quantum Key Distribution Protocol. Phys. Rev. Lett. 85, 441. 10 July 2000

[9] J. I. Cirac and P. Zoller. Quantum Computations with Cold Trapped Ions. Phys. Rev. Lett. 74, 4091. 15 May 1995

[10] Vittorio Giovannetti, Seth Lloyd, and Lorenzo Maccone. Quantum Metrology. Phys. Rev. Lett. 96, 010401. 3 January 2006.

[11] Chen, YA., Zhang, Q., Chen, TY. et al. An integrated space-to-ground quantum communication network over 4,600 kilometres. Nature 589, 214219 (2021).

[12] Heralded Single Photons Based on Spectral Multiplexing and Feed-Forward Control, M. Grimau Puigibert, G. H. Aguilar, Q. Zhou, F. Marsili, M. D. Shaw, V. B. Verma, S. W. Nam, D. Oblak, and W. Tittel, Phys. Rev. Lett. 119, 083601, Published 25 August 2017.

[13] Towards a Real-World Quantum Repeater Marcel.li Grimau Puigibert a thesis of Doctor of Philosophy university of Calgary.

[14] Zheng L, Wang S, Tian L, et al., Query-adaptive late fusion for image search and person re-identification, Proceedings of the IEEE Conference on Computer Vision and Pattern Recognition, 2015: 1741-1750.

[15] H. Hbel, M. R. Vanner, T. Lederer, B. Blauensteiner, T. Lornser, A. Poppe, and A. Zeilinger. High -fidelity transmission of polarization encoded qubits from an entangled source over 100 km of fiber. Opt. Express, 15(12):7853-7862, June 2007.

[16] J. Brendel, N. Gisin, W. Tittel, and H. Zbinden. Pulsed energy-time entangled twin-photon source for quantum communication. Phys. Rev. Lett., 82:2594-2597,March 1999.

[17] D. Dieks. Communication by epr devices. 92(6):271-272, November 1982

[18] N. Gisin, G. Ribordy, W. Tittel, and H. Zbinden. Quantum cryptography. Rev.Mod. Phys., 74:145-195, March 2002

[19] C. H. Bennett, G. Brassard, C. Crepeau, R. Jozsa, A. Peres, and W. K.Wootters. Teleporting an unknown quantum state via dual classical and einstein podolskyrosen channels. Phys. Rev. Lett., 70:1895-1899, March 1993.

[20] M. A. Nielsen and I. L. Chuang. Quantum Computation and Quantum Information: 10th Anniversary Edition. Cambridge University Press, Cambridge, 2010.

[21] P. G. Kwiat, K. Mattle, H. Weinfurter, A. Zeilinger, A. V. Sergienko, and Y. Shih. New high-intensity source of polarization-entangled photon pairs. Phys. Rev. Lett., 75:4337-4341, December 1995.

[22] Q. Zhou, S. Dong, W. Zhang, L. You, Y. He, W. Zhang, Y. Huang, and J. Peng. Frequency-entanglement preparation based on the coherent manipulation of frequency nondegenerate energy-time entangled state. J. Opt. Soc. Am. B, 31(8):1801-1806, August 2014.

[23] Mair1, A., Vaziri, A., Weihs, G. Zeilinger, A. Entanglement of the orbital angular momentum states of photons. Nature 412, 313316 (2001).

[24] J. D. Franson. Bell inequality for position and time. Phys. Rev. Lett., 62:2205-2208,May 1989.

[25] W. Tittel, J. Brendel, H. Zbinden, and N. Gisin. Quantum cryptography using entangled photons in energy-time bell states. Phys. Rev. Lett., 84:4737-4740, May 2000.

[26] I. Marcikic, H. de Riedmatten, W. Tittel, V. Scarani, H. Zbinden, and N. Gisin. Time-bin entangled qubits for quantum communication created by femtosecond pulses. Phys. Rev. A, 66:062308, December 2002.

[27] H. Jayakumar, A. Predojevi, T. Kauten, T. Huber, G. S. Solomon, and G. Weihs. Time-bin entangled photons from a quantum dot. 5:4251, June 2014.

[28] H. Takesue and K. Inoue. Generation of 1.5um band time-bin entanglement using spontaneous

ber four-wave mixing and planar light-wave circuit interferometers. Phys. Rev. A, 72:041804, October 2005

[29] http://www.rri.res.in/quic/resources/opn2019/

[30] A. Dousse, J. Suffczyski, A. Beveratos, O. Krebs, A. Lemaitre, I.Sagnes, J. Bloch,P.Voisin, and P. Senellart. Ultra bright source of entangled photon pairs. Nature, 466(7303):217-220, July2010

[31] Hoi-Kwong Lo, Marcos Curty, and Bing Qi. Measurement-device-independent quantum key distribution. Physical review letters, 108(13):130503, 2012.

[32] Charles Ci Wen Lim, Christopher Portmann, Marco Tomamichel, Renato Renner,and Nicolas Gisin. Device-independent quantum key distribution with local bell test. Physical Review X, 3(3):031006, 2013.

[33] Bennett C H, Brassard G, Crepeau C, Jozsa R, Peres A, Wootters W K 1993 Phys. Rev. Lett. 70-1895

[34] Bouwmeester D, Pan J W, Mattle K, Eibl M, Weinfurter H, Zeilinger A 1997 Nature 390 575

[35] M Z ukowski, A Zeilinger, MA Horne, and AK Ekert. event-ready-detectors bell experiment via entanglement swapping. Physical Review Letters,71(26):4287, 1993

[36] Charles H Bennett, Gilles Brassard, Claude Crépeau, Richard Jozsa, Asher Peres,and William K Wootters. Teleporting an unknown quantum state via dual classical and einstein-podolsky-rosen channels. Physical review letters, 70(13):1895, 1993.

[37] Nicolas Sangouard, Christoph Simon, Hugues De Riedmatten, and Nicolas Gisin. Quantum repeaters based on atomic ensembles and linear optics. Reviews of Modern Physics, 83(1):33, 2011

[38] Hoi-Kwong Lo, Marcos Curty, and Bing Qi. Measurement-device-independent quantum key distribution. Physical review letters, 108(13):130503, 2012.

[39] John Calsamiglia and Norbert Lutkenhaus. Maximum efficiency of a linear-optical bell state analyzer. Applied Physics B, 72(1):67-71, 2001.

[40] Jin, X., Ren, J., Yang, B. et al. Experimental free-space quantum teleportation. Nature Photon 4, 376381 (2010).

[41] Peter van Loock .Laser Photonics Rev. 5, No. 2, 167200 (2011)

[42] S.J. van Enk, N. Lutkenhaus, H.J. Kimble.Phys. Rev. A 75, 052318 (2007)

[43] Boschi D, Branca S, de Martini F, Hardy L, Popescu S 1998 Phys. Rev. Lett. 80 1121

[44] Duan L M, Lukin M D, Cirac J I, Zoller P 2001 Nature 414 413

[45] Briegel H J, Dr W, Cirac J I, Zoller P 1998 Phys. Rev.Lett. 81 5932

[46] Einstein A, Podolsky B, Rosen N 1935 Phys. Rev. 47 777

[47] Zukowski M, Zeilinger A, Horne M A, et al. Event-ready-detectors Bell experiment via entanglement swapping. Phys Rev Lett, 1993, 71: 42874290

[48] Ji-Gang Ren, Ping Xu, Hai-Lin Yong, Liang Zhang, Sheng-Kai Liao, Juan Yin, Wei-Yue Liu, Wen-Qi Cai, Meng Yang, Li Li, Kui-Xing Yang, Xuan Han, Yong-Qiang Yao, Ji Li, Hai-Yan Wu, Song Wan, Lei Liu, Ding-Quan Liu, Yao-Wu Kuang, Zhi-Ping He, Peng Shang, Cheng Guo, Ru-Hua Zheng, Kai Tian, Zhen-Cai Zhu, NaiLeLiu, Chao-Yang Lu, Rong Shu, Yu-Ao Chen, Cheng-Zhi Peng, Jian-Yu Wang, and Jian-Wei Pan. Ground-to-satellite quantum teleportation. Nature, advance online publication, August 2017.

[49] Jiu-Peng Chen, Chi Zhang, Yang Liu, Cong Jiang, Weijun Zhang, Xiao-Long Hu, Jian-Yu Guan, Zong-Wen Yu, Hai Xu, Jin Lin, Ming-Jun Li, Hao Chen, Hao Li, Lixing You, Zhen Wang, Xiang-Bin Wang, Qiang Zhang, and Jian-Wei Pan Phys. Rev. Lett. 124, 070501 2020

[50] https://www.technologyreview.com/s/612964/what-is-quantum-communications/

[51] H.-J. Briegel, W. D, J. I. Cirac, and P.Zoller. Quantum repeaters: The role of imperfect local operations in quantum communication. Phys. Rev. Lett., 81:5932-5935, December 1998.

[52] L.-M. Duan et al., Nature (London) 414, 413 (2001).

[53] Li, Z., Zhang, R., Yin, X. et al. Experimental quantum repeater without quantum memory. Nat. Photonics 13, 644648 (2019).

[54] Azuma, Koji and Tamaki, Kiyoshi and Lo, Hoi-Kwong. All-photonic quantum repeaters. Nat Commun 6, 6787 (2015)

[55] C. Simon, H. de Riedmatten, M. Afzelius, N. Sangouard, H. Zbinden, and N. Gisin.Quantum repeaters with photon pair sources and multimode memories. Phys. Rev.Lett., 98:190503, May 2007.

[56] N. Sinclair, E. Saglamyurek, H. Mallahzadeh, J. A. Slater, M. George, R. Ricken,M. P. Hedges, D. Oblak, C. Simon, W. Sohler, and W. Tittel. Spectral multiplexing for scalable quantum photonics using an atomic frequency comb quantum memory and feed-forward control. Phys. Rev. Lett., 113:053603, July 2014.

[57] Ma X S, Herbst T, Scheidl T, Wang D Q, Kropatschek S, Naylor W, Wittmann B, Mech A, Kofler J, Anisimova E, Makarov V, Jennewein T, Ursin R, Zeilinger A 2012 Nature 489 269

[58] Yin J, Ren J G, Lu H, Cao Y, Yong H L, Wu Y P, Liu C, Liao S K, Zhou F, Jiang Y, Cai X D, Xu P, Pan G S, Jia J J, Huang Y M, Yin H, Wang J Y, Chen Y A, Peng C Z, Pan J W 2012 Nature 488 185

[59] Stevenson R M, Nilsson J, Bennett A J, Skiba- Szymanska J, Farrer I, Ritchie D A, Shields A J 2013 Nat. Commun. 4 2859

[60] Bussieres F, Clausen C, Tiranov A, Korah B, Verma V B, Nam S W, Marsili F, Ferrier A, Goldner P, Herrmann H, Silberhorn C, Sohler W, Afzelius M, Gisin N 2014 Nat. Photonics 8 775

[61] Pfaff W, Hensen B, Bernien H, Dam S B V, Blok M S, Taminiau T H, Tiggelman M J, Schouten R N, Markham M, Twitchen D J, Hanson R 2014 Science 345 532

[62] Wang X L, Cai X D, Su Z E, Chen M C, Wu D, Li L, Liu N L, Lu C Y, Pan J W 2015 Nature 518 516

[63] Pan, J., Simon, C., Brukner, . et al. Entanglement purification for quantum communication. Nature 410, 10671070 (2001)

[64] N. Sinclair, E. Saglamyurek, H. Mallahzadeh, J. A. Slater, M. George, R. Ricken,M. P. Hedges, D. Oblak, C. Simon, W. Sohler, and W. Tittel. Spectral multiplexing for scalable quantum photonics using an atomic frequency comb quantum memory and feed-forward control. Phys. Rev. Lett., 113:053603, July 2014

[65] Long-distance quantum communication with neutral atoms Mohsen Razavi and Jeffrey H. Shapiro Phys. Rev. A 73, 042303 2006

[66] Marcel.li Grimau Puigibert.Towards a Real-World Quantum Repeater

[67] Burnham D. C. and Weinberg D. L. Observation of Simultaneity in Parametric Production of Optical Photon Pairs. Physical Review Letters, 1970, 25: 84-87.

[68] Ghosh R.and Mandel L. Observation of Nonclassical Effects in the Interference of Two Photons. Phys. Rev. Lett., 1987, 59:1903.

[69] JW. Pan, ZB. Chen, C Y. Lu, H.Weinfurter, A. Zeilinger,and M. Zukowski. Multiphoton entanglement and interferometry. Rev. Mod. Phys. 84:777-838, May 2012.

[70] Towards a Real-World Quantum Repeater Marcel.li Grimau Puigibert a thesis of Doctor of Philosophy university of Calgary

[71] R. W. Boyd. Nonlinear Optics. Elsevier LTD, Oxford, 2008.

[72] D.F. Walls and G. J. Milburn. Quantum Optics. Springer, 2008 2nd edition.

[73] James Schneeloch et al 2019 J. Opt. 21 043501

[74] Couteau, C. Spontaneous parametric down-conversion. Contemp. Phys. 59, 291304 (2018).

[75] J. A. Armstrong, N. Bloembergen, J. Ducuing, and P. S. Pershan Phys. Rev. 127, 1918 1962.

[76] Bahabad A., Murnane M. M. and Kapteyn H.C. Quasi-phase-matching of momentum and energy in nonlinear optical processes. Nature Photonics, 2010, 4: 570 575.

[77] https://www.covesion.com

[78] Comptes Rendus Physique Volume 8, Issue 2, March 2007, Pages 180-198

[79] Shih Y. H. and Alley C. O. New Type of Einstein-Podolsky-Rosen-Bohm Experiment Using Pairs of Light Quanta Produced by Optical Parametric Down Conversion. Phys. Rev. Lett., 1988, 61: 2921.

[80] KiessT. E., Shih Y. H., Sergienko A. V. and Alley C. O. Einstein-Podolsky-Rosen- Bohm experiment using pairs of light quanta produced by type-II parametric downconversion. Phys. Rev. Lett., 1993, 71: 3893.

[81] Olivier Alibart, Virginia D Auria, Marc de Micheli, Florent Doutre, Florian Kaiser, et al.. Quantum photonics at telecom wavelengths based on lithium niobate waveguides. Journal of Optics, Institute of Physics (IOP), 2016, 18 (10), pp.104001.

[82] https://www.thorlabs.com/catalogpages/693.pdf

[83] Lutfi Arif BIN NGAH, All-optical synchronization for quantum networking.Phd thesis

[84] Triply-Resonant Cavity-Enhanced Spontaneous Parametric Down-Conversion Dipl thesis .-Phys. Andreas Ahlrichs

[85] High performance photon-pair source based on a fiber-coupled periodically poled KTP. Master Thesis. Tian Zhong .

[86] E. C. Cheung, Karl Koch, Gerald T. Moore, and J. M. Liu, "Measurements of second-order nonlinear optical coefficients from the spectral brightness of parametric fluorescence," Opt. Lett. 19, 168-170 (1994).

[87] R.W. Boyd. Nonlinear Optics. Academic Press, second edition (2003).ISBN: 0-12-121682-9.

[88] Paschotta Encyclopedia of lasers physics and technology.[J] 2008

[89] Triply-Resonant Cavity-Enhanced Spontaneous Parametric Down-Conversion Dipl thesis .-Phys. Andreas Ahlrichs

[90] E Pomarico et al 2012 New J. Phys. 14 033008

[91] Narrowband Single Photons for Light-Matter Interfaces. Msc thesis Markus Rambach

[92] OBrien J L, Furusawa A and Vuckovic J 2009 Quantum communication Nature Photonics 3 687

[93] Smith B J, Kundys D, Thomas-Peter N, Smith P G R and Walmsley I A 2009 Phase-controlled integrated photonic quantum circuits Opt. Express 17 13516

[94] Sansoni L, Sciarrino F, Vallone G, Mataloni P, Crespi A, Ramponi R and Osellame R 2010 Polarization entangled state measurement on a chip Phys. Rev. Lett. 105 200503

[95] Lu Y J and Ou Z Y 2000 Optical parametric oscillator far below threshold: experiment versus theory Phys. Rev. A 62 033804

[96] Wang H, Horikiri T and Kobayashi T 2004 Polarization-entangled mode-locked photons from cavity enhanced spontaneous parametric down-conversion Phys. Rev. A 70 043804

[97] Neer gaard-Nielsen J S, Nielsen B M, Takahashi H, Vistnes A I and Polzik E S 2007 High purity bright single photon source Opt. Express 15 7940

[98] Scholz M, Koch L, Ullmann R and Benson O 2009 Single-mode operation of a high-brightness narrow-band single-photon source Appl. Phys. Lett. 94 201105

[99] Jeronimo-Moreno Y, Rodriguez-Benavides S and URen A B 2010 Theory of cavity-enhanced spontaneous parametric down conversion Laser Phys. 20 1221

[100] Jundt D H 1997 Temperature-dependent Sellmeier equation for the index of refraction, n_e in congruent lithium niobate Opt. Lett. 22 1553

[101] Markus Rambach Narrowband Single Photons for Light-Matter Interfaces. Thesis 2017.

[102] Ou ZY, Lu YJ (1999) Cavity enhanced spontaneous parametric down-conversion for the prolongation of correlation time between conjugate photons. Physical Review Letters 83(13) : 2556 – 2559. https://doi.org/10.1103/PhysRevLett.83.2556

[103] Florian Wolfgramm, Yannick A. de Icaza Astiz, Federica A. Beduini, Alessandro Cere‘, and Morgan W. Mitchell. Atom-Resonant Heralded Single Photons by Interaction-Free Measurement. Phys. Rev. Lett. 106, 053602 2011

[104] Julia Fekete, Daniel Rielander, Matteo Cristiani, Hugues de Riedmatten Ultranarrow-Band Photon Pair Source Compatible with Solid State Quantum Memories and Telecommunication Networks. Phys. Rev. Lett. 110, 220502 2013

[105] Kai-Hong Luo, Harald Herrmann, Stephan Krapick,et.al.Two-color narrowband photon pair source with high brightness based on clustering in a monolithic waveguide resonator. arXiv:1306.1756

[106] Haibo Wang, Tomoyuki Horikiri, and Takayoshi Kobayashi Polarization-entangled mode-locked photons from cavity-enhanced spontaneous parametric down-conversion. Phys. Rev. A 70, 043804 Published 5 October 2004

[107] Fujii G, Namekata N, Motoya1M, Kurimura S and Inoue S 2007 Bright narrowband source of photon pairs at optical telecommunication wavelengths using a type-II periodically poled lithium niobate waveguide Opt. Express 15 12769

[108] J. W. Goodman. Introduction to Fourier Optics (2nd ed.). pp. 6162

[109] Huang Y P, Altepeter J B and Kumar P 2010 Heralding single photons without spectral factor ability Phys. Rev. A 82 043826

[110] Tian Zhong, Franco N. C. Wong, Tony D. Roberts, and Philip Battle, "High performance photon-pair source based on a fiber-coupled periodically poled KTiOPO4 waveguide," Opt. Express 17, 12019-12030 (2009)

[111] Giordmaine J A and Miller R C 1966 Optical parametric oscillation in LiNbO3 Physics of Quantum Electronics ed P L Kelley, B Lax and PE Tannenwald (New York: McGraw-Hill)

[112] Eckardt R C, Nabors C D, Kozlovsky W J and Byer R L 1991 Optical parametric oscillator frequency tuning and control J. Opt. Soc. Am. B 8 646

[113] P. Sekatski, N. Sangouard, F. Bussieres, C. Clausen, N. Gisin, and H. Zbinden, e-print arXiv:1109.0194 (2011).

[114] M. N. OSullivan, K. W. C. Chan, V. Lakshminarayanan, and R. W. Boyd, Phys. Rev. A 77, 023804 (2008).

[115] P. P. Rohde, J. G.Webb, E. H. Huntington, and T. C. Ralph, New J. Phys. 9, 233 (2007).

[116] Y. P. Huang, J. B. Altepeter, and P. Kumar, Phys. Rev. A 84, 033844 (2011).

[117] M. A. Broome, M. P. Almeida, A. Fedrizzi, and A. G. White, Optics Express 19, 22698 (2011).

[118] Masahiro Takeoka et al 2015 New J. Phys. 17 043030

[119] A. I. Lvovsky. Squeezed light (2016)

[120] Krovi, H., Guha, S., Dutton, Z. et al. Practical quantum repeaters with parametric down-conversion sources. Appl. Phys. B 122, 52 (2016).

[121] Scarani, V., de Riedmatten, H., Marcikic, I. et al. Four-photon correction in two-photon Bell experiments. Eur. Phys. J. D 32, 129138 (2005).

[122] Pieter Kok, Samuel L.Braunstein. Postselected versus nonpostselected quantum teleportation using parametric down-conversion. Phys.Rev.A61:42304,2000

[123] Andreas Christ* and Christine Silberhorn, Limits on the deterministic creation of pure single-photon states using parametric down-conversion. PHYSICAL REVIEW A 85, 023829 (2012)

[124] Christopher J. Chunnilall,Ivo Pietro Degiovanni Stefan Kck, Ingmar Mller, Alastair G. Sinclair. Metrology of single-photon sources and detectors: a review.

[125] R. H. Hadfield, Single-photon detectors for optical quantum information applications, Nat. Photon. 3(11), 609705 (2009).

[126] H. Paul et al., Photon chopping: new way to measure the quantum state of light, Phys. Rev. Lett. 76(14), 24642467 (1996).

[127] K. Banaszek and I. A. Walmsley, Photon counting with loop detector, Opt. Lett. 28(1), 5254 (2003).

[128] M. J. Fitch et al., Photon-number resolution using time-multiplexed single-photon detectors, Phys. Rev. A 68(4), 043814 (2003).

[129] Steve M. Young, Mohan Sarovar, and Franois Lonard .Design of High-Performance Photon-Number-Resolving Photodetectors Based on Coherently Interacting Nanoscale Elements. ACS Photonics (2020)

[130] D. Achilles et al., Fiber-assisted detection with photon number resolution,Opt. Lett. 28(23), 23872389 (2003).

[131] D. Achilles et al., Fiber-assisted detection with photon number resolution, Opt. Lett. 28(23), 23872389 (2003).

[132] C. Silberhorn, Detecting quantum light, Contemp. Phys. 48(3), 147156 (2007).

[133] Rosenberg, D.; Lita, A. E.; Miller, A. J.; Nam, S. W. Noise-free high-efficiency photon-number-resolving detectors. Phys. Rev. A: At., Mol., Opt. Phys. 2005

[134] Fukuda, D.; Fujii, G.; Numata, T.; Amemiya, K.; Yoshizawa, A.; Tsuchida, H.; Fujino, H.; Ishii, H.; Itatani, T.; Inoue, S.; Zama, T.Titanium-based transition-edge photon number resolving detector with 98 % detection efficiency with index-matched small-gap fiber coupling. Opt. Express 2011.

[135] Kardynal, B.; Yuan, Z.; Shields, A. An avalanche photodiode based photon number resolving detector. Nat. Photonics 2008.

[136] Waks, E.; Inoue, K.; Oliver, W. D.; Diamanti, E.; Yamamoto, Y. High-efficiency photon-number detection for quantum information processing. IEEE J. Sel. Top. Quantum Electron. 2003.

[137] Design of High-Performance Photon-Number-Resolving Photodetectors Based on Coherently Interacting Nanoscale Elements Steve M. Young, Mohan Sarovar, and Franois Lonard ACS Photonics 2020.

[138] S. Kako, C. Santori, K. Hoshino, S. Gotzinger, Y. Yamamato, and Y. Arakawa, Nature Mater. 5, 887 (2006).

[139] A. J. Shields, Nature Photon. 1, 215 (2007).

[140] D. Leonard, M. Krishnamurthy, C. M. Reaves, S. P. Denbaars, and P. M. Petroff, Appl. Phys. Lett. 63, 3203 (1993).

[141] M D Eisaman 1, J Fan, A Migdall, S V Polyako, Single-photon sources and detectors, Review of Scientific Instruments 82, 071101 (2011)

[142] X. Brokmann, E. Giacobino, M. Dahan, and J. Hermier, Appl. Phys. Lett.85, 712 (2004).

[143] C. M. Santori, Ph.D. dissertation, Stanford University, 2003.

[144] V. Kuhlmann, J. H. Prechtel, J. Houel, A. Ludwig, D. Reuter, A. D. Wieck, and R. J. Warburton, Transform-limited single photons from a single quantum dot, Nat. Commun. 6, 8204 (2015).

[145] G. Kiranske, H. Thyrrestrup, R. S. Daveau, C. L. Dreeen, T. Pregnolato, L. Midolo, P. Tighineanu, A. Javadi, S. Stobbe, R. Schott, A. Ludwig, A. D. Wieck, S. I. Park, J. D. Song, A. V. Kuhlmann, I. Sllner, M. C. Lbl, R. J. Warburton, and P. Lodahl, Indistinguishable and efficient single photons from a quantum dot in a planar nanobeam waveguide, Phys. Rev. B 96, 165306 (2017).

[146] J. C. Loredo, N. A. Zakaria, N. Somaschi, C. Anton, L. de Santis, V. Giesz, T. Grange, M. A. Broome, O. Gazzano, G. Coppola, I. Sagnes, A. Lemaitre, A. Auffeves, P. Senellart, M. P. Almeida, and A. G. White, Scalable performance in solid-state single-photon sources, Optica 3, 433440 (2016).

[147] N. Somaschi, V. Giesz, L. De Santis, J. C. Loredo, M. P. Almeida, G. Hornecker, S. L. Portalupi, T. Grange, C. Antn, J. Demory, C. Gmez, I. Sagnes, N. D. Lanzillotti-Kimura, A. Lematre, A. Auffeves, A. G. White, L. Lanco, and P. Senellart, Near-optimal single-photon sources in the solid state, Nat. Photonics 10, 340 (2016).

[148] A. V. Kuhlmann, J. Houel, A. Ludwig, L. Greuter, D. Reuter, A. D. Wieck, M. Poggio, and R. J. Warburton, Charge noise and spin noise in a semiconductor quantum device, Nat. Phys.

9, 570 (2013).

[149] C. Santori et al., Triggered single photons from a quantum dot, Phys. Rev. Lett. 86(8), 15021505 (2001).

[150] Z. L. Yuan et al., Electrically driven single-photon source, Science 295(5552), 102105 (2002).

[151] V. Zwiller, T. Aichele, W. Seifert, J. Persson, and O. Benson, Appl. Phys.Lett. 82, 1509 (2003).

[152] M. B. Ward, T. Farrow, P. See, Z. L. Yuan, O. Z. Karimov, A. J. Bennett,A. J. Shields, P. Atkinson, K. Cooper, and D. A. Ritchie, Appl. Phys. Lett. 90, 063512 (2007).

[153] E. B. Flagg, A. Muller, S. V. Polyakov, A. Ling, A. Migdall, and G. S. Solomon, Phys. Rev. Lett. 104, 137401 (2010).

[154] R. B. Patel, A. J. Bennett, I. Farrer, C. A. Nicoll, D. A. Ritchie, and A. J. Shields, Nature Photon. 4, 632 (2010).

[155] C. Kurtsiefer, S. Mayer, P. Zarda, and H. Weinfurter, Stable solid-state source of single photons, Phys. Rev. Lett. 85, 290293 (2000).

[156] T. M. Babinec, B. J. M. Hausmann, M. Khan, Y. Zhang, J. R. Maze, P. R. Hemmer, and M. Loncar, A diamond nanowire single-photon source, Nat. Nanotechnol. 5, 195 (2010)

[157] B. Kambs and C. Becher, Limitations on the indistinguishability of photons from remote solid state sources, New J. Phys. 20, 115003 (2018)

[158] I. Aharonovich et al., Diamond-based single-photon emitters, Rep. Prog. Phys. 74(7), 076501 (2011).

[159] C. Kurtsiefer, S. Mayer, P. Zarda, and H. Weinfurter, Phys. Rev. Lett. 85,290 (2000).

[160] R. Brouri, A. Beveratos, J.-P. Poizat, and P. Grangier, Opt. Lett. 25, 1294 (2000).

[161] M. D. Eisaman, J. Fan, A. Migdall, and S. V. Polyakov. Single-photon sources and detectors.Review of Scientific Instruments 82, 071101 (2011)

[162] R. Alleaume, F. Treussart, G. Messin, Y. Dumeige, J.-F. Roch, A. Beveratos, R. Brouri-Tualle, J.-P. Poizat, and P. Grangier, New J. Phys. 6, 92 (2004)

[163] T. Gaebel, I. Popa, A. Gruber, M. Domhan, F. Jelezko, and J. Wrachtrup, New J. Phys. 6, 98 (2004).

[164] E. Wu, J. R. Rabeau, G. Roger, F. Treussart, H. Zeng, P. Grangier, S. Prawer and J.-F. Roch, New J. Phys. 9, 434 (2007).

[165] Hanno S. Kaupp. Coupling Nitrogen-Vacancy Centers in Diamond to Fiber-based Fabry-Prot Microcavities.(2017)

[166] A. Kuhn, M. Hennrich, and G. Rempe, Deterministic single-photon source for distributed quantum networking, Phys. Rev. Lett. 89, 067901 (2002).

[167] X.-L. Chu, S. Gtzinger, and V. Sandoghdar, A single molecule as a highfidelity photon gun for producing intensity-squeezed light, Nat. Photonics 11, (2016).

[168] Mikael Afzelius, Christoph Simon, Hugues de Riedmatten, and Nicolas Gisin. Multimode quantum memory based on atomic frequency combs. Phys. Rev. A 79, 052329 Published 21 May (2009).

[169] R. B. Jin, R. Shimizu, K. Wakui, H. Benichi, and M. Sasaki, Opt. Exp. 2110659 (2013)

[170] Phillip Kaye Raymond Laflamme Michele Mosca. An Introduction to Quantum Computing. (2007).

[171] Cirac, Juan Ignacio. ”Quantum computing and simulation” Nanophotonics, vol. 10, no. 1, (2021)

[172] Arute, F., Arya, K., Babbush, R. et al. Quantum supremacy using a programmable superconducting processor. Nature 574, 505510 (2019).

[173] I. Georgescu. Nobel prize 2012: Haroche wineland. Nature Physics, 8(777), (2012).

[174] Hall Glauber and Hnsch. Trabesinger, a. nobel prize 2005. Nature Physics,1(930), (2005).

[175] The Royal Swedish Academy of Sciences. Nobelprize.org. NobelPrize.org, Oct (1991).

[176] The Royal Swedish Academy of Sciences. Nobelprize.org. NobelPrize.org, Oct (1997).

[177] The Royal Swedish Academy of Sciences. Nobelprize.org. NobelPrize.org, Oct (2001).

[178] Christian L Degen, F Reinhard, and P Cappellaro. Quantum sensing. Reviews of modern physics, 89(3):035002, (2017).

[179] T. Gefen, A. Rotem, and Retzker. Overcoming resolution limits with quantum sensing. Nature Communication, 10:4992, (2019).

[180] M.E Trusheim. Nanoscale Engineering of Spin-Based Quantum Devices in Diamond. PhD thesis, MASSACHUSETTS INSTITUTE OF TECHNOLOGY, (2018).

[181] D. Drung, C. Abmann, J. Beyer, A. Kirste, M. Peters, F. Ruede, and T. Schurig. Highly sensitive and easy-to-use squid sensors. IEEE Transactions on Applied Superconductivity,17(2):699704, (2007).

[182] I. K. Kominis, T. W. Kornack, J. C. Allred, and M. V. Romalis. A subfemtotesla multichannel atomic magnetometer. Nature Photonics, 422:596599, (2003).

[183] R. Lutwak, J. Deng, W. Riley, M. Varghese, J. Leblanc, G. Tepolt, M. Mescher, D. K. Serkland, K. M. Geib, and G. M. Peake. The chip-scale atomic clock -low-power physics package. In Proceedings of the 36th Annual Precise Time and Time Interval Systems and Applications Meeting, pages 339354, (2012).

[184] V. Shah, S. Knappe, P.D.D Schwindt, and J. Kitching. Subpicotesla atomic magnetometry with a microfabricated vapour cell. Nature Photonics, 1:649652, (2007).

[185] Michael A. Lombardi, Thomas P. Heavner, and Steven R. Jefferts. Nist primary frequency standards and the realization of the si second. NCSLI Measure, 2(4):7489, (2007).

[186] Jun Ye, H. Schnatz, and L. W. Hollberg. Optical frequency combs: from frequency metrology to optical phase control. IEEE Journal of Selected Topics in Quantum Electronics, 9(4):10411058, (2003).

[187] Antonio Acn et al 2018 New J. Phys. 20 080201

[188] Sun, D., Zhang, Y., Wang, D. et al. Microstructure and domain engineering of lithium niobate crystal films for integrated photonic applications. Light Sci Appl 9, 197 (2020).

[189] P. Kmr, E. M.Kessler,M. Bishof, L. Jiang,A. S. Srensen,J. Ye, and M. D. Lukin, Nat. Phys. 10, 582 (2014).

[190] L. Badurina1, E. Bentine, D. Blas, K. Bongs, D. Bortoletto2, T. Bowcock, K. Bridges4, W. Bowden,, O. Buchmueller6, C. Burrage. AION: an atom interferometer observatory and network Journal of Cosmology and Astroparticle Physics, Volume (2020).

[191] Daniel Gottesman, Thomas Jennewein, Sarah Croke Longer-Baseline Telescopes Using Quantum Repeaters. Phys. Rev. Lett. 109, 070503 (2012)

[192] Kmr, P., Kessler, E., Bishof, M. et al. A quantum network of clocks. Nature Phys 10, 582587 (2014).

[193] Kimble, H. The quantum internet. Nature 453, 10231030 (2008).

[194] Caleffi, Marcello; Cacciapuoti, Angela Sara; Bianchi, Giuseppe. Quantum internet: from communication to distributed computing!. NANOCOM '18 Proceedings of the 5th ACM International Conference on Nanoscale Computing and Communication. (2018).

[195] https://en.wikipedia.org

[196] Severin Daiss, Stefan Langenfeld, Stephan Welte1 , Emanuele Distante, Philip Thomas, Lukas Hartung, Olivier Morin1 , Gerhard Rempe. A quantum-logic gate between distant quantum-network modules. Science 05 Feb (2021).

Appendix A

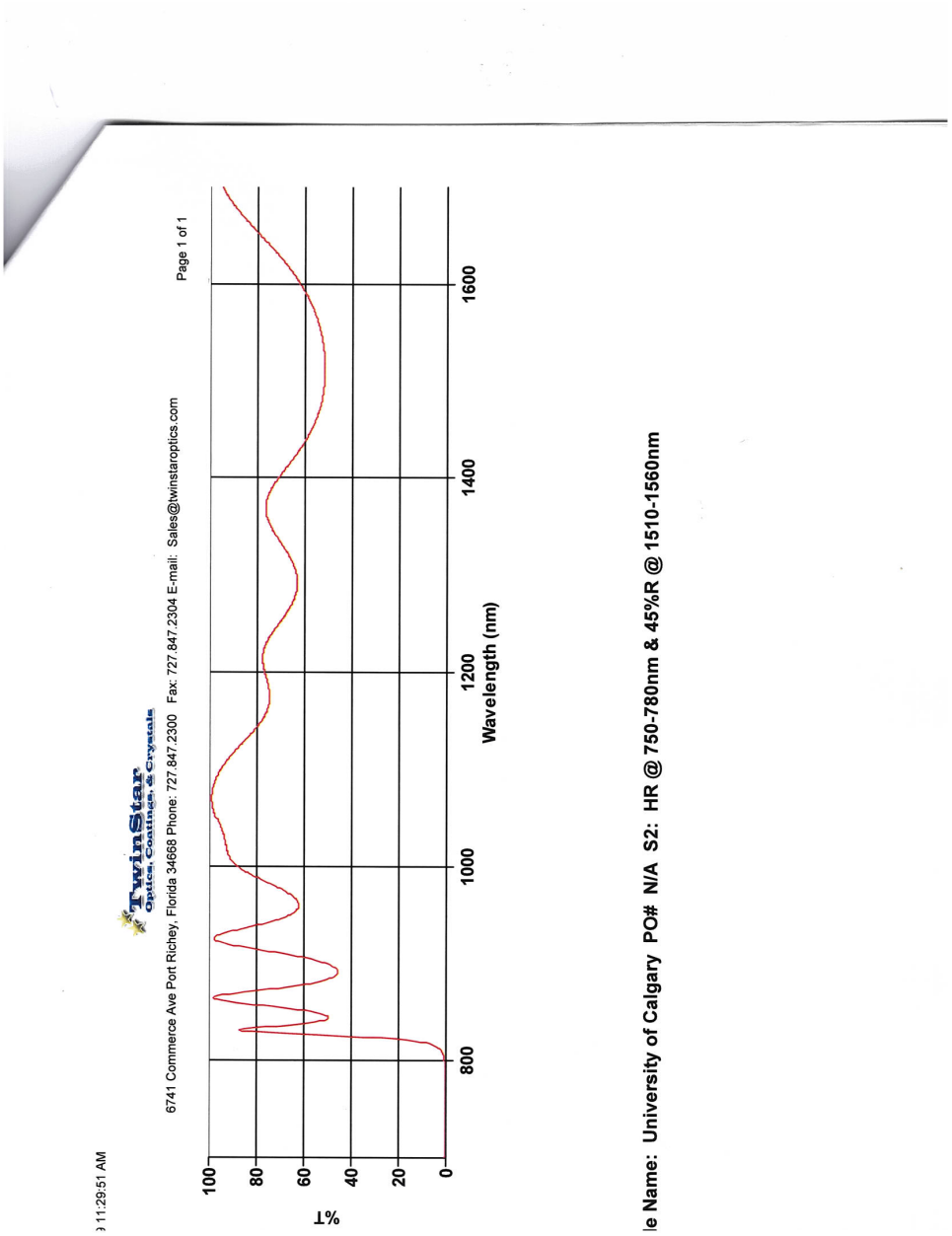

Figure A.1: **Cavity coating A**

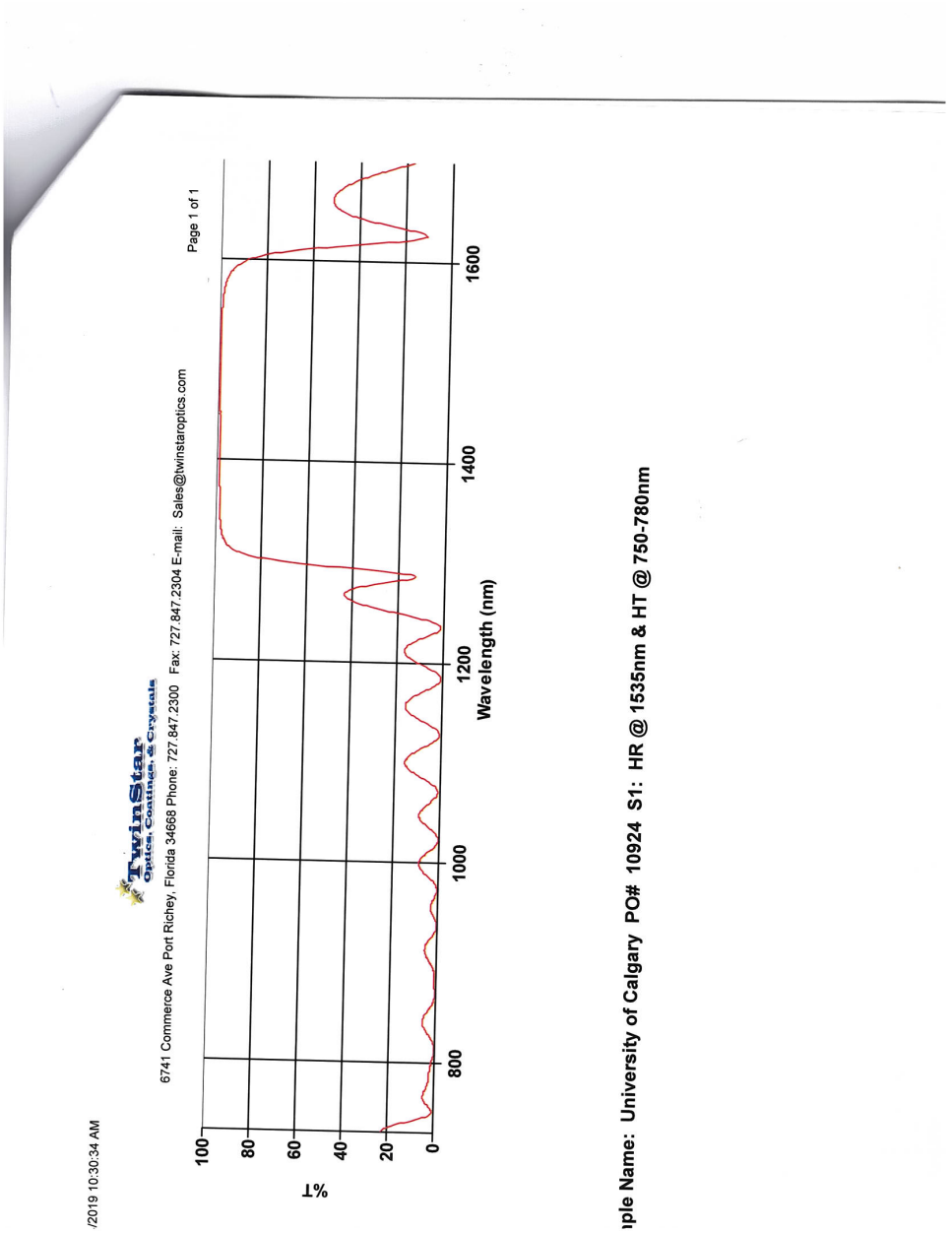

Figure A.2: **Cavity coating B**